UNIVERSITY OF MANITOBA

ELECTROWEAK RADIATIVE CORRECTIONS AND PARITY-VIOLATING ELECTRON-NUCLEON SCATTERING

By

Svetlana Barkanova

A THESIS

Submitted to the Faculty of Graduate Studies
of the University of Manitoba
in partial fulfillment of the requirements for
the degree of Doctor of Philosophy

Winnipeg, Manitoba
August 28, 2004

THE UNIVERSITY OF MANITOBA

FACULTY OF GRADUATE STUDIES

*****

COPYRIGHT PERMISSION

ELECTROWEAK RADIATIVE CORRECTIONS AND PARITY-VIOLATING ELECTRON-NUCLEON SCATTERING

BY

Svetlana Barkanova

A Thesis/Practicum submitted to the Faculty of Graduate Studies of The University of Manitoba in partial fulfillment of the requirement of the degree

Doctor Of Philosophy

DEDICATED

to my father

GENNADIJ BARKANOVS

1941 - 1999

Svetlana Barkanova

ELECTROWEAK RADIATIVE CORRECTIONS AND PARITY-VIOLATING ELECTRON-NUCLEON SCATTERING

August 28, 2004

Radiative corrections to the parity-violating asymmetry measured in elastic electron-proton scattering are analyzed in the framework of the Standard Model. The new method of constrained differential renormalization is used. We include the complete set of one-loop contributions to one quark current amplitudes. The contribution of soft photon emission to the asymmetry is also calculated, giving final results free of infrared divergences. The proper combination of single-quark parameters corresponding to specific corrections for the proton and neutron is included. A partially computerized procedure developed and tested specifically for electron-proton scattering can be relatively easy modified for any electroweak processes. It can be expanded to accommodate the Minimal Super Symmetric Model as well. Computerizing some stages of the calculations allowed retaining the momentum dependence, neglected in previous works. In addition to an extensive analysis of the kinematical dependence of electroweak radia-

tive corrections, the dependence on some poorly constrained parameters of the Standard Model was carefully analyzed.

Precise numerical evaluations were performed for a variety of lepton-nucleon scattering experiments at different momentum transfers: SAMPLE I, II and SAMPLE III (MIT-Bates) experiments, as well as HAPPEX I and II (Jefferson Lab), G0 (JLab), A4 (MAMI) and Q_{weak} (JLab). Special attention is paid to the SAMPLE experiment, where one quark radiative corrections, when combined with previous work on many quark effects and recent experimental data, are used to place some new constraints on electroweak form factors of the nucleon. The other major result of this work is the analytical momentum-dependent expressions derived for the leading diagrams, which were singled out numerically. Substituting the relevant kinematics parameters into these user-friendly expressions gives the applicable radiative corrections to a very good approximation.

Contents

List of Figures

List of Tables

ACKNOWLEDGEMENTS

The completion of this work would not have been possible without the support and assistance of a number of people.

My gratitude goes first and foremost to my advisor, Peter Blunden, for his continued guidance, instruction, support, and encouragement.

I also would like to thank the members of my thesis committee, Juris Svenne and Craig Platt, and the external referee Malcolm Butler, for their feedback and patience. My special gratitude goes to Shelley Page, from whose comments and corrections I have learned so much.

I am deeply indebted to Aleksands Aleksejevs, my dear colleague, whose constant support and proficient advice have been invaluable, especially his tireless assistance with programming and many inspiring discussions.

And last, I would like to acknowledge the significant support from the University of Manitoba Graduate Fellowship, University of Manitoba Student Union Scholarship for Excellence in Academic Achievement, Ernst and Ingrid Bock Graduate Award, as well as travel grants from University of Manitoba Faculty of Graduate Studies, TRIUMF, and the National Institute for Nuclear Theory.

1 Overview

1.1 Introduction

Although the basic validity of Quantum Chromodynamics (QCD) has rarely been doubted in recent years, confinement of quarks is still a mystery. QCD is very well understood at short distance scales, where perturbational methods apply. At the longest distance scales, where hadrons form, the picture is at best incomplete. There are still many interesting things to be learned from low energy, elastic electron-nucleon scattering.

The surprising discovery by the European Muon Collaboration showed that only 30% of the spin of the proton is carried by the spin of the quarks [5]. If one assumes that polarized s-quarks are not important, the result should be closer to 60-65%. Quark orbital angular momentum and gluon spin make up the remainder of the nucleon spin.

Overall, recent discoveries suggest that sizeable strange quark contributions to nucleon matrix elements may exist, parameterized by strangeness electric and magnetic form factors [19]. An attempt to understand the strange quark contribution to nucleon electroweak form factors is one of the areas of active theoretical and experimental interest. With uud valence quarks in the proton and udd in the neutron, the strange quark s is exclusively part of quark-antiquark sea. The c, b and t quarks also

contribute to the sea, but their effects can be handled in the heavy quark approximation by the methods of perturbative QCD. Assuming that u and d quarks in the sea behave in the same manner as s-quarks, we hope to use s-quarks as the key to understanding the overall sea properties. At present, theoretical estimates of strangeness electric and magnetic form factors span a wide spectrum in both magnitude and sign (see Table 1).

The electromagnetic current is a pure $SU(3)_f$ flavour octet. By exploiting flavor symmetries one can separate two flavor structures: the isovector, $(u-d)$, and the hypercharge, $(u+d-2s)$. There is no singlet component $(u+d+s)$, so the electromagnetic current can not provide sufficient information to separate u, d, and s contributions.

The Z^0 offers a new flavor coupling to the nucleon proportional to weak isospin, which samples $(u-d-s)$ in the light quark sector. Knowing matrix elements of $(u-d)$, the Z^0 can be used as a probe to find strange quark matrix elements in the nucleon [36]. One can measure such direct characteristics of strangeness in the nucleon as the strange magnetic moment $\mu_s = \frac{1}{2} s^\dagger \overrightarrow{r} \times \overrightarrow{\alpha} s$, the strangeness charge radius $r_s^2 = s^\dagger r^2 s$, and the strangeness analog of the axial charge $\overline{s}\overrightarrow{\gamma}\gamma_5 s$, which can serve as an independent confirmation of the quark spin fraction measurements.

The Standard Model introduces an asymmetry between left and right-handed particles and predicts parity violating interference between the weak and electromagnetic

amplitudes in electron-nucleon scattering [56]. Thus, electroweak properties of the nucleon can be studied by parity-violating electron scattering at low to medium energies [9]. In this regime the asymmetry associated with the difference between cross sections for scattering of left- and right-handed electrons can be measured. Here, left- (right-) handedness means that the electron helicity $\langle \sigma \cdot \hat{p} \rangle$ is $+1$ (-1). These interference effects are small, but have been clearly detected in recent experiments [7, 10, 41]; however, extracting information of interest from the experimental data requires evaluating radiative corrections to electroweak scattering at the few percent level.

Electroweak radiative corrections to intermediate energy, parity non-conserving semi-leptonic neutral current interactions have been addressed previously [42, 43, 44, 45, 57]. In these works, radiative corrections are constructed from the underlying fundamental weak interaction between electron and quarks. Broadly, such corrections are denoted as being either one-quark or many-quark effects. The one-quark corrections involve the interaction of the electron with a single quark in the nucleon. The many-quark contributions involve two or more quarks, and include effects due to an intrinsic weak interaction in the nucleon (e.g. the anapole moment). In this work, we restrict our considerations to the one-quark contributions, because, as far as we know, one-loop processes involving the elementary particles of the Standard Model ("one-quark" type) give the dominant contribution to radiative corrections.

At the time this work was started, combined analysis of the data from the first two SAMPLE measurements compared with the existing calculations of radiative effects showed discrepancy that could not be accounted for [8]. There was an approximately 1.5s discrepancy between the extracted value of isovector axial form factor and that expected, assuming a value for the weak radiative corrections as computed by Zhu et al. [57]. This was taken to be an indication that the radiative effects in the nucleon are somewhat larger than expected based on [57] as well as earlier calculations [42, 43, 44, 45].

The primary aim of this thesis is to improve considerably the precision for corrections involving only Standard Model constituents. These calculations should be performed for a variety of lepton-nucleon scattering experiments, in order to obtain the form factor values at different momentum transfers.

The use of computer packages *FeynArts*, *FormCalc*, and *LoopTools* [21] is of great assistance in facilitating our calculations, allowing us to include the full set of one-loop contributions (there are several hundred Feynman diagrams, which are laborious and error-prone to calculate by hand), and to retain the momentum-dependence of the amplitudes, for example. This partially computerized procedure allows for performing an extensive analysis of the kinematical dependence of the radiative corrections and the dependence on some poorly constrained parameters of the Standard Model. This kind of analysis has not been done before. Our treatment of hadronic

model dependencies (e.g. kinematics) is slightly different than previous work. In addition, we have treated infrared (IR) divergences in the one-loop amplitudes by including bremsstrahlung contributions for soft photon emission. While such a prescription is not completely satisfactory, and would be better handled by also accounting for hard photons and the particular detector setup of a given experiment, it nevertheless sets the scale for uncertainties of this origin. A better way to treat the bremsstrahlung contributions is briefly described in the "Discussion and Analysis" section and is left as a future project.

The thesis is constructed as follows. Chapter 1, called "Overview", gives the overview of the general situation in the given field of research, statement and explanation of the problem, physical motivation, and some history. Part 2 of Chapter 1 explains the concept of electroweak form factors of the nucleon, shows the way form factors are constructed from the up, down and strange quark currents, and summarizes up-to-date experimental data. Part 1.2 also contains a compilation of various theoretical estimates of strangeness electric and magnetic form factors, which, at present, span a wide spectrum in both magnitude and sign. Electroweak properties of the nucleon can be studied by parity-violating electron-proton scattering at low to medium energies, where one can measure the asymmetry coming from the difference between cross sections of left- and right-handed electrons. In Part 1.3, we explain how electroweak form factors can be extracted from the asymmetry factor and how

the electroweak radiative corrections enter the picture. This formalism for parity-violating electron scattering includes definitions of the relevant currents, couplings, form factors, and kinematics. Part 1.4 presents the way the asymmetry can be measured, giving a short description for eight recently performed (SAMPLE I, II and III, HAPPEX I and II), currently underway (G0, A4) or future experiments (Q_{weak}). The information that we need to calculate radiative corrections for all eight of these experiments is also presented there. In addition to the brief description of experimental set ups, we summarize goals, kinematics, and results of the measurements (if any are available for a given experiment at this time).

Chapter 2, "Radiative Effects", sets the ground for our theoretical evaluations by summarizing the relevant aspects of the Standard Model of particle physics and deriving several key equations. Part 2 of Chapter 2 defines one-quark radiative corrections, and, in general terms, shows the way we approach their evaluation. This section outlines the one-loop calculations, including the prescription for including soft photon emission.

Chapter 3 gives the details. First, we derive the tree level parity non-conserving amplitude for the electroweak interaction in the scattering processes e+p $\rightarrow$ e+p and e+n $\rightarrow$ e+n by modeling the nucleon as a collection of quasi-free quarks carrying some fraction x of the nucleon four-momentum. Then we do the same for the one-loop amplitudes. The new method of constrained differential renormalization is used.

Renormalization constants and counterterms are evaluated. We treat infrared divergences in the one-loop amplitudes by including bremsstrahlung contributions for soft photon emission.

Chapter 4, "Results", reports the net result of a total of the 446 one-loop graphs evaluated numerically for each experiment. The analysis of their dependence on some poorly constrained parameters of the Standard Model is presented.

Numerical results for the radiative corrections applicable to different experiments are given in Section 4.1. In particular, our results are combined with other calculations of many-quark effects to discuss the implications for the SAMPLE experiment. In Part 4.2, we single out the diagrams giving the dominant contribution and derive the analytical momentum-dependent expressions for them. Now, by substituting their own kinematical parameters into these expressions, the experimentalists can obtain the applicable radiative corrections in a very good approximation. All of 446 graphs can be calculated only numerically, of course. The one-quark radiative corrections, when combined with previous work on many-quark effects and some of the available experimental results, place new constrains on electroweak form factors of the nucleon. These results, and some future prospects, are outlined in "Discussion and Analysis", Chapter 5.

Notations and conventions are chosen according to [48], unless specified otherwise.

1.2 Form Factors

1.2.1 Electromagnetic Form Factors

Nucleon electromagnetic form factors are fundamental quantities related to the charge and magnetization distributions inside the nucleon.

To illustrate the concept of the form factor most generally, let us consider the simplest case of electron scattering on a spin 0 nucleus. The internal structure of this nucleus in not known and has to be somehow parametrized. In the plane-wave Born approximation, the elastic electron-nucleus scattering cross section can be expressed as a product of two terms, one describing the cross section for elastic electron scattering from a point charge nucleus, and another one accounting for the extended charge distribution:

$$\frac{d\sigma}{d\Omega} = \left(\frac{d\sigma}{d\Omega}\right)_{point} |F(\mathbf{q})|^2 . \tag{1}$$

For a point-like charge distribution, $F(\mathbf{q})$ would be equal to 1.

Assuming a static nucleus and relativistic electrons, for the first term of Eq. (1) we can use well-known Mott formula:

$$\left(\frac{d\sigma}{d\Omega}\right)_{point} = \frac{(Z\alpha)^2 \cos^2\frac{\theta}{2}}{(2E\sin^2\frac{\theta}{2})^2}, \tag{2}$$

where $\alpha = e^2/4\pi$, E is the energy of the incident electron, and θ is its scattering

angle. The momentum transfer is defined as

$$q^2 = -4EE' \sin^2 \frac{\theta}{2}, \tag{3}$$

where E' is the energy of the scattered electron. See the diagram below for illustration.

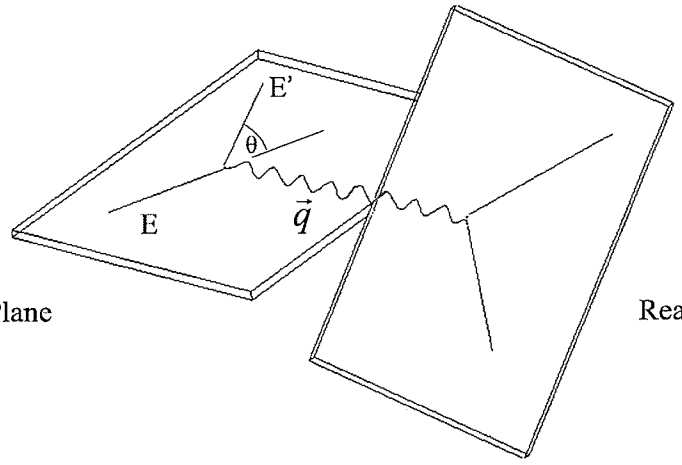

The form factor $F(\mathbf{q})$ is a well defined mathematical concept since it is the Fourier transform of the ground state nuclear charge distribution:

$$F(\vec{q}) = \int \rho(\vec{x}) e^{i\vec{q}\cdot\vec{x}} d^3x, \tag{4}$$

$$\rho(\vec{x}) = \int F(\vec{q}) e^{i\vec{q}\cdot\vec{x}} d^3q. \tag{5}$$

For a spin 1/2 particle there are additional contributions from the magnetization distribution. As the magnetic moments of the proton and neutron differ in reality

from the particle Dirac magnetic moment $\mu = e\hbar/2Mc$, we have to include a factor to correct for μ. Thus, the Rosenbluth formula describes the differential cross section for the electron-nucleon scattering more realistically:

$$\left(\frac{d\sigma}{d\Omega}\right)_{lab} = \left(\frac{\alpha^2}{4E^2\sin^4\frac{\theta}{2}}\right)\frac{E'}{E}\left\{\begin{array}{c}\left(F_1^2(q^2) - \frac{\kappa^2 q^2}{4M_N^2}F_2^2(q^2)\right)\cos^2\frac{\theta}{2} \\ -\frac{q^2}{2M_N^2}(F_1(q^2)+\kappa F_2(q^2))^2\sin^2\frac{\theta}{2}\end{array}\right\}, \tag{6}$$

where κ is the anomalous magnetic moment measured to be $1.792847337\pm0.000000029$ in the units of μ_N for the proton and -1.9130427 ± 0.0000005 for the neutron [46]. The Dirac ($F_1(q^2)$) and Pauli ($F_2(q^2)$) form factors parametrize the structure of the proton.

In the limit $q^2 \to 0$,

$$\begin{aligned} F_1^{proton}(0) &= 1, \quad F_2^{proton}(0) = 1, \\ F_1^{neutron}(0) &= 0, \quad F_2^{neutron}(0) = 1. \end{aligned} \tag{7}$$

In practice, it is more convenient to use Sach's form factors $G_E(Q^2)$ and $G_M(Q^2)$, which represent electric ($G_E(Q^2)$) and magnetic ($G_M(Q^2)$) momentum-dependent ($Q^2 = -q^2$) structure of the nucleon more explicitly. They are defined as a linear combination of the Dirac form factors:

$$\begin{aligned} G_E &\equiv F_1 - \frac{\kappa Q^2}{4M_N^2}F_2, \\ G_M &\equiv F_1 + \kappa F_2. \end{aligned} \tag{8}$$

Direct experimental measurements [13] are usually given in terms of $G_E(Q^2)$ and

$G_M(Q^2)$. Magnetic form factor dominates the cross section at high momentum transfer, and is well studied experimentally. Electric form factor is more difficult to measure, but it can be obtained using the polarization transfer method [3] giving the proton form factor ratio $\mu_p G_E^p/G_M^p$.

Figure (1) shows published world data for $\mu_p G_E^p/G_M^p$ as a function of the momentum transfer Q^2 in comparison with the fit to the polarization transfer measurements from Jefferson Lab. Open symbols indicate Rosenbluth separations while filled symbols indicate polarization transfer measurements. As one can see, the newer polarization transfer technique gives a ratio which decreases dramatically with increasing momentum transfer, in contrast to previous measurements with the Rosenbluth separation technique. See [13] for more experimental details. For the purposes of our calculations, we are only concerned with the numerical measurement data for a set of relatively low momentum transfers, where the experimental situation is rather clear.

Let us now consider a nucleon as a composite particle made of quarks, and introduce the form factors on the electromagnetic current level.

The nucleon electromagnetic vector current is

$$J_\mu^\gamma = \overline{N}\left(F_1(q^2)\gamma_\mu + i\frac{\kappa F_2(q^2)}{2M_N}\sigma_{\mu\nu}q^\nu\right)N, \tag{9}$$

where $\overline{N}$ and N are nucleon spinors, and the amplitude is given by

$$\mathcal{M}^\gamma = -\frac{4\pi\alpha}{q^2}Q_f l^\mu J_\mu^\gamma. \tag{10}$$

For the case of electron scattering, the leptonic vector current is the Dirac current with electron spinor u_e:

$$l^{\mu} = \overline{u}_e \gamma^{\mu} u_e. \tag{11}$$

Hadronic currents J_{μ} are hadronic matrix elements of the electromagnetic, vector, and axial-vector quark current operators:

$$J_{\mu}^{\gamma} = \langle N \left| \widehat{J}_{\mu}^{\gamma} \right| N \rangle, \tag{12}$$

with $|N\rangle = |p\rangle$ or $|n\rangle$, and

$$\widehat{J}_{\mu}^{\gamma} = \sum_{q} Q_q \overline{u}_q \gamma_{\mu} u_q. \tag{13}$$

Nominally, summation must be done over all quark flavors, but it is sufficient at the momentum scale of interest to include only light quarks, u, d, and s.

Comparing the equations (8), (9), and (13), we can express the form factors in terms of a linear combinations of contributions from different flavors of quarks:

$$G_{E,M} = \frac{2}{3} G_{E,M}^{u} - \frac{1}{3} (G_{E,M}^{d} + G_{E,M}^{s}). \tag{14}$$

1.2.2 Weak Form Factors

Let us consider now the fundamental coupling of an elementary fermion to the Z^0. The weak invariant amplitude is given in [45] as:

$$\mathcal{M}^{Z} = -\frac{4\pi\alpha}{M_Z^2 - q^2} \frac{1}{(4 \sin\theta_W \cos\theta_W)^2} \left(g_V^f l^{\mu} + g_A^f l^{\mu 5} \right) \left(J_{\mu}^{Z} + J_{\mu 5}^{Z} \right), \tag{15}$$

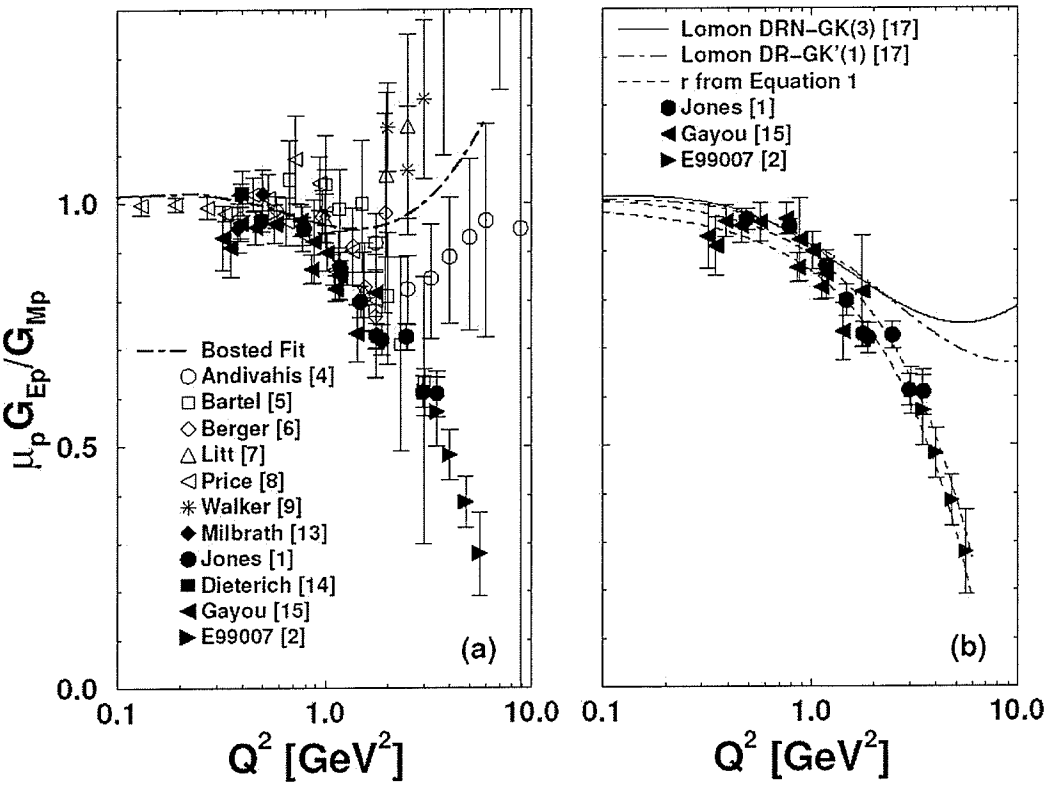

Figure 1: (a) Published world data for $\mu_p G_E^p / G_M^p$ as a function of the momentum transfer Q^2. (b) Fit to the polarization transfer measurements from Jefferson Lab. (Ref. [13])

where l^μ ($l^{\mu 5}$) and J^μ ($J^{\mu 5}$) are leptonic and hadronic vector (axial vector) currents, respectively, and Q_f is the electromagnetic charge number of the fermion. The vector and axial-vector "charges" of the fermions, g_V^f and g_A^f, are defined as

$$\begin{aligned} g_V^f &= 2T_3^f - 4Q_f \sin^2\theta_W, \\ g_A^f &= -2T_3^f, \end{aligned} \tag{16}$$

with $T_3^f = +\frac{1}{2}(-\frac{1}{2})$ for the upper (lower) member of the fermion doublet. For quark and lepton multiplets, see Table 2, Section 2.1.1, or refer to [50] for more detailed explanations.

Explicitly, we have for the electron and the (u, d, s) quarks:

$$\begin{aligned} g_V^e &= -1 + 4\sin^2\theta_W, \qquad g_A^e = +1, \\ g_V^u &= +1 - \frac{8}{3}\sin^2\theta_W, \qquad g_A^u = -1, \\ g_V^{d,s} &= -1 + \frac{4}{3}\sin^2\theta_W, \qquad g_A^{d,s} = +1. \end{aligned} \tag{17}$$

The leptonic axial-vector current is a Dirac current with electron spinor u_e:

$$l^{\mu 5} = \overline{u}_e \gamma^\mu \gamma^5 u_e. \tag{18}$$

Currents J_μ^Z and $J_{\mu 5}^Z$ are defined similarly to Eqs. (12) and (13), as:

$$J_\mu^Z = \langle N \left| \widehat{J}_\mu^Z \right| N \rangle, \tag{19}$$

$$J_{\mu 5}^Z = \langle N \left| \widehat{J}_{\mu 5}^Z \right| N \rangle, \tag{20}$$

where

$$\begin{aligned} \widehat{J}^Z_\mu &= \sum_q g^q_V \overline{u}_q \gamma_\mu u_q, \\ \widehat{J}^Z_{\mu 5} &= \sum_q g^q_A \overline{u}_q \gamma_\mu \gamma_5 u_q. \end{aligned} \tag{21}$$

The axial current of the nucleon is normally defined through the axial form factor G_A :

$$\widehat{J}^Z_{A,\mu} = \overline{N} \left(G_A \gamma_\mu \gamma_5 \right) N. \tag{22}$$

Factoring out the quark charges and using Eq. (17), the neutral weak vector and axial-vector form factors can be written as

$$G^Z_{E,M} = (1 - \frac{8}{3} \sin^2 \theta_W) G^u_{E,M} + (-1 + \frac{4}{3} \sin^2 \theta_W)(G^d_{E,M} + G^s_{E,M}), \tag{23}$$

$$G_A = G^u_A - (G^d_A + G^s_A). \tag{24}$$

Our task is to separate the strange component of the form factors using parity-violating electron scattering measurements at low to medium energies. One of the areas of active theoretical and experimental interest is in understanding the strange quark contribution to nucleon electroweak form factors. The s quarks are a key to the overall sea properties, and their distribution is of particular interest for developing our understanding of quark-quark interactions.

The leading nonzero moments of the strange quark form factors are the most critical for our understanding of the low energy nucleon structure. They are defined as the following:

$$\mu_s \equiv G_M^s(0), \qquad \rho_s \equiv \frac{dG_E^s(\tau)}{d\tau} \mid_{\tau=0}, \tag{25}$$

with

$$\tau = \frac{Q^2}{4M_N^2}. \tag{26}$$

The physical meaning of the strange magnetic moment μ_s is clear, but instead of ρ_s it is more convenient to talk about a strangeness Dirac mean square charge radius $\langle r_s^2 \rangle$, related to G_E^s, ρ_s, and μ_s as

$$\left\langle r_s^2 \right\rangle \equiv -6\frac{dG_E^s(Q^2)}{dQ^2} \mid_{Q^2=0}; \qquad \rho_s \equiv -\frac{2}{3}M_p^2 \left\langle r_s^2 \right\rangle - \mu_s \,. \tag{27}$$

Defined as above, the strangeness Dirac mean square charge radius can be seen as a clear analogy to the regular mean square charge radius of the nucleon.

In spite of active interest and numerous efforts, at present theoretical estimates of μ_s and $\langle r_s^2 \rangle$ span a wide spectrum in both magnitude and sign (see Table 1). Figures (2) and (3) illustrate the same data in a more visual form. As one can see from Fig. (2), the strange magnetic moment is most probably negative on theoretical grounds. As for the the strangeness mean square charge radius, its value is still highly uncertain.

Type of Calculation	μ_s (n.m.)	r^2_s (fm^2)	Year	Ref.
Poles	-0.31 ± 0.09	0.11→ 0.22	1989	1
SU(3) Skyrme (broken)	-0.13	-0.10	1991	2
SU(3) Skyrme (symmetric)	-0.33	-0.19	1991	2
Kaon Loops	-0.026	-0.01	1992	3
Kaon Loops + Vector Meson Dominance	-0.28 ± 0.04	-0.0425 ± 0.0026	1993	4
SU(3) chiral hyperbag	+0.42		1993	5
Kaon Loops	-0.31→ -0.40	-0.032→ -0.027	1994	6
SU(3) chiral colour dielectric	-0.20→ -0.026	-0.003 ± 0.002	1994	7
Kaon Loops	-0.125→ -0.146	-0.022→ -0.019	1995	8
NJR Soliton	-0.05→ +0.25	-0.25→ -0.15	1995	9
Chiral quark-soliton	-0.45	-0.17	1995	10
QCD equalities	-0.75 ± 0.30		1996	11
Poles	-0.24 ± 0.03	0.19 ± 0.03	1996	12
SU(3) chiral soliton	-0.45	-0.35	1996	13
Loops	+0.035	-0.04	1996	14
Poles	0.003	0.002	1997	15
Poles	-0.185 ± 0.075	0.14 ± 0.06	1997	16
Dispersion	-0.10→ -0.14	0.21→ 0.27	1997	17
SU(3) Skyrme (broken)	+0.36		1997	18
Chiral models	-0.25, -0.09	0.24	1997	19
Lattice (quenched)	-0.36 ± 0.20	-0.06→ -0.16	1998	20
SU(3) algebra	0.41 ± 0.18		1998	21
Heavy Baryon ChPT	0.18 ± 0.34	0.05 ± 0.09	1999	22
Lattice (chiral)	-0.16 ± 0.18		2000	23
Chiral Quark Model	-0.046		2000	24
Lattice QCD	-0.28 ± 0.10		2000	25
SU(3) chiral quark-soliton *with kaon asymptotics*	0.115	-0.095	2001	26
SU(3) chiral quark-soliton *with pion asymptotics*	0.074	-0.220	2001	26
Perturbative CQM	-0.048 ± 0.012	-0.011 ± 0.003	2002	27

Table 1: Theoretical predictions for the strange magnetic moment and the strangeness radius of the nucleon, in chronological order.

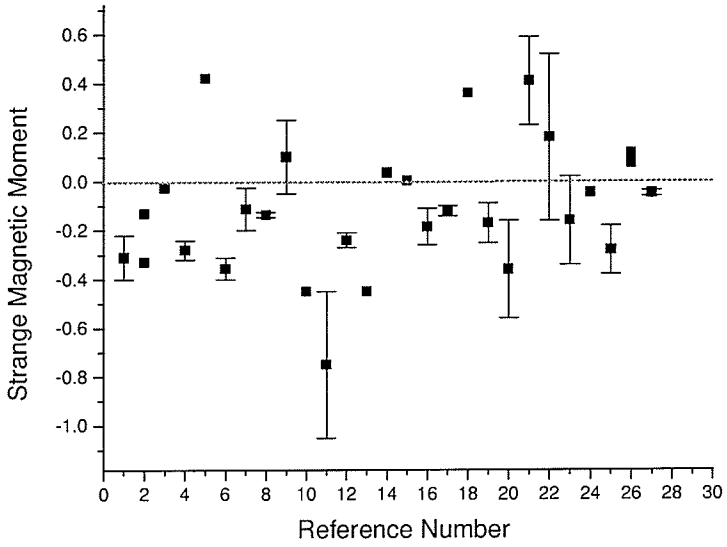

Figure 2: Model values for the strange magnetic moment, from Table 1.

1.2.3 Form Factors in Terms of Quark Contributions

Let us now review and summarize the content of the previous two sections with the emphasis on the individual quark contributions. The physics interest is that, with some approximations, one can extract the individual contributions of the different quark flavors to the measured proton form factors. The electromagnetic form factors of the proton and the neutron, and the weak form factor of the proton can be expressed in terms of quark contributions [9]:

Ref. #	Publication
1	R. L. Jaffe, Phys. Lett. B229, 275 (1989)
2	N. W. Park, J. Schechter, and H. Weigel, Phys. Rev. D43, 869 (1991)
3	W. Koepf, E. M. Henley, and S. J. Polloch, Phys. Lett. B288, 11 (1992)
4	T. D. Cohen, H. Forkel, and M. Nielson, Phys. Lett. B316, 1 (1993)
5	S. Hong and B. Park, Nucl. Phys. A561, 525 (1993)
6	M. J. Musolf and M. Burkardt, Z. Phys. C61, 433 (1994)
7	S. C. Phatak and Sarira Sahu, Phys. Lett. B321, 11 (1994)
8	H. Ito, Phys. Rev. C52, R1750 (1995)
9	H. Weigel, et al., Phys. Lett. B353, 20 (1995)
10	H. C. Kim et al., hep-ph/9506344, Report-no: RUB-TPII-11/95
11	D. Leinweber, Phys. Rev. D53, 5115 (1996)
12	H.-W. Hammer, U.-G. Meissner, and D. Drechsel, Phys. Lett. B367, 323 (1996)
13	C. V. Christov et al., Prog. Part. Nucl. Phys. 37, 1 (1996)
14	P. Geiger and N. Isgur, hep-ph/9610445, Phys.Rev. D55, 299-310 (1997)
15	U.-G. Meissner et al., Phys.Lett. B408, 381-386 (1997)
16	H. Forkel, Phys. Rev. C56, 510 (1997)
17	M. J. Musolf, H.-W. Hammar, and D. Drechsel, Phys. Rev. D55, 2741 (1997)
18	S-T. Hong, B-Y. Park, and D-P. Min, Phys.Lett. B414, 229 (1997)
19	M. J. Ramsey-Musolf and H. Ito, Phys. Rev. C55, 3066 (1997)
20	S. J. Dong, K. F. Liu, and A. G. Williams, Phys. Rev. D58, 074504 (1998)
21	H.-Ch. Kim et al., Phys. Rev. D58, 114027 (1998)
22	T. R. Hemmert, B. Kubis, and Ulf-G. Meissner, Phys. Rev. C60, 045501 (1999)
23	D. B. Leinweber and A. W. Thomas, Phys. Rev. D62, 074595 (2000)
24	L. Hannelius and D. O. Riska, Phys. Rev. C62, 045204 (2000)
25	N. Mathur and S.-J. Dong, Nucl. Phys. Proc. Suppl. 94, 311 (2001)
26	A. Silva, H.-C. Kim, and K.Goeke, Phys.Rev. D65, 014016 (2002); Erratum-ibid. D66, 039902 (2002)
27	V. E. Lyubovitskij et al., Phys.Rev. C66, 055204 (2002)

Table 2: References for Table 1 and Figures 2 and 3.

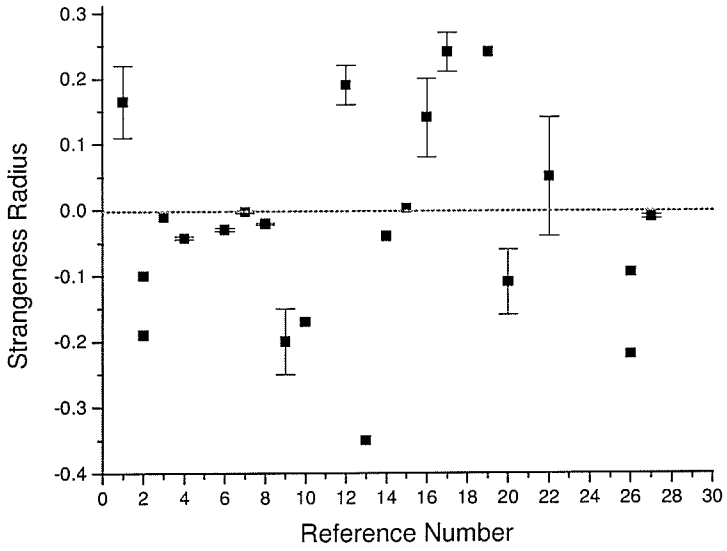

Figure 3: Model values for the strangeness radius, from Table 1.

$$G_{E,M}^{\gamma,p} = \sum_q Q_q G_{E,M}^{q,p}, \tag{28}$$

$$G_{E,M}^{\gamma,n} = \sum_q Q_q G_{E,M}^{q,n}, \tag{29}$$

$$G_{E,M}^{Z,p} = \sum_q (\frac{1}{2}T_j^3 - Q_q \sin^2\theta_W) G_{E,M}^{q,p}, \tag{30}$$

where $q = u, d$ or s , Q_q is the electric charge of each quark $(2/3, -1/3, -1/3$ respectively), $(\frac{1}{2}T_j^3 - Q_q \sin^2\theta_W)$ is the weak charge and T_j^3 is the weak isospin $(1/2, -1/2, -1/2$ respectively). If now we suppose isospin symmetry (interchanging u and d quarks will transform a neutron into a proton and vice versa):

$$G_{E,M}^{u,p} = G_{E,M}^{d,n}, \tag{31}$$

$$G_{E,M}^{d,p} = G_{E,M}^{u,n}, \tag{32}$$

$$G_{E,M}^{s,p} = G_{E,M}^{s,n}, \tag{33}$$

we obtain from Eqs. (28) - (33) an expression of the contribution of the quark flavors to the proton form factors in terms of measurable quantities:

$$G_{E,M}^{u,p} = (3 - 4\sin^2\theta_W) G_{E,M}^{\gamma,p} - 4G_{E,M}^{Z,p}, \tag{34}$$

$$G_{E,M}^{d,p} = (2 - 4\sin^2\theta_W) G_{E,M}^{\gamma,p} + G_{E,M}^{\gamma,n} - 4G_{E,M}^{Z,p}, \tag{35}$$

$$G_{E,M}^{s,p} = (1 - 4\sin^2\theta_W) G_{E,M}^{\gamma,p} - G_{E,M}^{\gamma,n} - 4G_{E,M}^{Z,p}. \tag{36}$$

As the s quarks are a key to the overall sea properties, strange form factors describing their distribution are of particular interest for developing our understanding of low energy nucleon structure.

1.3 Parity Violating Electron Scattering

At "tree level", the electron-nucleon scattering amplitude consists of two terms, $\mathcal{M}^\gamma$ (Fig. 3a) and $\mathcal{M}^Z$ (Fig. 3b).

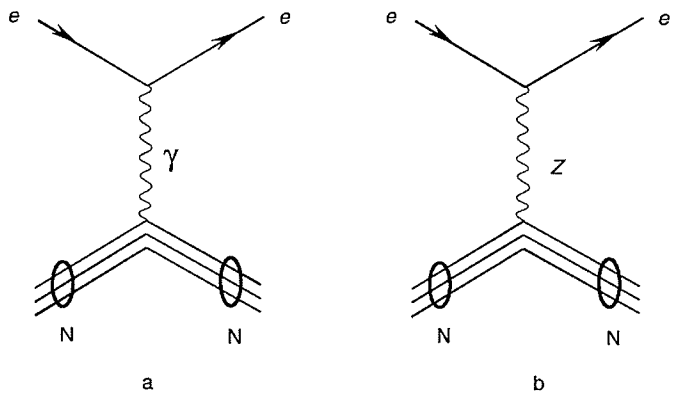

Figure 4: Tree level electron-nucleon scattering.

The first term is parity-conserving γ-exchange, and the second has a parity-violating contribution from Z^0-exchange. The differential cross section is proportional to

$$d\sigma \sim \left|\mathcal{M}^\gamma + \mathcal{M}^Z\right|^2 = |\mathcal{M}^\gamma|^2 + 2\mathrm{Re}\left\{(\mathcal{M}^\gamma)^* \mathcal{M}^Z\right\} + \left|\mathcal{M}^Z\right|^2. \tag{37}$$

The purely weak term $\left|\mathcal{M}^Z\right|^2$ is very small compared to the other terms and can

safely be neglected. The electromagnetic-weak interference term $2\mathrm{Re}\left\{(\mathcal{M}^{\gamma})^{*}\,\mathcal{M}^{Z}\right\}$ contains the physics of interest. This term can be extracted from the parity-violating asymmetry, formed as the ratio of helicity-dependent to helicity-independent cross sections:

$$\mathcal{A} = \frac{d\sigma_R - d\sigma_L}{d\sigma_R + d\sigma_L}. \tag{38}$$

Here, $d\sigma_R$ and $d\sigma_L$ are partial cross sections for right- and left-handed electrons, respectively. This ratio, measured in a number of experiments, is of the order 10^{-6} at low energies.

For elastic electron-nucleon scattering, the asymmetry is given by [45, 7]

$$\begin{aligned}\mathcal{A} &= \left[\frac{-G_F Q^2}{4\sqrt{2}\pi\alpha}\right] \frac{\varepsilon G_E^{\gamma} G_E^{Z} + \tau G_M^{\gamma} G_M^{Z} - (1-4\sin^2\theta_W)\varepsilon' G_M^{\gamma} G_A^{Z}}{\varepsilon (G_E^{\gamma})^2 + \tau (G_M^{\gamma})^2} \\ &\equiv -\frac{G_F Q^2}{4\sqrt{2}\pi\alpha} \times \frac{N}{D},\end{aligned} \tag{39}$$

where $Q^2 > 0$ is the four-momentum transfer. G_E^{γ} and G_M^{γ} are the electric and magnetic vector form factors of the nucleon associated with γ-exchange, G_E^{Z} and G_M^{Z} are the similar parameters for Z^0-exchange, and G_A^{Z} is the axial vector form factor. Kinematic parameters τ, ε and ε' are defined as

$$\begin{aligned}\tau &= \frac{Q^2}{4M_N^2}, \\ \varepsilon &= \frac{1}{1+2(1+\tau)\tan^2\frac{\theta}{2}}, \\ \varepsilon' &= \sqrt{\tau(1+\tau)(1-\varepsilon^2)}.\end{aligned} \tag{40}$$

The electromagnetic vector form factors of the proton $G_E^{\gamma,p}$ and $G_M^{\gamma,p}$ are well measured, and some constraints can be put on $G_E^{\gamma,n}$ and $G_M^{\gamma,n}$ for the neutron [13]. The expressions for the weak form factors of the nucleon, G_E^Z and G_M^Z, and the axial vector coupling G_A^Z, are given below. The factor $(1 - 4\sin^2\theta_W) \simeq 0.1$ suppresses the term containing G_A^Z, and makes the contribution of higher order processes more apparent.

The neutral weak vector form factors for the proton and neutron can be expressed in terms of the electromagnetic form factors of the proton and neutron, plus a contribution from strange quarks [10]. We choose to write this in the form

$$\begin{aligned} G_{E,M}^Z &= (1 - 2\sin^2\theta_W)\left[1 + R_V^{T=1}\right] G_{E,M}^{T=1}\tau_3 \\ &\quad -2\sin^2\theta_W \left[1 + R_V^{T=0}\right] G_{E,M}^{T=0} - \left[1 + R_V^{(0)}\right] G_{E,M}^s. \end{aligned} \tag{41}$$

Here $R_V^{T=0}$, $R_V^{T=1}$, and $R_V^{(0)}$ are the isoscalar, isovector, and isosinglet weak radiative corrections describing the contribution from weak vector couplings beyond tree level, respectively. Strong isospin τ_3 is equal to $+1(-1)$ for the proton (neutron). The isoscalar and isovector electromagnetic form factors are taken to be the linear combinations

$$\begin{aligned} G_{E,M}^{T=0} &= G_{E,M}^p + G_{E,M}^n, \\ G_{E,M}^{T=1} &= G_{E,M}^p - G_{E,M}^n, \end{aligned} \tag{42}$$

so that at $Q^2 = 0$, $G_E^{T=0}(0) = G_E^{T=1}(0) = 1$, and $G_M^{T=0}(0) = 0.8797$, $G_M^{T=1}(0) = 4.709$.

The strange quark form factors are undetermined, but take on the values $G_E^s(0) = 0$ and $G_M^s(0) = \mu_s$, where μ_s is the contribution of strange quarks to the magnetic moment of the nucleon.

The axial vector form factor is conveniently written in terms of octet matrix elements [45] as

$$G_A^Z = -\left[1 + R_A^{T=1}\right] G_A^{T=1}\tau_3 + \sqrt{3} R_A^{T=0} G_A^{(8)} + \left[1 + R_A^{(0)}\right] G_A^s. \tag{43}$$

The isovector axial form factor $G_A^{T=1}$ is determined from neutron beta decay as $G_A^{T=1}(0) = g_A$, with $g_A = 1.2670 \pm 0.0035$. The second term involving the $SU(3)$ isoscalar octet form factor $G_A^{(8)}$ is not present at tree level. From a least squares fit to hyperon beta decay, we have determined $G_A^{(8)} = 0.169 \pm 0.009$, which is consistent with results of polarized deep inelastic lepton scattering [17]. In our calculations (see section IV) we find $|R_A^{T=0}| < |R_A^{T=1}|$, so we expect overall that the second term in Eq. (43) is suppressed relative to the first term. The axial strange form factor G_A^s is extracted from polarized deep inelastic lepton scattering as $G_A^s(Q^2 = 0) = -0.086 \pm 0.024$ [17]. Due to the unknown Q^2 dependence we take $G_A^s(Q^2 = 0.1) = -0.086 \pm 0.086$ in our analysis.

Additional information on the axial vector form factor can be provided by parity-violating quasielastic scattering from deuterium. In the simplest impulse approximation, the asymmetry for the deuteron can be written as the incoherent sum of neutron

and proton contributions

$$\mathcal{A}_d = \left[\frac{-G_F Q^2}{4\sqrt{2}\pi\alpha}\right] \frac{N_n + N_p}{D_n + D_p}, \tag{44}$$

where $N_p(N_n)$ is the numerator and $D_p(D_n)$ is the denominator in Eq. (39) for the proton (neutron).

The neutral weak axial form factor as measured in electron scattering includes anapole contributions and a class of electroweak radiative corrections that are absent in neutrino scattering.

1.4 Experiments

1.4.1 SAMPLE I and SAMPLE II

The first experiment to measure the weak neutral magnetic form factor G_M^s of the nucleon is the SAMPLE experiment at the Bates Linear Accelerator Center. The SAMPLE I experiment involves scattering 194 MeV polarized electrons from protons, and SAMPLE II refers to scattering the same beam from deuterium. It is the combination of results from both these experiments that allows us to separate G_M^s and G_A^e contributions, so it is convenient to describe SAMPLE I & II in the same section.

The details of the techniques employed in these experiments are available in Refs. [7, 10, 41]. The scattered electrons are detected in a large solid angle of ~ 1.5 sr

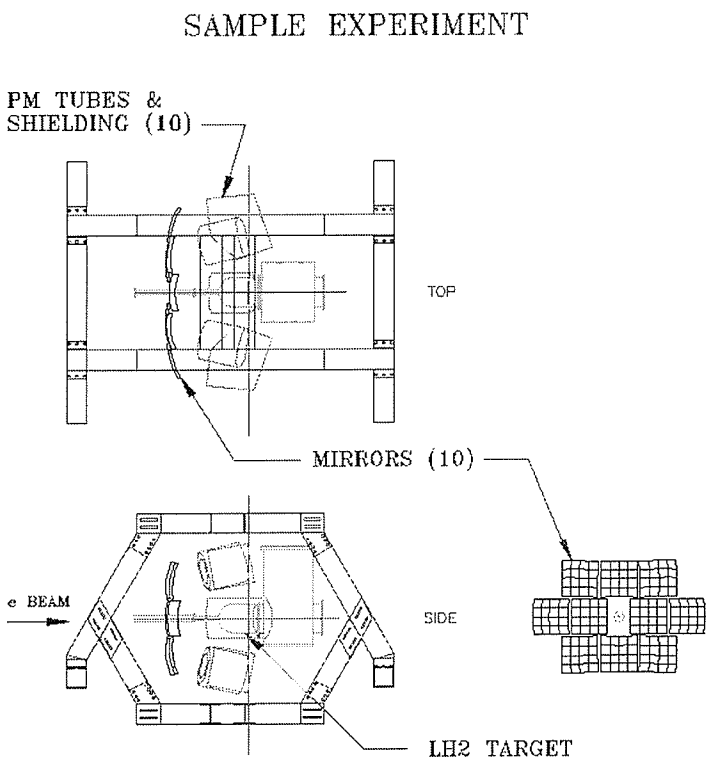

Figure 5: The layout of the SAMPLE target and detector system. (Ref. [51])

at 4 backward angles $138° < \theta < 160°$, which results in an average $Q^2 \simeq 0.1$ (GeV/c)^2.

The polarized electron source is a bulk GaAs photoemission source, with polarization typically 35%. The detector consists of 10 large ellipsoidal mirrors that reflect the Cerenkov light into 20.32 cm diameter photomultiplier tubes.

For SAMPLE II, a separate measurement was performed with the same apparatus but with a deuterium target.

The measured proton and deuteron asymmetries for $Q^2 = 0.1$ GeV^2 and $\theta_{\text{avg}} =$

146.2° are (in ppm):

$$A_p^{\rm exp} = -4.92 \pm 0.61 \pm 0.73, \quad (45)$$

$$A_d^{\rm exp} = -6.97 \pm 0.64 \pm 0.55. \quad (46)$$

The first uncertainty is statistical while the second is systematic. According to these data, the size of the electroweak radiative corrections to the axial form factor is significantly larger than anticipated from theory [57].

The original values have been subsequently re-analyzed at least twice. In 2001, Spayde [54] reexamined the data to find two significant corrections. The first arises from a different treatment of the electromagnetic radiative corrections, while the second is a correction for the fraction of the detector signal due to pions. Each correction increases A_p and A_d by about 4 percent, resulting in quoted asymmetries of

$$A_p^{\rm exp} = -5.61 \pm 0.67 \pm 0.88, \quad (47)$$

$$A_d^{\rm exp} = -7.28 \pm 0.68 \pm 0.75. \quad (48)$$

The latest re-examination by the SAMPLE collaboration [30] resulted in a further increase in magnitude of the deuteron asymmetry:

$$A_d^{\rm exp} = -7.77 \pm 0.73 \pm 0.62. \quad (49)$$

The deuteron is affected the most by correction for coherent π^0 photoproduction. Additional increases came from the improved determination of the scintillation

component of the detector signal.

1.4.2 SAMPLE III

In order to confirm the SAMPLE II observations with a measurement that has an improved signal-to-background ratio, a new measurement of the parity-violating asymmetry in electron scattering on deuterium with lower beam energy of 125 MeV has been carried out [30]. As was the case for SAMPLE II, the dominant scattering process is quasielastic scattering. Using a 125 MeV electron beam yielding $Q^2 \simeq 0.038$ GeV^2 resulted in roughly the same sensitivity but very different systematics. The asymmetry was further corrected for the beam polarization, the background dilution, and electromagnetic radiative effects to obtain the following physical asymmetry:

$$A_d^{\text{exp}} = -3.51 \pm 0.57 \pm 0.58. \tag{50}$$

1.4.3 HAPPEX I

The HAPPEX experiment [7, 4] utilized the two spectrometers in Hall A at Jefferson Lab (JLab) to measure the asymmetry in elastic electron-proton scattering at small forward angles. The HAPPEX I experiment used $E_{electron} = 3.2$ GeV and $\Theta_{electron} = 12.3°$ yielding $Q^2 \simeq 0.477$ GeV^2.

The measured asymmetry is

$$A_p^{\text{exp}} = -14.60 \pm 0.94 \pm 0.54, \tag{51}$$

where again the first uncertainty is statistical and the second is systematic.

Because this asymmetry was measured at a forward angle, it is in principle sensitive to three unmeasured form factors: G_E^s, G_M^s, and G_A^e. The axial contribution is very small at this kinematics, becoming zero at 0°. Assuming the calculated value from [57] is correct, G_A^e should not contribute more that 4% to the total asymmetry. The other two form factors enter in the linear combination $G_E^s + 0.392 G_M^s$.

Thus, we have

$$\frac{G_E^s + 0.392 G_M^s}{G_M^p/\mu_p} = 0.091 \pm 0.054 \pm 0.039, \tag{52}$$

where the first uncertainty is a combination of the statistical and systematic errors in the asymmetry combined in quadrature with the uncertainty in G_A^e, and the second is due to the uncertainty in the electromagnetic form factors. As was stated in Part 2 of this chapter, completely reliable values are still not available for the neutron electric G_E^n and magnetic G_M^n form factors. Unfortunately, the result is sensitive to them, especially to G_M^n. For example, using the results from a different G_M^n measurement [14] to interpret the Happex data, yields

$$\frac{G_E^s + 0.392 G_M^s}{G_M^p/\mu_p} = 0.146 \pm 0.054 \pm 0.047. \tag{53}$$

1.4.4 HAPPEX II

The HAPPEX II experiment was approved at JLab with an "A" rating and will probably run starting in October 2004. It will measure the parity violating (PV) asymmetry in the elastic scattering of 3.2 GeV electrons from a liquid Hydrogen target at a scattering angle of $\Theta_{electron} = 6°$, corresponding to an average $Q^2 \simeq 0.1$ GeV^2 [33]. The very forward scattering angle will be achieved by utilizing new septum magnets placed in front of the existing high-resolution spectrometers.

The physics asymmetry is estimated to be about $A_{LR} = -1.63$ ppm. With 100 μA electron beam and a polarization of 75%, a statistical error of 4.6% and a projected systematic error of 2.9% can be achieved in 700 hours of data taking.

The HAPPEX II measurement would access the linear combination $\rho_s + \mu_p \mu_s$ to an accuracy of ± 0.31 and would provide a direct sensitive constraint on the nucleon strangeness radius. In terms of form factors, HAPPEX II will measure the linear combination $G_E^s + 0.08 G_M^s$.

1.4.5 G0

The goal of the Jefferson Lab G0 experiment is to measure forward proton asymmetries and backward asymmetries for both proton and deuteron targets in order to provide a complete set of observables from which charge, magnetic and axial neutral weak form factors of the nucleon can be determined. Measuring asymmetries at both

forward and backward scattering angles makes it possible to separate the contributions of each quark flavor to the charge and magnetic form factors. In addition, the effective axial form factor can be extracted by measuring quasi-elastic asymmetries on a deuterium target at a backward angle. The axial current of the $N\Delta$ transition will be also be measured by detecting in addition the inelastic electrons in the backward scattering experiment.

The experiment will be performed in Hall C using a dedicated setup (see Ref. [8], [18] for more details). The spectrometer consists of an eight sector superconducting toroidal magnet which will focus recoil protons (forward scattering measurement) or electrons (backward measurement) from a 20 cm long liquid hydrogen or deuterium target to pairs of plastic scintillator detectors. In the forward angle measurement, time-of-flight will be used to separate elastic protons from background using a pulsed 40 μA , 70% polarized beam current (31.25 MHz rather than 499 MHz) and custom time digitization electronics. In the backward angle experiment, the pairs of scintillators are spatially separated to allow momentum and angle measurement. The range of momentum transfers accessible with this apparatus is from about 0.1 GeV^2 to 1 GeV^2.

In the first G0 experiment, which took its first data in the spring of 2004, forward angle asymmetries are measured by detecting the recoil protons from elastic scattering. For this "forward mode", the beam energy is 3.2 GeV and Q^2 covers the entire

range of 0.1 to 1 GeV^2. The scattered protons are detected at $\Theta_{proton} = 70° \pm 10°$.

Backward angle asymmetries will be measured by reversing the same apparatus relative to the beam direction. The "backward mode" uses the same beam energy and scattering angles for both proton and deuteron targets. The scattered electrons are detected at $\Theta_{electron} \simeq 110°$. A set of smaller scintillators will be installed near the exit window of the cryostat to discriminate elastic and inelastic electrons.

The following beam energy and corresponding momentum transfers are going to be used at the "backward mode":

E_{beam} (MeV)	Q^2 (GeV^2)
424	0.3
576	0.5
799	0.8

1.4.6 A4

As well as G0, the PV A4 experiment at the MAMI accelerator in Mainz is being mounted with dedicated apparatus to address the question of the weak neutral current in the nucleon. It will measure both forward and backward asymmetries using an array of PbF_2 calorimeter crystals. The Mainz proposal (Ref.[1]) is directed towards a measurement of the strange contribution to the Dirac form factor $F_1(Q^2)$ of the

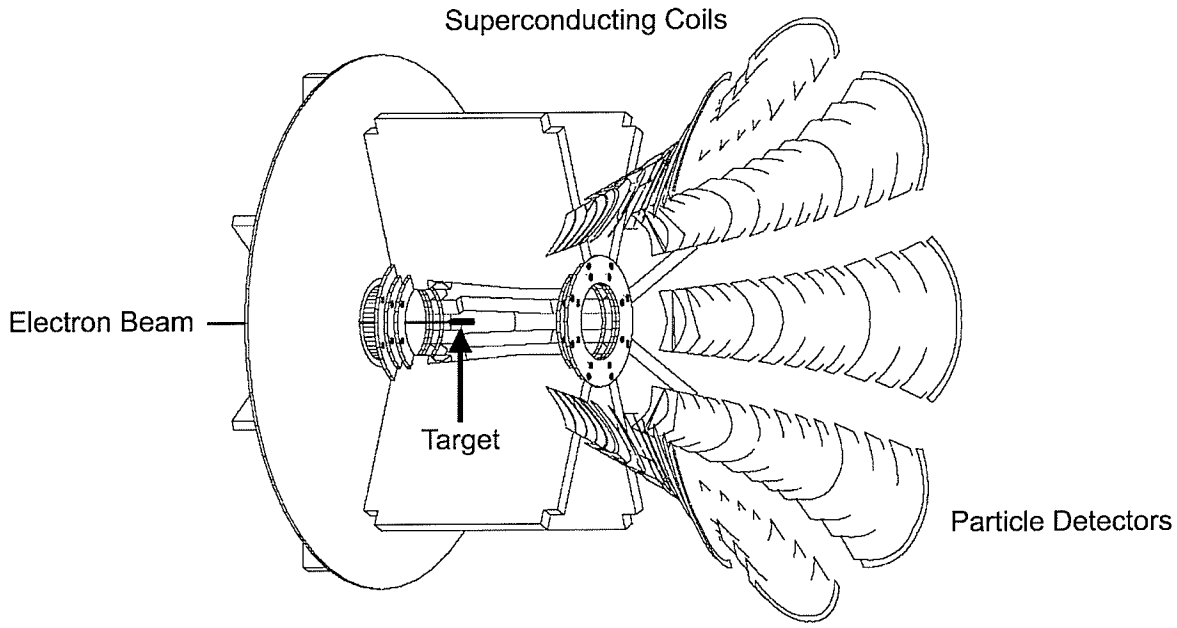

Figure 6: Schematic of the G0 Experiment. (Ref. [7])

proton at low four-momentum transfer. This forward angle asymmetry will yield a measurement of the linear combination of strange electric and strange magnetic form factors G_E^s and G_M^s. The measurement began in summer 2000. Up to the moment, the measurements were done at 854.3 MeV and 570 MeV electron beam energy, which led to the momentum transfers of 0.23 GeV^2 and 0.1 GeV^2, correspondingly; with the detector covering the angular range from 30° to 40°.

With a liquid hydrogen target, a beam intensity of 20 μA and a detector of $\Omega = 0.8$ sr the total number of elastic scattering events of $N_{tot} = 4.8 \times 10^{13}$ can be obtained in 1500 hrs. If a beam polarization of 80% is assumed, this would correspond to a measurement of $\delta(F_1 + 0.12F_2)$ to ± 0.011. Most of the current models for F_1 predict values of 0.05 to 0.1

The detector for the experiment consists of 1022 PbF_2 calorimeter crystals arranged in a pointing geometry relative to the target as shown in Figure 7. All shieldings, cryogenic and vacuum equipment are omitted.

It consists of six rings of 64 modules sized $5.4 \times 5.4 \times 39$ cm^3 of liquid Xe. It is designed to handle the substantial background from inelastic electron scattering, Moeller pairs and μ-decays. The resolution of $\sigma_E/E = 3\%/\sqrt{E(\text{GeV})}$ can be achieved by collecting the scintillation light. The fast Cerenkov signal from the PbF_2 allows effective separation of elastic and inelastic electrons in hardware. The same apparatus can be reversed relative to the beam to provide corresponding asymmetries over a

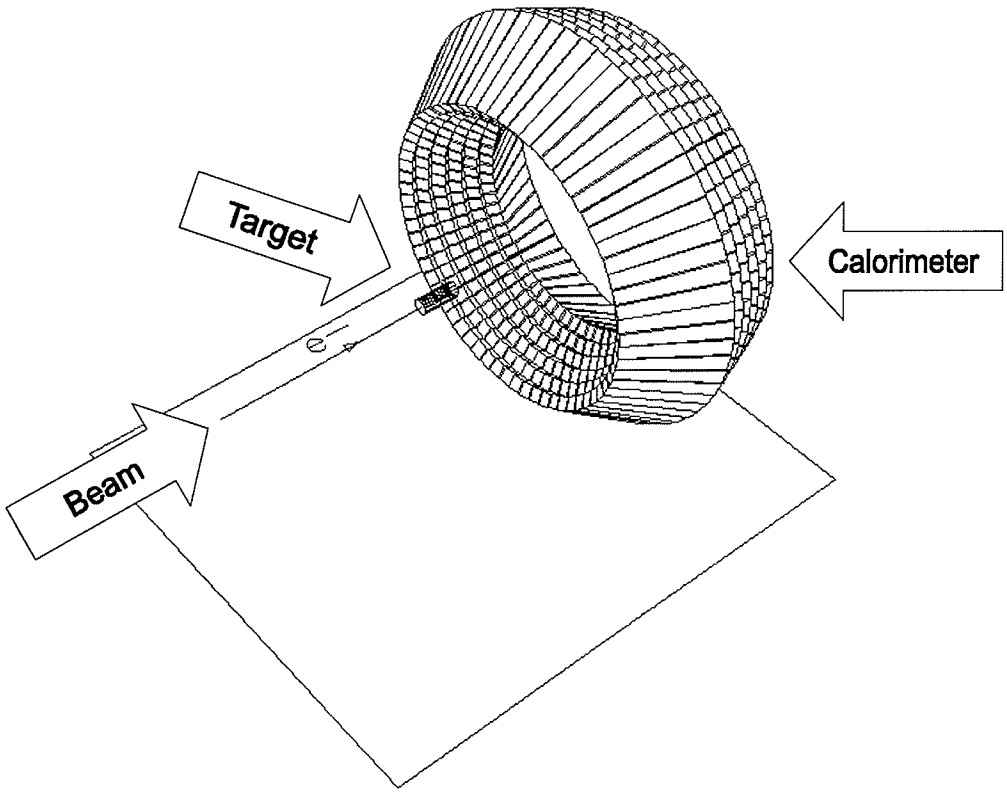

Figure 7: Schematic view of a calorimetric detector for the Mainz parity experiment.

(Ref. [7])

range of momentum transfers at backward angle of 145°.

1.4.7 Q_{weak}

A general purpose of the Q_{weak} experiment is to search for new physics challenging predictions of the Standard Model.

The Standard Model evolution predicts a shift of $\Delta \sin^2\theta_W = +0.007$ at low Q^2 with respect to the Z^0 pole best fit value of 0.23113 ± 0.00015 (Fig. 8). The solid line shows the running $\sin^2\theta_W$ of according to Modified Minimal Subtraction scheme ($\overline{MS}$) The reduced slope indicated by the dashed line is given by Minimal Supersymmetric (SUSY) Standard Model. The solid dots show the existing measurement results from atomic parity violation (APV), deep inelastic neutrino-nucleus scattering (NuTeV), and from Z^0 pole asymmetries (LEP+SLC). The open symbols with arbitrary chosen vertical location refer to the asymmetry measurements proposed for Q_{weak} and E-158 experiments.

The weak mixing angle at that energy scale close to the Z^0 pole was measured very precisely. A precision experimental study of the evolution of $\sin^2\theta_W$ to lower energies still has to be carried out. As one can see from Fig. 8, currently there are only two off-peak measurements.

At tree level,

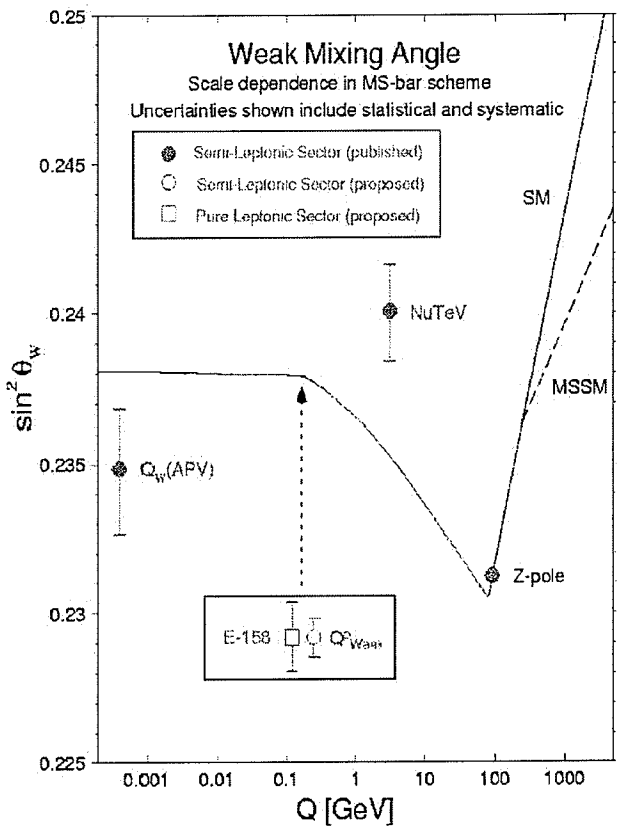

Figure 8: Calculated running of the weak mixing angle in the Standard Model. (Ref. [32])

$$Q^p_{weak} = 1 - 4\sin^2\theta_W \tag{54}$$

and, thus, has a definite prediction in the electroweak Standard Model. The proton's weak charge Q^p_{weak} is also a well-defined experimental observable. At $Q^2 \to 0$ and $\theta \to 0$ the asymmetry can be parameterized as

$$\mathcal{A} = \left[\frac{-G_F Q^2}{4\sqrt{2}\pi\alpha}\right][Q^2 Q^p_{weak} + Q^4 B(Q^2)], \tag{55}$$

where $B(Q^2)$ is a function of form factors $G^\gamma_{E,M}$ and $G^Z_{E,M}$.

At JLab, the Q_{weak} collaborators [32] propose a new precision measurement of parity violating electron scattering on the proton at very low Q^2 and forward angles. According to [32], "A unique opportunity exists to carry out the first precision measurement of the proton's weak charge, $Q^p_{weak} = 1 - 4\sin^2\theta_W$ building on technical advances that have been made in JLab's parity violation program."

The parity violating asymmetry in elastic $e - p$ scattering at $Q^2 = 0.028$ GeV^2 will be measured employing 180 μA of 80% polarized beam of $E_{beam} = 1.165$ GeV on a 35 cm liquid hydrogen target. This 2200 hour measurement will allow to determine the proton's weak charge with $\simeq$4% combined statistical and systematic errors. The electrons are collimated to $\theta_e = 9^\circ \pm 2^\circ$.

The high quality data on form factors provided (hopefully) by the described above PV experiments HAPPEX I, HAPPEX II, and G^0, plus HAPPEX ^4He, will be used to

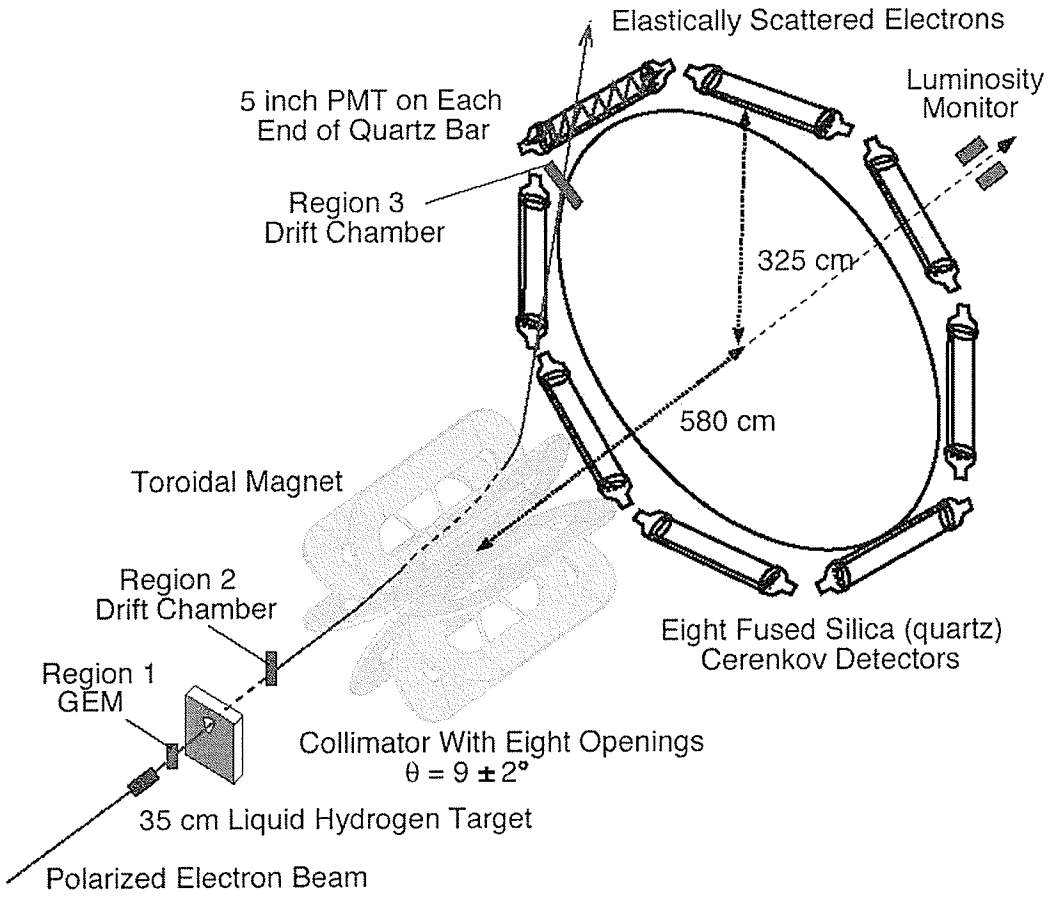

Figure 9: Schematic diagram of the Q_{weak} experiment set-up. (Ref. [49])

determine the contributions of hadronic structure to the planned Q_{weak} measurement.

2 Radiative Effects

2.1 Formalism

2.1.1 Standard Model

The Glashow-Salam-Weinberg model [20], originally developed for leptons, has become the "Standard Model" of electroweak interactions after being successfully extended to the hadronic sector by incorporating the concept of Cabbibo-Kobayashi-Maskawa (CKM) mixing. The Standard Model is the most comprehensive formulation of a theory of the unified electroweak interaction at present [27]. It is theoretically consistent and in agreement with all known phenomena of electroweak origin.

The electroweak Standard Model is a non-abelian gauge theory based on the gauge group $SU(2) \times U(1)$ where the ideas of Yang-Mills theories, isospin invariance, spontaneous symmetry breaking, and Higgs mechanism merge in one common framework. The renormalizability of this class of theories was proven by 't Hooft in 1971 [28]. This frame gives the possibility to perform perturbative calculations for measurable quantities order by order, using a few input parameters. The input parameters themselves cannot be predicted but have to be taken from appropriate experiments.

The renormalizability makes it possible to calculate the higher order quantum

effects (i.e. radiative corrections) to the processes accessible by experimental facilities. Such processes include the weak decays of particles, neutrino-lepton and neutrino-nucleon scattering, electron-nucleon scattering, and electron-positron annihilation. If hadrons are involved, the basic electroweak processes are considered to be the corresponding subreactions at the level of quarks as their constituents. Thus, these kinds of fundamental reactions are all the types of 4-fermion processes.

Electroweak processes between fermions can essentially be described with the help of three input parameters, besides the masses of the fermions themselves and CKM mixing angles: the non-abelian $SU(2)$ gauge coupling constants g_2, abelian $U(1)$ coupling g_1, and the Higgs field vacuum expectation value v. This set can be replaced by any other set of three independent parameters, having theoretical relations to the previous set. Since the input parameters eventually have to be taken from experiment, it is practical to choose a set of more or less well measured quantities.

One such set of input parameters would be [46]:

– the fine structure constant $\alpha = 1/137.03599976(50)$

– the Fermi coupling constant $G_\mu = 1.16639(1) \times 10^{-5}$ GeV^{-2}

– the Weinberg mixing angle $\sin^2\theta_W = 0.23113(15)$ (Z-pole, $\overline{MS}$ renormatization).

Another possible choice of input parameters could include the masses of $W^\pm$ and

Z bosons:

$$M_W^2 = \frac{\pi\alpha}{\sqrt{2}G_\mu \sin^2\theta_W} \tag{56}$$

$$\frac{M_W^2}{M_Z^2} = 1 - \sin^2\theta_W \tag{57}$$

The lowest order description of 4-fermion process starts with the classical Lagrangian. According to the general principles of constructing a gauge invariant field theory with a spontaneous symmetry breaking mechanism, the electroweak classical Lagrangian consists of following gauge, Higgs, and fermion parts [27]:

$$L_{classical} = L_{gauge} + L_{Higgs} + L_{fermion}. \tag{58}$$

The gauge Lagrangian L_{Gauge} is formed from the isotriplet of vector fields $\overrightarrow{W_\mu} = (W_\mu^1, W_\mu^2, W_\mu^3)$ (we will use notation W_μ^a, $a = 1, 2, 3$) and the isosinglet vector field B_μ transforming under a gauge transformation according to the adjoint representation of the gauge group $SU(2) \times U(1)$, leading to the field strength tensors

$$W_{\mu\nu}^a = \partial_\mu W_\nu^a - \partial_\nu W_\mu^a - g_2\epsilon^{abc}W_\mu^b W_\nu^c, \tag{59}$$

$$B_{\mu\nu} = \partial_\mu B_\nu - \partial_\nu B_\mu. \tag{60}$$

Using the field tensors Eq. (59), we can form the pure gauge field Lagrangian:

$$L_{gauge} = -\frac{1}{4}W_{\mu\nu}^a W^{\mu\nu,a} - \frac{1}{4}B_{\mu\nu}B^{\mu\nu}. \tag{61}$$

Now let us consider the Higgs field components. The electric charge operator Q is built from the generators $\overrightarrow{T}$ of the weak isospin and the weak hypercharge Y:

$$Q = T_{w3} + \frac{Y}{2}. \tag{62}$$

T_{w3} is assigned a quantum number of $+\frac{1}{2}(-\frac{1}{2})$ for the upper (lower) component of left-handed fermion doublets of Table 3 and zero for all right-handed fermions.

For spontaneous breaking of the $SU(2) \times U(1)$ symmetry leaving the electromagnetic gauge subgroup $U(1)$ unbroken, a single complex scalar doublet field with hyper charge $Y = 1$

$$\Phi(x) = \begin{pmatrix} \phi^+(x) \\ \phi^0(x) \end{pmatrix} \tag{63}$$

is coupled to the gauge fields

$$L_{Higgs} = (D_\mu \Phi)^* (D^\mu \Phi) - V(\Phi). \tag{64}$$

with the covariant derivative

$$D_\mu = \partial_\mu - i g_2 T_a W_\mu^a + i \frac{g_1}{2} B_\mu. \tag{65}$$

The Higgs field self-interaction is constructed in a way that it gives rise to spontaneous symmetry breaking:

$$V(\Phi) = -\mu^2 \Phi^+ \Phi + \lambda (\Phi^+ \Phi)^2. \tag{66}$$

Here, coefficients μ and λ are related to the non-vanishing vacuum expectation value

υ as

$$\upsilon = \frac{\mu}{\sqrt{\lambda}}. \tag{67}$$

Using Eq. (67), let us re-write Eq. (63) in the following way:

$$\Phi(x) = \begin{pmatrix} \phi^+(x) \\ (\upsilon + H(x) + i\chi(x))/\sqrt{2} \end{pmatrix}, \tag{68}$$

where the components ϕ^+, H and χ now have zero vacuum expectation values.

The real component $H(x)$ describes a physical neutral scalar particle with mass

$$M_H = \mu\sqrt{2}, \tag{69}$$

i.e. the Higgs boson, which has so far escaped experimental detection at present colliders. This non-observation allows one to set a lower bound of $M_H > 114.3$ GeV [46].

At the European Laboratory for Particle Physics (CERN) in Geneva [6], a new particle accelerator, the Large Hadron Collider (LHC) is presently being constructed. In the year 2007 beams of protons are expected to collide at a center of mass energy of 14 TeV. In parallel to the accelerator two general purpose detectors, ATLAS and CMS, are being constructed to investigate proton-proton collisions in the new energy domain and to study fundamental questions of particle physics. The ATLAS experiment will be capable of detecting the Higgs boson with a high significance ($> 5\sigma$) in the mass range from 100 GeV to 1 TeV.

Quarks	$q_L \equiv$	$\begin{pmatrix} u \\ d \end{pmatrix}_L$ *up* *down*	$\begin{pmatrix} c \\ s \end{pmatrix}_L$ *charm* *strange*	$\begin{pmatrix} t \\ b \end{pmatrix}_L$ *top* *bottom*
	$q_R \equiv$	$u_R,\ d_R$	$c_R,\ s_R$	$t_R,\ b_R$
Leptons	$l_L \equiv$	$\begin{pmatrix} \nu_e \\ e \end{pmatrix}_L$ *e−neutrino* *electron*	$\begin{pmatrix} \nu_\mu \\ \mu \end{pmatrix}_L$ *μ−neutrino* *muon*	$\begin{pmatrix} \nu_\tau \\ \tau \end{pmatrix}_L$ *τ−neutrino* *tau*
	$l_R \equiv$	e_R	μ_R	τ_R

Table 3: Fermions of the Standard Model.

The Higgs field components have cubic and quadric self couplings following from V, and couplings to the gauge fields via the kinetic term of Eq. (64). Yukawa couplings give mass to the charged fermions, although the values of these masses are not specified by the Standard Model.

The left-handed fermion fields of each quark and lepton family are grouped into $SU(2)$ doublets

$$\psi_j^L = \begin{pmatrix} \psi_{j+}^L \\ \psi_{j-}^L \end{pmatrix}, \tag{70}$$

where j is the doublet index and $+/-$ refers to the component index ($\sigma = \pm$). The right-handed fields form singlets:

$$\psi_j^R = \psi_{j\sigma}^R \tag{71}$$

The left handed-fermion doublets and right handed-fermion singlets, included into our calculations, are listed in the Table 3.

Each left and right-handed multiplet is an eigenstate of the weak hypercharge Y according to Eq. (62). The covariant derivative (see Eq. (65))

$$D_\mu = \partial_\mu - ig_2 T_a W_\mu^a + ig_1 \frac{Y}{2} B_\mu \tag{72}$$

induces the fermion-gauge field interaction.

The interaction with the Higgs field is expressed in the terms of Yukawa couplings:

$$L_{fermion} = \sum_{j,\sigma} \left\{ \psi_j^L i\gamma^\mu D_\mu \psi_j^L + \psi_{j,\sigma}^R i\gamma^\mu D_\mu \psi_{j,\sigma}^R \right\} + L_{Yukawa} \ , \tag{73}$$

with

$$L_{Yukawa} = -g_l(\overline{\nu}_L \phi^+ l_R + \overline{l}_R \phi^- \nu_L + \overline{l}_L \phi^0 l_R + \overline{l}_R \phi^{0*} l_L). \tag{74}$$

Here, ϕ^- denotes the adjoint of ϕ^+. The Yukawa coupling g_l constants are directly related to the masses of the charged fermions as will be specified later. For one family of the leptons and quarks only (let's say u and d) and neglecting quark mixing, Eq. (74) can be written as:

$$\begin{aligned} L_{Yukawa} \ = \ & -g_d(\overline{u}_L \phi^+ d_R + \overline{d}_R \phi^- u_L + \overline{d}_L \phi^0 d_R + \overline{d}_R \phi^{0*} d_L) \\ & -g_u(\overline{u}_R \phi^+ d_L + \overline{d}_L \phi^- u_R + \overline{u}_R \phi^0 u_L + \overline{u}_L \phi^{0*} u_R) \end{aligned} \tag{75}$$

According to the expressions above, the Standard Model has included parameters

$$\mu^2, \ \lambda, \ g_1, \ g_2, \ g_{j\sigma} \tag{76}$$

i.e. two parameters coming from the Higgs self-interaction Eq. (66) μ^2 and λ (which are positive but otherwise arbitrary), gauge couplings g_1 and g_2, and Yukawa coupling

constants $g_{j\sigma}$. None of them is physical and can be measured directly, so we have to find a way to replace the original set Eq. (76) by the set of some physical, measurable quantities.

The symmetry is manifested in terms of fields W^a_μ, B_μ. The gauge invariant Higgs gauge field interaction in the kinetic part of Eq. (64) leads to mass terms for the vector bosons in the non-diagonal form

$$\left(\frac{g_2}{4}\upsilon\right)^2 (W_1^2 + W_2^2) + \frac{\upsilon^2}{8}(W^3_\mu, B_\mu) \begin{pmatrix} g_2^2 & -g_1 g_2 \\ -g_1 g_2 & g_2^2 \end{pmatrix} \begin{pmatrix} W^3_\mu \\ B_\mu \end{pmatrix}. \tag{77}$$

Let us now transform W^a_μ, B_μ to the physical fields $W^\pm_\mu$ and Z_μ, A_μ :

$$W^\pm_\mu = \frac{1}{\sqrt{2}}(W^1_\mu \mp i W^2_\mu) \tag{78}$$

$$\begin{aligned} Z_\mu &= \cos\theta_W W^3_\mu - \sin\theta_W B_\mu \\ A_\mu &= \sin\theta_W W^3_\mu + \cos\theta_W B_\mu \end{aligned} \tag{79}$$

where θ_W is called the Weinberg or weak mixing angle (although Glashow was the first to introduce the idea).

In Eq. (79), A_μ is the regular electric (photon) field which is massless and couples to the electron via the electric charge $e = \sqrt{4\pi\alpha}$, $W^\pm_\mu$ and Z_μ describe two charged $W^\pm$ and one neutral Z heavy vector bosons. The $SU(2)_L \times U(1)_Y$ proposal made by Glashow in 1961 was extended to accommodate massive vector bosons by Weinberg (1967) and Salam (1968). In 1979 Glashow, Weinberg and Salam were awarded the

Nobel prize for this work. The $W^{\pm}$ and Z were experimentally discovered in 1983 by a collaboration represented C. Rubbia and S. van der Meer as the spokesmen, who, correspondingly, received their Nobel prize in 1984.

In these fields the mass term Eq. (77) is diagonal and has the form

$$\frac{1}{2}M_W^2 W_\mu^+ W^{\mu-} + \frac{1}{4}(A_\mu, Z_\mu)\begin{pmatrix} 0 & 0 \\ 0 & M_Z^2 \end{pmatrix}\begin{pmatrix} A^\mu \\ Z^\mu \end{pmatrix}, \tag{80}$$

with

$$\begin{aligned} M_W &= \frac{1}{2}g_2 v, \\ M_Z &= \frac{1}{2}v\sqrt{g_1^2+g_2^2}, \end{aligned} \tag{81}$$

if the mixing angle in Eq. (79) is chosen as

$$\cos\theta_W = \frac{M_W}{M_Z} = \frac{g_2}{\sqrt{g_1^2+g_2^2}}. \tag{82}$$

The electric charge e can be expressed in terms of the gauge couplings in the following way:

$$e = \frac{g_1 g_2}{\sqrt{g_1^2+g_2^2}}, \tag{83}$$

or

$$g_1 = \frac{e}{\cos\theta_W}, \quad g_2 = \frac{e}{\sin\theta_W}. \tag{84}$$

The fermion masses can be obtained from the Yukawa coupling terms Eq. (75) as

$$m_{j\sigma} = g_{j\sigma}\frac{v}{\sqrt{2}}. \tag{85}$$

Thus, instead of the original set of non-physical parameters Eq. (76), we have an equivalent set where every parameter can be measured directly:

$$m_{j\sigma},\ M_W,\ M_Z,\ M_H,\ e \tag{86}$$

Not all of them are precisely known at the moment, which makes it crucial to analyze carefully dependence of the results of the work presented here from several purely-constrained Standard Model parameters and have the associated uncertainties under control. The values used in this work are summarized in Table 5.

2.1.2 Cabibbo-Kobayashi-Maskawa matrix

The quark mass eigenstates are not the same as the weak eigenstates, and the matrix relating these bases is called the Cabibbo-Kobayashi-Maskawa (CKM) matrix, or the quark mixing matrix $\mathbb{V}$. Its matrix elements are not predicted by the Standard Model and must be extracted from experiment.

For three quark generations, the matrix is expressed by convention in terms of a 3×3 unitary matrix $\mathbb{V}$ operating on the lower ($\sigma-$) quark mass eigenstates (d, s, and b):

$$\begin{pmatrix} d' \\ s' \\ b' \end{pmatrix} = \begin{pmatrix} V_{ud} & V_{us} & V_{ub} \\ V_{cd} & V_{cs} & V_{cb} \\ V_{td} & V_{ts} & V_{tb} \end{pmatrix} \begin{pmatrix} d \\ s \\ b \end{pmatrix}, \tag{87}$$

with experimental magnitudes [46]

$$\mathbb{V} = \begin{pmatrix} 0.9741 \text{ to } 0.9756 & 0.219 \text{ to } 0.226 & 0.0025 \text{ to } 0.0048 \\ 0.219 \text{ to } 0.226 & 0.9732 \text{ to } 0.9748 & 0.038 \text{ to } 0.044 \\ 0.004 & 0.037 \text{ to } 0.044 & 0.9990 \text{ to } 0.9993 \end{pmatrix} \tag{88}$$

For some matrix elements the values can be obtained from the weak decays of the relevant quarks or from deep inelastic neutrino scattering; the rest are restricted using unitarity constraints. See [46] for more experimental details.

There are several parametrizations of the CKM matrix. We use a parametrization involving the four angles θ_1, θ_2, θ_3, and δ, originally chosen by Kobayashi and Maskawa [16]:

$$\begin{pmatrix} d' \\ s' \\ b' \end{pmatrix} = \begin{pmatrix} c_1 & -s_1c_3 & -s_1s_3 \\ s_1c_2 & c_1c_2c_3 - s_2s_3e^{i\delta} & c_1c_2s_3 + s_2c_3e^{i\delta} \\ s_1s_2 & c_1s_2c_3 + c_2s_3e^{i\delta} & c_1s_2s_3 - c_2c_3e^{i\delta} \end{pmatrix} \begin{pmatrix} d \\ s \\ b \end{pmatrix}, \tag{89}$$

where $c_i = \cos\theta_i$ and $s_i = \sin\theta_i$ for $i = 1, 2, 3$.

2.1.3 Electroweak Feynman Rules

The Feynman rules is a method widely used today to calculate rates for electromagnetic and weak interaction particle processes. Each possible reaction is represented by a diagram; and each diagram has a definite amplitude related to it by a set of rules (the Feynman rules), providing a convenient shorthand for the calculations. There is a multiplication factor of for each vertex, i.e. coupling, so the amplitudes for diagrams

with many loops are small and can be neglected in most cases. Of course, Feynman rules are only useful when this factor is small, that is, for electromagnetic or weak interactions but not for strong interactions (except at very high energies).

The full set of electroweak Feynman rules can found in [12]. Below are shown several rules most commonly applied in the presented work, expressed in terms of bare parameters.

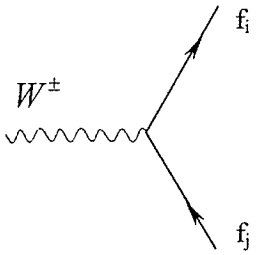

$$-i\frac{g_2}{2\sqrt{2}}V_{ij}\gamma_\mu(1-\gamma^5)$$

Fermion W-boson vertex.

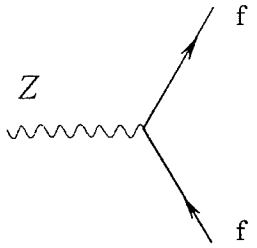

$$-i\frac{g_2}{2\cos\theta_W}\gamma_\mu(g_V^f-g_A^f\gamma^5)$$

Fermion Z-boson vertex.

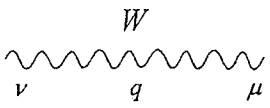

$$\frac{i}{q^2-M_W^2}\left[-g_{\mu\nu}+\frac{q_\mu q_\nu(1-\xi_+)}{q^2-\xi_+M_W^2}\right]$$

W-boson propagator

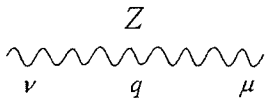

$$\boxed{\frac{i}{q^2 - M_Z^2}\left[-g_{\mu\nu} + \frac{q_\mu q_\nu (1-\xi_Z)}{q^2 - \xi_Z M_Z^2}\right]}$$

Z-boson propagator.

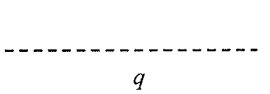

$$\boxed{\frac{i}{q^2 - \xi_+ M_W^2}}$$

Unphysical charged Higgs propagator.

We use notation ξ for the gauge-fixing parameter. As one can see from the expressions above, all boson propagators are gauge dependent. We shall consider different gauge choices in the next section, "Renormalization Theory" (Sec. 2.1.4).

The vector and axial-vector "charges" of the fermions, g_V^f and g_A^f, are defined as

$$\begin{aligned} g_V^f &= T_{w3}^f - 2Q_f \sin^2\theta_W, \\ g_A^f &= T_{w3}^f, \end{aligned} \tag{90}$$

The same quantities are also called "coupling constants".

More specifically, for the electron and the (u, d, s) quarks we have:

$$\begin{aligned} g_V^e &= -\frac{1}{2} + 2\sin^2\theta_W, \qquad g_A^e = -\frac{1}{2}, \\ g_V^u &= +\frac{1}{2} - \frac{4}{3}\sin^2\theta_W, \qquad g_A^u = +\frac{1}{2}, \\ g_V^{d,s} &= -\frac{1}{2} + \frac{2}{3}\sin^2\theta_W, \qquad g_A^{d,s} = -\frac{1}{2}. \end{aligned} \tag{91}$$

Expressions (90) and (91) differ from (16) and (17) by a factor of two, but give the same results in the end.

In this thesis, it was found more convenient to define amplitudes using chirality projection operators $\varpi_+ = \frac{1+\gamma_5}{2}$ and $\varpi_- = \frac{1-\gamma_5}{2}$ instead of explicit Dirac matrices γ_5. As an example, let us consider electron interacting with up-quark via $Z-$boson exchange, at tree level:

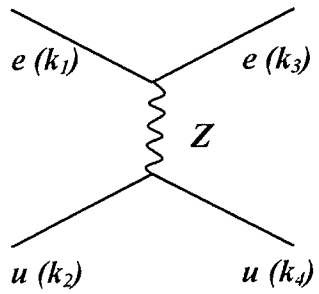

According to the Feynman rules stated above and for the momenta specified on the diagram, we obtain the following parity-violating amplitude:

$$\begin{aligned}\mathcal{M}^{Z-tree} &= \overline{u}(k_3, m_e)\left[\frac{ie(-\frac{1}{2}+\sin^2\theta_W)\gamma_\mu\,\varpi_-}{\cos\theta_W \sin\theta_W} + \frac{ie\sin\theta_W\,\gamma_\mu\,\varpi_+}{\cos\theta_W}\right] u(k_1, m_e) \\ &\times\overline{u}(k_4, m_u)\left[\frac{ie(\frac{1}{2}-\frac{2}{3}\sin^2\theta_W)\gamma_\nu\,\varpi_-}{\cos\theta_W \sin\theta_W} - \frac{2ie\sin\theta_W\,\gamma_\nu\,\varpi_+}{3\cos\theta_W}\right] u(k_2, m_u) \\ &\times\frac{g_{\mu\nu}}{(k_4-k_2)^2 - M_Z^2} \qquad (92)\end{aligned}$$

Let us now consider ZZ-box diagram as a simple example of a one-loop process:

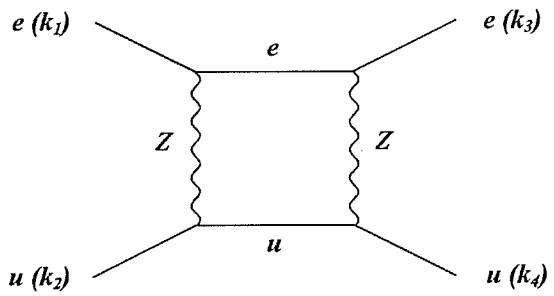

This amplitude will include four propagators (last line) and require integration over 4-dimensional momenta in the loop:

$$\begin{aligned}
\mathcal{M}^{\{Z-Z\}box} &= \frac{i}{16\pi^4}\int d^4q\,\overline{u}(k_3,m_e)\left[\frac{ie(-\frac{1}{2}+\sin^2\theta_W)\gamma_\mu\,\varpi_-}{\cos\theta_W\sin\theta_W}+\frac{ie\sin\theta_W\,\gamma_\mu\,\varpi_+}{\cos\theta_W}\right] \\
&\quad\times(m_e+(\not{k}_3+\not{k}_4-\not{k}_2-\not{q})) \\
&\quad\times\left[\frac{ie(-\frac{1}{2}+\sin^2\theta_W)\gamma_\nu\,\varpi_-}{\cos\theta_W\sin\theta_W}+\frac{ie\sin\theta_W\,\gamma_\nu\,\varpi_+}{\cos\theta_W}\right]u(k_1,m_e) \\
&\quad\times\overline{u}(k_4,m_u)\left[\frac{ie(\frac{1}{2}-\frac{2}{3}\sin^2\theta_W)\gamma_\sigma\,\varpi_-}{\cos\theta_W\sin\theta_W}-\frac{2ie\sin\theta_W\,\gamma_\sigma\,\varpi_+}{3\cos\theta_W}\right](m_u+(\not{k}_2+\not{q})) \\
&\quad\times\left[\frac{ie(\frac{1}{2}-\frac{2}{3}\sin^2\theta_W)\gamma_\rho\,\varpi_-}{\cos\theta_W\sin\theta_W}-\frac{2ie\sin\theta_W\,\gamma_\rho\,\varpi_+}{3\cos\theta_W}\right]u(k_2,m_u) \\
&\quad\times\frac{1}{q^2-M_Z^2}\cdot\frac{1}{(k_2+q)^2-m_u^2}\cdot\frac{1}{(k_2+q-k_4)^2-M_Z^2}\cdot\frac{g_{\nu\rho}g_{\mu\sigma}}{(k_2+q-k_4-k_3)^2-m_e^2}
\end{aligned} \tag{93}$$

Generally speaking, the task of constructing an amplitude according to the Feynman rules is a very straightforward one. This part can be automated. The amplitude chosen above as a simple example is not divergent. However, sometimes the amplitudes beyond tree level do diverge, and integration requires more of an effort. We can tell whether the integral diverges by simply counting the powers of q in a given

Feynman graph. Each fermion propagator contributes q^{-1}, each boson propagator contributes q^{-2}, each loop contributes a loop integration with q^4, and each vertex with n derivatives contributes at most n powers to q. If the result scales as q^m and $m \geq 0$, the graph diverges. The methods of regularization and renormalization applicable in this case are discussed in the next section.

2.1.4 Renormalization Theory

One of the creators of quantum field theory, Dirac himself, considered the renormalization approach to be artificial and contrived. In his opinion, the renormalization approach "... is just not sensible mathematics. Sensible mathematics involves neglecting a quantity when it turns out to be small - not neglecting it because it is infinitely great and you do not want it!" By introducing supersymmetry, two new types of finite theories were developed recently: Super Yang-Mills theory and Superstings (see [35] for more extensive review). Superstring theory is the most powerful and remarkable of the two. It is finite to all orders of perturbation theory, plus it contains quantum gravity. However, there is no experimental evidence at all to support supersymmetry. So, for now, we must rely on infinite, but renormalizable theories, such as Yukawa theory and spontaneously broken non-Abelian gauge theory. Not all theories are renormalizable. Renormalizability of Yang-Mills theory, proven by 't Hooft, made it possible to successfully apply quantum field theory to the weak

interactions in order to calculate effects beyond the tree level.

Divergences found in quantum field theory came from the transition to an infinite number of degrees of freedom from a finite number found in quantum mechanics. We have to sum continually over an infinite number of internal modes in loop integration, which leads to divergences.

There are numerous renormalization proposals with the details varying from scheme to scheme, but they all share the same basic physical features. The divergences are absorbed into a set of "bare" physical parameters such as the coupling constants and particle masses. Those parameters are, consequently, divergent and unmeasurable. The divergences of these parameters are chosen in a way so that they cancel against the ultraviolet infinities coming from infinite classes of Feynman diagrams. After the divergences are absorbed by the bare parameters, parameters become renormalized and "dressed", i.e. physical and measurable. The details of the renormalization program may be tedious and quite complicated. Here, the schematic point of view is presented. For a more comprehensive description, the readers are directed to [35], [48], [23], [2].

There are three essential steps in renormalization theory. First, power counting is done as described in the previous section.

Second, we have to perform regularization. Because manipulating divergent integrals is not well defined, we need to cut off the integration over d^4q. This formally

makes each graph finite. After we have rearranged the graphs to put all divergent terms into the physical parameters, making them "dressed", we let the cutoff go to infinity. A wide variety of regularization schemes have been developed over the decades, each with its own advantages and disadvantages. Let us consider three main types: Pauli-Villars, Lattice and Dimensional regularizations.

In the Pauli-Villars regularization scheme, we cut off the integrals by assuming the existence of a fictitious particle of mass M. The propagator becomes modified by a factor

$$\frac{1}{q^2 - m^2} - \frac{1}{q^2 - M^2} = \frac{m^2 - M^2}{(q^2 - m^2)(q^2 - M^2)},$$

where the relative minus sign means that the new particle is a "ghost", i.e. the particle has negative norm. The propagator now behaves as $1/q^4$, rendering all graphs finite. Then, we let M^2 go to infinity so that the unphysical fermion decouples from the theory. The Pauli-Villars scheme preserves local gauge invariance and Ward identities in QED, but they get broken for higher groups [35].

Lattice regularization is the most widely used regularization scheme in QCD for non-perturbative calculations. Combined with Monte-Carlo techniques, it makes it possible to extract qualitative and even some quantitative information from QCD. Here, we assume that space-time is actually a set of discrete points arranged in some kind of hypercubical array. The lattice spacing then serves as the cutoff for the space-time integral. Because this method is defined in Euclidean space, this approach allows

us to calculate only the static properties of QCD.

Dimensional regularization is the method selected for the presented work. We describe it more extensively later, in Chapter 3, "Details of Calculations". The method involves generalizing the action to arbitrary dimension d, where there are regions in complex d space in which the Feynman integrals are all finite. Then, as we analytically continue d to four, the Feynman graphs pick up poles in d space, allowing us to absorb the divergences of the theory into the physical parameters. Dimensional regularization preserves all properties of the theory that are independent of the dimension of space-time, such as the Ward Takahashi identities (see Sec. 2.1.5).

As the third step in renormalization theory, we actually renormalize the theory using either multiplicative renormalization or counterterms. The method of multiplicative renormalization, developed first for QED, involves summation over an infinite series of Feynman graphs followed by the redefinition of the coupling constants and masses, allowing us to absorb the divergent sum. Since the bare parameters are unmeasurable, we can assume they are divergent and that they cancel against the divergences of corresponding Feynman graphs. In the method of counterterms, which we actually use in this work, we add new terms directly to the action to subtract off the divergent graphs. Adding the original action with the counterterm gives us the renormalization of masses and coupling constants in the action. The coefficients of these counterterms are chosen so that they precisely cancel the divergent graphs.

Counterterms are proportional to terms in the original action and there are a finite number of counterterms needed to make the theory finite to any order.

2.1.5 Ward Takahashi Identities

A set of Ward Takahashi identities ([55]) simplifies our work by reducing the number of independent renormalization constants.

For correlation functions in QED, and amplitudes of the type

$\mathcal{M}(k; p_1 \cdots p_n; q_1 \cdots q_n) =$

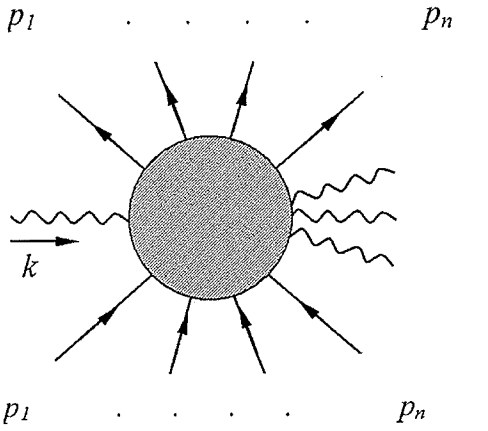

,

the Ward Takahashi identity is given by

$$k_\mu \mathcal{M}^\mu(k; p_1 \cdots p_n;\ q_1 \cdots q_n) \tag{94}$$

$$= e \sum_i [\mathcal{M}_0(p_1 \cdots p_n;\ q_1 \cdots (q_i - k) \cdot \cdot\cdot) - \mathcal{M}_0(p_1 \cdots (p_i + k) \cdots;\ q_1 \cdots q_n)] \ .$$

For the arbitrary symmetry

$$\varphi_a(x) \rightarrow \varphi_a(x) + \varepsilon \Delta\varphi_a(x)$$

we can use the Schwinger-Dyson equation as the Ward Takahashi identity:

$$\begin{aligned} & \langle \partial_\mu j^\mu(x)\varphi_a(x_1)\varphi_b(x_2)\rangle \qquad (95) \\ = \; & -i\left\langle (\Delta\varphi_a(x_1)\delta(x-x_1))\varphi_b(x_2) + \varphi_a(x_1)(\Delta\varphi_b(x_2)\delta(x-x_2))\right\rangle \ . \end{aligned}$$

Now, how does the expression like Eq. (94) help us to reduce the number of independent renormalization constants? Let us consider the simplest example of the electron-photon vertex, where on the left hand side of Eq. (94) we would have the three-point function with one entering (p) and one exiting ($p+k$) electron and one external photon (k). Then the Ward Takahashi identity reads ([48]):

$$S(p+k)[-iek_\mu\Gamma^\mu(p+k,p)]S(p) = e(S(p) - S(p+k)), \qquad (96)$$

where quantities S are the electron propagators and Γ^μ is the vertex.

Multiplying both sides by $S^{-1}(p)$ and $S^{-1}(p+k)$ gives:

$$-ik_\mu\Gamma^\mu(p+k,p) = S^{-1}(p+k) - S^{-1}(p). \qquad (97)$$

Let us now define the renormalization factors Z_1 and Z_2 as

$$\Gamma^\mu(p+k,p) \to Z_1^{-1}\gamma^\mu$$

for $k \to 0$, and

$$S(p) \sim \frac{iZ_2}{\not{p} - m}.$$

Setting p near the mass shell and expanding Eq. (96) about $k = 0$, for the first-order terms we obtain:

$$-iZ_1^{-1} \not{k} = -iZ_2^{-1} \not{k},$$

i.e.

$$Z_1 = Z_2. \tag{98}$$

2.2 One-Quark Radiative Corrections

As was indicated in the previous chapter, extracting form factors $G_{E,M}^Z$ and G_A^Z is based not only on experimental data, but also on theoretical calculations of radiative corrections for parity-violating scattering. We calculate the radiative corrections to tree level for the electroweak interaction in the scattering processes $e + p \rightarrow e + p$ and $e + n \rightarrow e + n$ by modeling the nucleon as a collection of quasi-free quarks each carrying some fraction x of the nucleon four-momentum.

If we assume that during the scattering process the electron interacts with only one quark, we can split the problem of electron-nucleon scattering into calculations of Feynman graphs for processes like $e(p_1) + q(p_2) \rightarrow e(p_3) + q(p_4)$, with q representing (u, d, s) quarks. Starting from the fundamental coupling of an elementary fermion to the photon or to the Z^0, one can arrive at the general form of electromagnetic and weak invariant amplitudes [45]:

$$\mathcal{M}^\gamma = -\frac{4\pi\alpha}{q^2} Q_f l^\mu J_\mu^\gamma, \tag{99}$$

$$\mathcal{M}^Z = -\frac{4\pi\alpha}{M_Z^2 - q^2}\frac{1}{(4\sin\theta_W\cos\theta_W)^2}\left(g_V^f l^\mu + g_A^f l^{\mu 5}\right)\left(J_\mu^Z + J_{\mu 5}^Z\right), \qquad (100)$$

where l^μ ($l^{\mu 5}$) and J^μ ($J^{\mu 5}$) are leptonic and hadronic vector (axial vector) currents, respectively, and Q_f is the electromagnetic charge number of the fermion. Definitions for currents and couplings are given in Chapter 1, Part 2.

The weak coupling has been expressed in terms of the parameter set (α, M_W, M_Z) rather than G_F, noting that $\sin^2\theta_W = 1 - M_W^2/M_Z^2$ in our renormalization scheme. In order to be parity-violating, Z^0 exchange must involve either $V(e) \times A(q)$ or $A(e) \times V(q)$, where $V(A)$ stands for a vector (axial vector) current. Thus, it is convenient to express the amplitude for the parity-violating (PV) part of the electron-quark $(e-q)$ scattering in the general form

$$\begin{aligned}\mathcal{M}_{\rm PV}^{eq} &= A^{eq}\,\bar{u}_e(p_3)\gamma^\mu u_e(p_1)\cdot\bar{u}_q(p_4)\gamma_\mu\gamma_5 u_q(p_2) \\ &\quad + B^{eq}\,\bar{u}_e(p_3)\gamma^\mu\gamma_5 u_e(p_1)\cdot\bar{u}_q(p_4)\gamma_\mu u_q(p_2), \qquad (101) \\ &\equiv A^{eq}\,J_{VA}^{eq} + B^{eq}\,J_{AV}^{eq}.\end{aligned}$$

Here, A^{eq} and B^{eq} are functions of the Standard Model parameters, $n-$point tensor coefficients, and kinematics. From this point we define one-loop radiative correction relative to tree level electron-quark scattering as follows:

$$R_A^q \equiv \frac{A_{\rm rad}^{eq}}{A_{\rm tree}^{eq}}, \qquad R_V^q \equiv \frac{B_{\rm rad}^{eq}}{B_{\rm tree}^{eq}}, \qquad (102)$$

where $A_{\rm tree}^{eq}$ and $B_{\rm tree}^{eq}$ come from the tree level, and $A_{\rm rad}^{eq}$ and $B_{\rm rad}^{eq}$ come from the one-loop radiative corrections. The relationship between the hadronic radiative cor-

rections of Eqs. (41-43) and the electron-quark radiative corrections of Eq. (102) follows from the linear combinations:

$$\begin{aligned} R_V^{T=0} &= (g_V^u R_V^u + g_V^d R_V^d)/(g_V^u + g_V^d), \\ R_V^{T=1} &= (g_V^u R_V^u - g_V^d R_V^d)/(g_V^u - g_V^d), \\ R_V^{(0)} &= (g_V^u R_V^u + g_V^d R_V^d + g_V^s R_V^s)/(g_V^u + g_V^d + g_V^s), \\ R_A^{T=0} &= -R_A^u + R_A^d, \\ R_A^{T=1} &= (R_A^u + R_A^d)/2, \\ R_A^{(0)} &= -R_A^u + R_A^d + R_A^s. \end{aligned} \tag{103}$$

For the axial corrections we have used the explicit values of g_A^q, which are $+1$ or -1, and the $R_A^{T=0}$ correction is divided by 1 instead of the tree level term $g_A^u + g_A^d$, since $g_A^u + g_A^d = 0$.

Each particle carries 4-momentum $p_i^2 = m_i^2$ with the following structure in the center-of-mass (CM) frame:

$$\begin{aligned} p_1 &= (E_1, 0, 0, p)\,, \\ p_2 &= (E_2, 0, 0, -p)\,, \\ p_3 &= (E_3, p\sin\theta, 0, p\cos\theta)\,, \\ p_4 &= (E_4, -p\sin\theta, 0, -p\cos\theta)\,. \end{aligned} \tag{104}$$

Here $E_1 = E_3$ and $E_2 = E_4$ (for elastic scattering) and p denote the energy and mo-

mentum of the scattered particles. The Mandelstam variables are defined as follows:

$$\begin{aligned} s &= (p_1 + p_2)^2 = (E_1 + E_2)^2 = E_{\rm CM}^2, \\ t &= (p_1 - p_3)^2 = -2p^2\,(1 - \cos\theta)\,, \\ u &= (p_1 - p_4)^2 = (E_1 - E_2) - 2p^2\,(1 + \cos\theta)\,, \end{aligned} \tag{105}$$

with $E_{1,2}^2 = p^2 + m_{1,2}^2$. For elastic scattering we have $s + t + u = 2m_1 + 2m_2$. Input kinematic parameters, in our case, are the energy of the electron in the laboratory reference frame, $E_{\rm lab}$, and the scattering angle θ. Hence $E_{\rm CM}$ and p can be expressed in terms of $E_{\rm lab}$ and θ:

$$p^2 = \frac{\left(E_{\rm CM}^2 + m_2^2 - m_1^2\right)^2}{2E_{\rm CM}^2} - m_2^2. \tag{106}$$

For quarks bound in the nucleon, we can assume that the energy of the quark can be defined as a fraction of the mass of the nucleon $E_{2,\rm lab}^2 = x^2 m_N^2$, with $x \approx 1/3$. Taking into account $E_{2,\rm lab}^2 = p_{2,\rm lab}^2 + m_2^2$, we can determine the center-of-mass energy as follows:

$$\begin{aligned} E_{\rm CM}^2 &= (p_{1,\rm lab} + p_{2,\rm lab})^2 = m_1^2 + m_2^2 + \\ &\quad + 2E_{1,\rm lab}\, x\, m_N \left(1 - \frac{(E_{1,\rm lab}^2 - m_1^2)^{1/2}((x\,m_N)^2 - m_2^2)^{1/2}\cos\theta_i}{E_{1,\rm lab}\, x\, m_N}\right). \end{aligned} \tag{107}$$

In the latter equation, θ_i denotes the unknown angle between the spatial momentum of the electron and quark just before scattering took place. Final expressions for radiative corrections have been integrated over this angle to account for all possible values of θ_i.

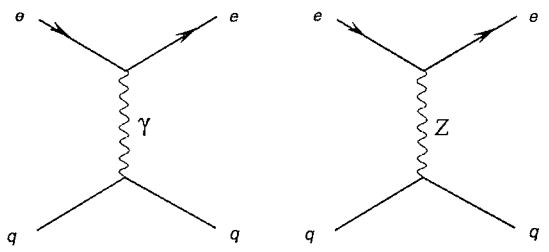

Figure 10: PC and PNC tree-level amplitudes for electron-quark scattering.

3 Details of the Calculations

3.1 Tree Level PNC Amplitude

At tree level, we have only one type of diagram to consider:

The PC part is of no interest, and PNC amplitude of Fig. 10 has the simple structure

$$
\begin{aligned}
F_{PN_0}^{e,f} \;=\; & \frac{\pi\alpha\left(1-4\sin\left(\theta_W\right)^2\right)}{4\cos\left(\theta_W\right)^2\sin\left(\theta_W\right)^2\left(t-M_Z^2\right)}\times \\
& \overline{u}\left(k_3,m_e\right)\gamma_\mu u\left(k_1,m_e\right)\cdot\overline{u}\left(k_4,m_f\right)\gamma_\mu\gamma_5 u\left(k_2,m_f\right)+ \\
& +\frac{\pi\alpha\left(3-8\sin\left(\theta_W\right)^2\right)}{12\cos\left(\theta_W\right)^2\sin\left(\theta_W\right)^2\left(t-M_Z^2\right)}\times \\
& \overline{u}\left(k_4,m_f\right)\gamma_\mu u\left(k_2,m_f\right)\cdot\overline{u}\left(k_3,m_e\right)\gamma_\mu\gamma_5 u\left(k_1,m_e\right).
\end{aligned}
\tag{108}
$$

Here $\sin\theta_W^2 = 1 - \frac{M_W^2}{M_Z^2}$ is the Weinberg mixing angle.

3.2 One-loop corrections

Doing one-loop calculations in the Standard Model by hand is a laborious task due to the sheer number of particles and the complexity of the underlying theory. To facilitate this task, and to reduce the possibility of errors, for some time software packages have been developed to automate different tasks in these calculations [22]. In this paper, we have chosen to use the packages *FeynArts*, *FormCalc*, and *LoopTools*, running on *Mathematica* platform [21]. These packages are designed to work hand in hand on various aspects of the calculation, as described below.

In total, 446 one-loop diagrams were calculated, including counterterms and contributions from scalar bosons (H, χ, ϕ) and ghost fields (u_Z, u_-, u_+). All diagrams are listed in the Appendix. For analysis and comparison with earlier work (see Ref. [42], for example), it is useful to split diagrams into three classes (Fig. 11). Class 1 are self-energy loops, Class 2 are triangles, and Class 3 are boxes. Class 1 have a dominant contribution from Z exchange and γZ mixing. Class 2 include triangles with $ff'Z$ and $ff'\gamma$ vertices. Class 3 are the ZZ, WW and γZ box and crossed box diagrams. Contributions from scalar bosons and ghost fields to the boxes were found to be negligibly small.

Because of the huge size of the analytical expressions for amplitudes, we leave them

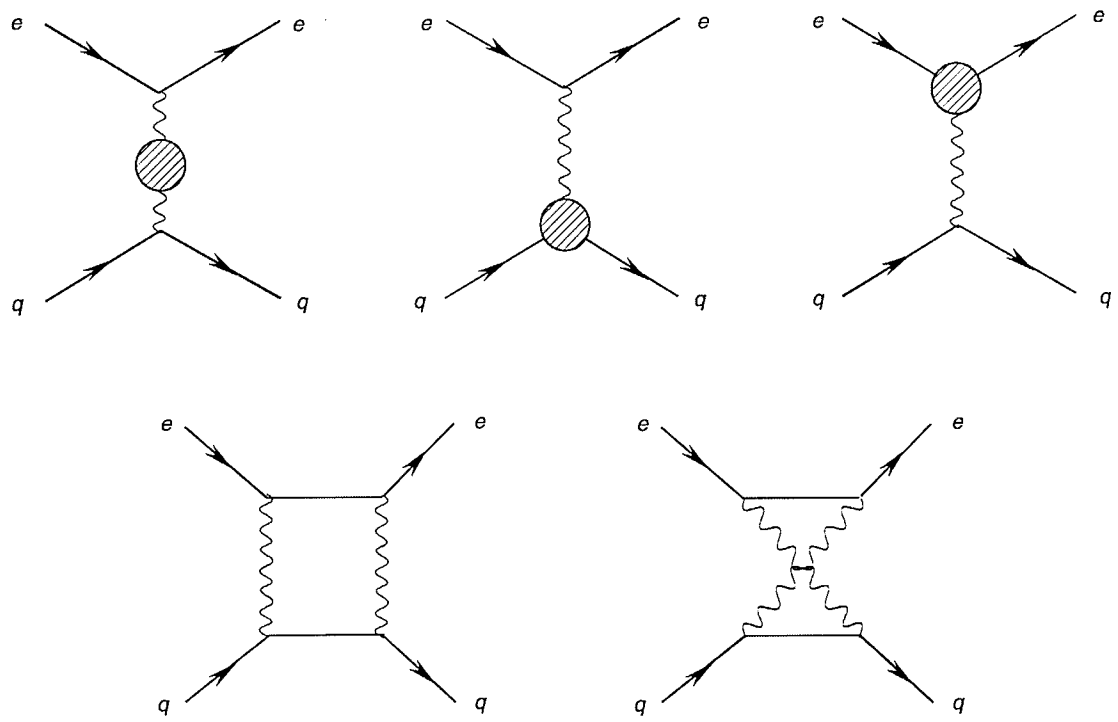

Figure 11: Classes of one-loop contributions to electron-quark scattering including self-energy, vertex, and box diagrams.

out of this work. We keep the complete expressions in electronic form and can send them to anyone interested. Certain steps involved in the evaluation of the one-loop PNC amplitude have to be explained more carefully. To evaluate four dimensional one-loop tensor integrals, we have used the Constrained Differential Renormalization (CDR) scheme [2] implemented in the package *FormCalc*. In the CDR scheme, Feynman diagrams are considered completely in four dimensions. Thereafter, the reduction of singular basic functions (products of propagators and their derivatives) has been renormalized into the sum of "regular" ones by implementing a set of rules in such a way that Ward identities are satisfied. It was proven in Ref. [21] that CDR is equivalent at the one-loop level to regularization by dimensional reduction [52], after taking the Fourier transform of the basic renormalized functions into momentum space. This last approach corresponds to a modified dimensional regularization, where one-loop integrals are considered in D dimensions, but all the tensors and spinors are kept 4-dimensional [52]. To preserve gauge invariance in dimensional reduction, one should use $\widehat{g}_{\mu\nu}$ $\left(\widehat{g}^{\mu}_{\mu} = D\right)$ with $g_{\mu\nu}\widehat{g}^{\nu\rho} = \widehat{g}^{\rho}_{\mu}$ for the tensor decomposition.

In dimensional regularization, the general structure of a one-loop tensor integral can be written in the form [24]

$$J^{N}_{i_1\ldots i_p} = \frac{(2\pi\mu)^{4-D}}{i\pi^2}\int d^D q \frac{q_{i_1}q_{i_2}\cdots q_{i_p}}{(q^2-m_1^2)\left((q+p_1)^2-m_2^2\right)\cdots\left((q+p_{N-1})^2-m_N^2\right)}. \quad (109)$$

Here, μ is the regularization scale parameter of dimensional reduction, which is related to the CDR renormalization scale by $\log\left(\bar{M}^2\right) = \log\left(\mu^2\right) + 2$. For the tensor

decomposition of Eq. (109) into linear combinations of tensor coefficients functions, we have used the method of Passarino-Veltman [47]. Using the Passarino-Veltman method for tensor decomposition, we can represent the above integral as the linear combination of tensor coefficients functions, which reads explicitly:

$$
\begin{aligned}
B'_{\mu} &= k_{1\mu} B_1, \\
B'_{\mu\nu} &= \widehat{g}_{\mu\nu} B_{00} + k_{1\mu} k_{1\nu} B_{11}, \\
C'_{\mu} &= \sum_{i=1}^{2} k_{i\mu} C_i, \\
C'_{\mu\nu} &= \widehat{g}_{\mu\nu} C_{00} + \sum_{i,j=1}^{2} k_{i\mu} k_{j\nu} C_{ij}, \\
C'_{\mu\nu\rho} &= \sum_{i=1}^{2} \left(\widehat{g}_{\mu\nu} k_{i\rho} + \widehat{g}_{\nu\rho} k_{i\mu} + \widehat{g}_{\mu\rho} k_{i\nu} \right) C_{00i} + \sum_{i,j,\xi=1}^{2} k_{i\mu} k_{j\nu} k_{\xi\rho} C_{ij\xi}, \\
D'_{\mu} &= \sum_{i=1}^{3} k_{i\mu} D_i, \\
D'_{\mu\nu} &= \widehat{g}_{\mu\nu} D_{00} + \sum_{i,j=1}^{3} k_{i\mu} k_{j\nu} D_{ij},
\end{aligned}
\tag{110}
$$

$$D'_{\mu\nu\rho} = \sum_{i=1}^{3} \left(\widehat{g}_{\mu\nu}k_{i\rho} + \widehat{g}_{\nu\rho}k_{i\mu} + \widehat{g}_{\mu\rho}k_{i\nu}\right) D_{00i} + \sum_{i,j,\xi=1}^{2} k_{i\mu}k_{j\nu}k_{\xi\rho}D_{ij\xi},$$

$$D'_{\mu\nu\rho\sigma} = \left(\widehat{g}_{\mu\nu}\widehat{g}_{\rho\sigma} + \widehat{g}_{\mu\rho}\widehat{g}_{\nu\sigma} + \widehat{g}_{\mu\sigma}\widehat{g}_{\nu\rho}\right) D_{0000}$$

$$+ \sum_{i,j=1}^{3} \begin{pmatrix} \widehat{g}_{\mu\nu}k_{i\rho}k_{j\sigma} + \widehat{g}_{\nu\rho}k_{i\mu}k_{j\sigma} + \widehat{g}_{\mu\rho}k_{i\nu}k_{j\sigma} \\ \\ +\widehat{g}_{\mu\sigma}k_{i\nu}k_{j\rho} + \widehat{g}_{\nu\sigma}k_{i\mu}k_{j\rho} + \widehat{g}_{\rho\sigma}k_{i\mu}k_{j\nu} \end{pmatrix} D_{00ij}$$

$$+ \sum_{i,j,\xi,m=1}^{3} k_{i\mu}k_{j\nu}k_{\xi\rho}k_{m\sigma}D_{ij\xi m}.$$

Here (B', C', D') mean two, three, and four point tensor integrals, with two, three, and four propagators, respectively. The rank of the above tensors is equal to the number of integrable momenta $\left(q_{i_1}q_{i_2}\ldots q_{i_p}\right)$in the numerator of Eq. (109). Two, three and four point tensor coefficient functions, coming from tensor decomposition, were calculated numerically by using the package *LoopTools*, and algebraic calculations were completed with the help of packages *FeynArts*, *FormCalc* and *FORM*. To summarize this section, we provide an outline of how calculations were implemented in these packages.

1. Generation of the diagrams (package *FeynArts*)

- Topologies are defined

- Fields are inserted
- Amplitudes and their counterterms in integral form are defined, along with CKM matrix

2. Evaluation of amplitudes (package *FormCalc* along with *FORM*)

- Indices contracted and traces are taken
- Amplitudes in general form (i.e. combination of many-point tensor coefficients along with spinor chains) are presented
- Radiative corrections were calculated (On Shell Renormalization)
- Infrared divergences are treated by adding soft-photon emission

3. Numerical evaluation

- Standard Model parameters and kinematics are defined
- Many-point tensor coefficients are numerically evaluated (package *LoopTools*)

3.3 Renormalization constants

Generally, tensor coefficient functions are ultraviolet divergent (inversely proportional to the parameter $\varepsilon = 4 - D$). In order to cancel divergences and transform bare parameters into physical observables one has to introduce a renormalization scheme. The

renormalized parameters are related to the bare parameters (denoted by a subscript 0) as follows:

$$
\begin{aligned}
M^2_{Z,0} &= M^2_Z + \delta M^2_Z, \\
M^2_{W,0} &= M^2_W + \delta M^2_W, \\
M^2_{H,0} &= M^2_H + \delta M^2_H, \\
m_{f_i,0} &= m_{f_i} + \delta m_{f_i}, \\
e_0 &= (1+\delta e)\, e, \\
\begin{pmatrix} Z_0 \\ A_0 \end{pmatrix} &= \begin{pmatrix} 1+\frac{1}{2}\delta Z^{ZZ} & \frac{1}{2}\delta Z^{ZA} \\ \frac{1}{2}\delta Z^{AZ} & 1+\frac{1}{2}\delta Z^{AA} \end{pmatrix} \begin{pmatrix} Z \\ A \end{pmatrix}, \\
W^{\pm}_0 &= \left(1+\frac{1}{2}\delta Z^{WW}\right) W^{\pm}, \\
H_0 &= \left(1+\frac{1}{2}\delta Z^{H}\right) H, \\
f^L_{i,0} &= \left(\delta_{ij}+\frac{1}{2}(\delta f^f_L)_{ij}\right) f^L_j, \\
f^R_{i,0} &= \left(\delta_{ij}+\frac{1}{2}(\delta f^f_R)_{ij}\right) f^R_j.
\end{aligned}
\tag{111}
$$

Counterterms were chosen in the On Shell Renormalization (OSR) scheme in the 't Hooft-Feynman gauge, where the gauge parameter $\xi = 1$ with the following renormalization constants ([23]):

Wave function renormalization:

$$\begin{aligned}
\delta Z^{ZZ} &= -\mathrm{Re}\left(\frac{\partial}{\partial k^2}\Sigma_{\perp}^{ZZ}\left(k^2\right)\right)_{k^2=M_Z^2}, \\
\delta Z^{ZA} &= 2\mathrm{Re}\left(\frac{\Sigma_{\perp}^{AZ}(0)}{M_Z^2}\right), \qquad (112)
\end{aligned}$$

$$\begin{aligned}
\delta Z^{AA} &= -\mathrm{Re}\left(\frac{\partial}{\partial k^2}\Sigma_{\perp}^{AA}\left(k^2\right)\right)_{k^2=0}, \\
\delta Z^{AZ} &= -2\mathrm{Re}\left(\frac{\Sigma_{\perp}^{AZ}\left(M_Z^2\right)}{M_Z^2}\right), \qquad (113)
\end{aligned}$$

$$\delta Z^{WW} = -\mathrm{Re}\left(\frac{\partial}{\partial k^2}\Sigma_{\perp}^{WW}\left(k^2\right)\right)_{k^2=M_W^2}, \qquad (114)$$

$$\delta Z^{H} = -\mathrm{Re}\left(\frac{\partial}{\partial k^2}\Sigma^{H}\left(k^2\right)\right)_{k^2=M_H^2}, \qquad (115)$$

$$\begin{aligned}
\delta Z^{\chi} &= -\mathrm{Re}\left(\frac{\partial}{\partial k^2}\Sigma^{\chi}\left(k^2\right)\right)_{k^2=M_Z^2}, \\
\delta Z^{\phi} &= -\mathrm{Re}\left(\frac{\partial}{\partial k^2}\Sigma^{\phi}\left(k^2\right)\right)_{k^2=M_W^2}, \qquad (116)
\end{aligned}$$

(117)

$$\begin{aligned}
(\delta f_L^f)_{ii} &= -\mathrm{Re}\left(\Sigma_{ii}^{f,L}\left(m_{f_i}^2\right)\right) \qquad (118) \\
&\quad -m_{f_i}^2\mathrm{Re}\left(\frac{\partial}{\partial p^2}\left[\Sigma_{ii}^{f,L}\left(p^2\right)+\Sigma_{ii}^{f,R}\left(p^2\right)+2\Sigma_{ii}^{f,S}\left(p^2\right)\right]\right)_{p^2=m_{f_i}^2},
\end{aligned}$$

$$\begin{aligned}
(\delta f_R^f)_{ii} &= -\mathrm{Re}\left(\Sigma_{ii}^{f,R}\left(m_{f_i}^2\right)\right) \\
&\quad -m_{f_i}^2\mathrm{Re}\left(\frac{\partial}{\partial p^2}\left[\Sigma_{ii}^{f,L}\left(p^2\right)+\Sigma_{ii}^{f,R}\left(p^2\right)+2\Sigma_{ii}^{f,S}\left(p^2\right)\right]\right)_{p^2=m_{f_i}^2}.
\end{aligned}$$

Mass renormalization:

$$\delta M_Z^2 = \mathrm{Re}\left(\Sigma_\perp^{ZZ}\left(M_Z^2\right)\right), \tag{119}$$

$$\delta M_W^2 = \mathrm{Re}\left(\Sigma_\perp^{WW}\left(M_W^2\right)\right), \tag{120}$$

$$\delta M_H^2 = \mathrm{Re}\left(\Sigma^{H}\left(M_H^2\right)\right),$$

$$\delta m_{f_i} = \frac{1}{2} m_{f_i} \mathrm{Re}\left(\Sigma_{ii}^{f,L}\left(m_{f_i}^2\right) + \Sigma_{ii}^{f,R}\left(m_{f_i}^2\right) + 2\Sigma_{ii}^{f,S}\left(m_{f_i}^2\right)\right). \tag{121}$$

Here L and R correspond to left- and right-handed fermions, Σ is the one-loop integral of the truncated self-energy graph, and $\perp$ denotes the transverse part only.

Charge and mixing angle renormalization:

$$\delta(\sin^2\theta_W) = \cos^2\theta_W \left(\frac{\delta M_Z^2}{M_Z^2} - \frac{\delta M_W^2}{M_W^2}\right), \tag{122}$$

$$\delta(\cos^2\theta_W) = -\delta(\sin^2\theta_W), \tag{123}$$

$$\delta e = -\frac{1}{2}\left(\delta Z^{AA} + \frac{\sin^2\theta_W}{\cos^2\theta_W}\,\delta Z^{ZA}\right), \tag{124}$$

with $\sin^2\theta_W = 1 - M_W^2/M_Z^2$.

3.4 Infrared divergences and soft-photon emission

For diagrams with photon exchange between external fermion legs we have encountered infrared (IR) divergences. These are regulated by introducing a small photon "rest mass" λ in loop integrals involving the photon propagator. This results in $\ln\left(m_f^2/\lambda^2\right)$ terms in the amplitude. Hence the radiative corrections are, strictly

speaking, infinite in the limit $\lambda \to 0$. This unphysical dependence on λ is cancelled by adding the inelastic bremsstrahlung contributions arising from soft-photon emission by the external fermions (i.e. from the initial or final electron or quark) to the scattering cross section [11].

To see how this works in the parity-violating asymmetry, consider the inelastic bremsstrahlung amplitude $\mathcal{M}_{\rm b}^{Z}$, which includes the four diagrams of Fig. 12 involving Z exchange, and the corresponding QED amplitude $\mathcal{M}_{\rm b}^{\gamma}$ (not shown) involving photon exchange. The total inelastic cross section is given by

$$d\sigma_{\rm b}^{eq} \sim \left| \mathcal{M}_{\rm b}^{\gamma} + \mathcal{M}_{\rm b}^{Z} \right|^2 . \tag{125}$$

In analogy with Eq. (37), a parity-violating asymmetry will result from the interference term $2\mathrm{Re}\left\{ (\mathcal{M}_{\rm b}^{\gamma})^* \, \mathcal{M}_{\rm b}^{Z} \right\}$.

In the soft photon approximation, it is straightforward to show (see Ref. [40], for example) that the amplitude for soft photon emission can be written in terms of the Born (tree level) amplitude

$$\mathcal{M}_{\rm b}^{\gamma} = \mathcal{M}_{\rm Born}^{\gamma} \left[-\frac{p_1}{(p_1 \cdot k)} + \frac{p_3}{(p_3 \cdot k)} + \frac{Q_q p_2}{(p_2 \cdot k)} - \frac{Q_q p_4}{(p_4 \cdot k)} \right] \cdot \epsilon^*(k), \tag{126}$$

with k the momentum of the photon and $\epsilon(k)$ its polarization. This is just the amplitude for elastic scattering (without bremsstrahlung) times a factor for soft photon emission. An identical factor relates $\mathcal{M}_{\rm b}^{Z}$ to $\mathcal{M}_{\rm Born}^{Z}$.

The contribution of the parity-violating inelastic differential cross section to the

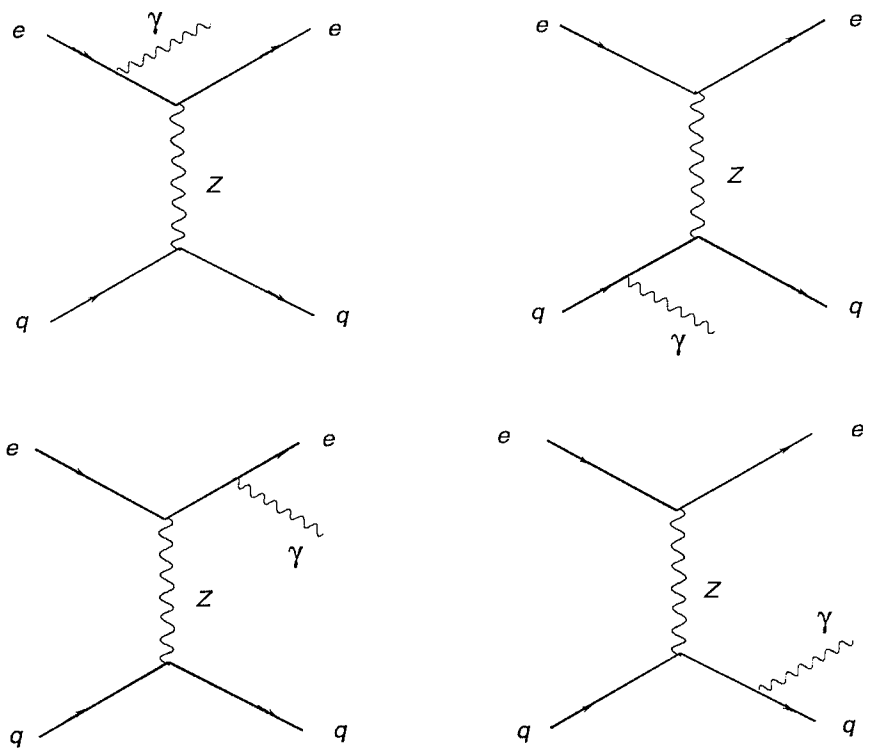

Figure 12: Bremsstrahlung diagrams for treating IR divergences.

radiative correction can also be expressed in terms of the parity-violating elastic Born cross section, once the appropriate integrals over phase space are done. The steps involved in carrying out the phase space integrals are analogous to ordinary parity-conserving electron scattering, as discussed for example in the paper by Maximon and Tjon [40]. We refer the reader to that paper for details, and simply present the result that

$$d\sigma_{\rm b}^{eq} = d\sigma_{\rm Born}^{eq}\kappa_{\rm soft}^{eq}, \tag{127}$$

where $\kappa_{\rm soft}^{eq}$ is the soft-photon factor defined as

$$\kappa_{\rm soft}^{eq} = -\frac{\alpha}{2\pi^2}\int_{|\mathbf{k}|\leq\Delta\varepsilon}\frac{d^3k}{2\sqrt{\mathbf{k}^2+\lambda^2}}\left(-\frac{p_1}{(p_1\cdot k)}+\frac{p_3}{(p_3\cdot k)}+\frac{Q_q p_2}{(p_2\cdot k)}-\frac{Q_q p_4}{(p_4\cdot k)}\right)^2. \tag{128}$$

Here $\Delta\varepsilon$ is the maximum momentum of the undetected photon for which an elastic scattering event is recorded, which is related to the final electron detector acceptance in the lab frame, ΔE.

Adding together the elastic and inelastic cross sections, we have

$$d\sigma_{\rm tot}^{eq} \sim \left|\mathcal{M}_{\rm Born}^{\gamma}+\mathcal{M}_{\rm rad}^{\gamma}+\mathcal{M}_{\rm Born}^{Z}+\mathcal{M}_{\rm rad}^{Z}\right|^2+\left|\mathcal{M}_{\rm Born}^{\gamma}+\mathcal{M}_{\rm Born}^{Z}\right|^2\kappa_{\rm soft}^{eq}, \tag{129}$$

where $\mathcal{M}_{\rm rad}^{\gamma}$ and $\mathcal{M}_{\rm rad}^{Z}$ denote the one-loop radiative corrections. Note that at this stage, our expression (129) also includes the purely QED radiative corrections $\mathcal{M}_{\rm rad}^{\gamma}$ to the Born amplitude $\mathcal{M}_{\rm Born}^{\gamma}$. $\mathcal{M}_{\rm rad}^{\gamma}$ includes vertex and $\gamma\gamma$ box diagrams of order $\mathcal{O}(\alpha^2)$.

For the PV contribution, it is convenient to work with the amplitude $\mathcal{M}^{eq}_{\rm PV}$ defined in Eq. (101), from which we can write the relevant PV interference term as

$$d\sigma^{eq}_{\rm PV,tot} \sim 2{\rm Re}\left\{ \begin{array}{c} \left(\mathcal{M}^{\gamma}_{\rm Born}\right)^* \left(\mathcal{M}^{eq}_{\rm PV,tree} + \mathcal{M}^{eq}_{\rm PV,rad} + \mathcal{M}^{eq}_{\rm PV,tree}\frac{1}{2}\kappa^{eq}_{\rm soft}\right) \\ + \left(\mathcal{M}^{eq}_{\rm PV,tree}\right)^* \left(\mathcal{M}^{\gamma}_{\rm rad} + \mathcal{M}^{\gamma}_{\rm Born}\frac{1}{2}\kappa^{eq}_{\rm soft}\right) \end{array} \right\}. \qquad (130)$$

At this point we note that the second term of Eq. (130) involves a PV interference term between $\mathcal{M}^{\gamma}_{\rm rad}$ and $\mathcal{M}^{eq}_{\rm PV,tree}$, plus the soft photon emission contribution needed to cancel the IR divergences in $\mathcal{M}^{\gamma}_{\rm rad}$. In principle, one should use the full expression (130) to evaluate both the QED and weak radiative corrections on the same footing, since they contribute to the PV asymmetry at the same order. In practice, this has not been done. We take the position here that experimental analyses have already accounted for the QED radiative corrections, and to include such effects again here would be double counting. Accordingly, we drop the second term in Eq. (130) from further consideration at this time.

Using the general structure of the PV amplitude in Eq. (101), we can rewrite the first term in Eq. (130) as

$$d\sigma^{eq}_{\rm PV,tot} \sim 2{\rm Re}\left\{ \begin{array}{c} \left(\mathcal{M}^{\gamma}_{\rm Born}\right)^* [\left(1 + R^q_A + \frac{1}{2}\kappa^{eq}_{\rm soft}\right) A^{eq}_{\rm tree} J^{eq}_{VA} \\ + \left(1 + R^q_V + \frac{1}{2}\kappa^{eq}_{\rm soft}\right) B^{eq}_{\rm tree} J^{eq}_{AV}] \end{array} \right\}, \qquad (131)$$

where current products J^{eq}_{VA} and J^{eq}_{AV} are defined in Eq. (101).

Evaluating Eq. (128), we have

$$\kappa^{eq}_{\rm soft} = -\frac{\alpha}{2\pi^2}[2m_e^2 I\left(p_1,p_1\right) - \left(2m_e^2 - t\right) I\left(p_1,p_3\right) + 2Q_q^2 m_q^2 I\left(p_2,p_2\right)$$

$$-Q_q^2\left(2m_q^2-t\right)I\left(p_2,p_4\right)-2Q_q\left(u-m_e^2-m_q^2\right)I\left(p_1,p_4\right) \tag{132}$$

$$-2Q_q\left(s-m_e^2-m_q^2\right)I\left(p_1,p_2\right)],$$

with the soft-photon emission integral $I\left(p_i,p_j\right)$ defined as

$$I\left(p_i,p_j\right)=\int_{|\mathbf{k}|\leq\Delta\varepsilon}\frac{d^3k}{2\sqrt{\mathbf{k}^2+\lambda^2}}\frac{1}{\left(p_i\cdot k\right)\left(p_j\cdot k\right)}. \tag{133}$$

These integrals generally have been worked out in Ref. [29]. For electron-quark scattering in the CM frame, we have (see also Ref. [23])

$$\begin{aligned}I\left(p_i,p_j\right)=&\frac{2\pi\alpha_{ij}}{\alpha_{ij}^2m_i^2-m_j^2}[\frac{1}{2}\ln\left(\frac{\alpha_{ij}^2m_i^2}{m_j^2}\right)\ln\left(\frac{4\Delta\varepsilon^2}{\lambda^2}\right)+\frac{1}{4}\ln^2\left(\frac{E_i-p_i}{E_i+p_i}\right)\\&-\frac{1}{4}\ln^2\left(\frac{E_j-p_j}{E_j+p_j}\right)+\mathrm{Li}_2\left(1-\frac{\alpha_{ij}}{v_{ij}}\left(E_i+p_i\right)\right)\\&+\mathrm{Li}_2\left(1-\frac{\alpha_{ij}}{v_{ij}}\left(E_i-p_i\right)\right)-\mathrm{Li}_2\left(1-\frac{1}{v_{ij}}\left(E_j+p_j\right)\right)-\mathrm{Li}_2\left(1-\frac{1}{v_{ij}}\left(E_j-p_j\right)\right)],\end{aligned} \tag{134}$$

where $v_{ij}=(\alpha_{ij}^2m_i^2-m_j^2)/(2\left(\alpha_{ij}E_i-E_j\right))$, and (E_i,p_i) are the energy and momentum in the CM system. The parameters for different values of i,j are given in Table 4. Li_2 is the dilogarithm function

$$\mathrm{Li}_2(z)=\int_z^0 dt\,\frac{\ln(1-t)}{t}. \tag{135}$$

The IR divergent $(\ln\lambda)$ terms in the elastic and inelastic contributions to the radiative correction cancel exactly. In particular, if we define the modified radiative correction factors

$$\tilde{R}_V^q \equiv R_V^q+\frac{1}{2}\kappa_{\mathrm{soft}}^{eq}, \tag{136}$$

$$\tilde{R}_A^q \equiv R_A^q+\frac{1}{2}\kappa_{\mathrm{soft}}^{eq}. \tag{137}$$

i	j	m_i	m_j	α_{ij}
1	1	m_e	m_e	1
2	2	m_q	m_q	1
1	3	m_e	m_e	$1-\frac{t}{2m_e^2}+\frac{\sqrt{t^2-4tm_e^2}}{2m_e^2}$
2	4	m_q	m_q	$1-\frac{t}{2m_f^2}+\frac{\sqrt{t^2-4tm_f^2}}{2m_f^2}$
1	4	m_e	m_q	$\frac{m_e^2+m_f^2-u+\sqrt{\left(u-m_e^2-m_f^2\right)^2-4m_e^2m_f^2}}{2m_e^2}$
1	2	m_e	m_q	$\frac{s-m_e^2-m_f^2+\sqrt{\left(m_e^2+m_f^2-s\right)^2-4m_e^2m_f^2}}{2m_e^2}$

Table 4: Soft photon emission integral parameters of Eq.(134).

then $\tilde{R}_V^q$ and $\tilde{R}_A^q$ are the radiative corrections to electron-quark scattering free of IR divergences. This was confirmed numerically in our calculation by varying the parameter λ over several orders of magnitude, with no numerically significant change in $\tilde{R}$.

There remains a weak logarithmic dependence on $\Delta\varepsilon$ of the form $\ln(\Delta\varepsilon/m)$. This dependence will be cancelled if hard photon bremsstrahlung is taken into account. This requires knowledge of particular experimental details such as detector geometry, energy resolution, phase space cuts, etc. This is beyond the scope of this thesis, and we have chosen to simply set the scale for these effects by choosing an energy resolution ΔE corresponding to the parameters of the corresponding detector. We leave a more complete treatment of the hard bremsstrahlung corrections, as well as

the simultaneous treatment of both QED and weak radiative corrections, as a future project.

4 Results

4.1 Numerical Results

4.1.1 SAMPLE I and SAMPLE II

The parameters of the Standard Model are taken from Ref. [46], and are given in Table 5.

As discussed by Hollik [26], the masses of the light quarks are regarded as parameters and have to be adjusted. The adjustment is made necessary by quark-antiquark interactions in the loops, i.e. hadronic vacuum polarization. Instead of the constituent or bare quark masses, we consider the effective quark mass modified to reproduce the results of a dispersion analysis for the $e^+e^- \rightarrow hadron$ process, normalized by the $e^+e^- \rightarrow \mu^+\mu^-$ scattering cross section for the low-energy region [46].

For kinematical input, we have chosen the SAMPLE I and II kinematics, corresponding to $E_{e,\mathrm{lab}} = 194$ MeV and an average backward scattering angle $\theta = 146.2°$. Radiative correction results for the $V(e) \times A(q)$ and $A(e) \times V(q)$ current interactions are given separately in the Table 6 for u, d, and s quarks.

The contributions from self-energy, triangle, and box classes of diagrams are shown

Quantity	Value	Quantity	Value
m_u	47 MeV	m_e	0.51100 MeV
m_d	47 MeV	m_μ	105.66 MeV
m_s	150 MeV	m_τ	1777.0 MeV
m_c	1.25 GeV	M_Z	91.1882 GeV
m_b	4.2 GeV	M_W	80.419 GeV
m_t	174.3 GeV	M_H	100 GeV

Table 5: Standard Model parameters used in this calculation.

for loops which do not involve photons. The self-energy (SE) diagrams give the dominant contribution to radiative corrections in most of the cases. Triangle and box diagrams that involve photon loops are shown as a combined result in column 5 because they are separately infrared divergent. In the combined result, the infrared divergence is cancelled by the bremsstrahlung corrections for soft-photon emission. The corrections show a weak logarithmic dependence on the resolution of the detector, ΔE. Using the expression

$$\Delta E = \frac{E_{lab}}{1 + 2(\sin\frac{\theta}{2})\frac{E_{lab}}{M_N}} - 0.02 \text{ GeV},$$

we have obtained 120 MeV. This corresponds roughly to the parameters of the SAMPLE detector, which detects all electrons above the Čerenkov threshold of 20 MeV [41].

$R_{VA}^{ff'}$	Self Energy	Vertex (no γ)	Box (no γ)	Vetrex+Box (with γ)	Total
eu	-0.278	-0.224	0.096	0.114	-0.292
ed	-0.278	-0.164	0.022	-0.083	-0.503
es	-0.293	-0.198	0.022	-0.081	-0.550
ue	-0.059	-0.015	0.027	0.019	-0.028
de	-0.025	0.026	0.002	0.004	0.008
se	-0.025	0.026	0.002	0.015	0.017

Table 6: Radiative corrections for one-quark currents at SAMPLE I and II kinematics ($E_{\rm lab} = 194$ MeV, $\theta = 146.2°$, $\Delta E = 120$ MeV).

	T=0	T=1	isosinglet	p	n
R_V	0.057	-0.005	0.029	-0.252	0.022
R_A	-0.210	-0.398	-0.760	-0.608	-0.187

Table 7: Radiative corrections for nucleon currents at SAMPLE I and II kinematics.

The calculated one-quark radiative corrections were combined to form hadronic vector and axial vector corrections. These are shown in Table 7 for the isoscalar and isovector representations $R_V^{T=0}$, $R_V^{T=1}$, $R_A^{T=0}$, and $R_A^{T=1}$. Also shown are the appropriate linear combinations of isoscalar and isovector corrections for the proton (R_V^p and R_A^p) and the neutron (R_V^n and R_A^n).

We point out again that these values are calculated in the CDR scheme, and also

include a bremsstrahlung contribution. Values calculated in the $\overline{\rm MS}$ scheme tend to be smaller [45], however, the tree level amplitudes also differ between the two schemes due to the different definitions of $\sin^2\theta_W$.

Our theoretical results for the one-quark contributions given in Table 7 need to be supplemented by the many-quark contributions. These have been evaluated using chiral perturbation theory by Zhu *et al.* [57], who found small, predominantly isovector, contributions. Their isovector contribution can be parameterized as $R_A^{T=1} = -0.06 \pm 0.24$, while the isoscalar is $R_A^{T=0} = -0.01 \pm 0.14$. The quoted uncertainties are large, and dominate the overall uncertainties in the theoretical analysis, as described below.

Our error analysis for the theoretical asymmetry takes into account uncertainties in the measured electromagnetic form factors, in the axial contributions $G_A^{(8)}$ and G_A^s, and in the radiative corrections. The largest source of uncertainty in the one-quark radiative corrections is in the soft photon approximation for the bremsstrahlung contributions. We have allowed for a rather generous error estimate by evaluating these corrections for $\Delta E = 60$ MeV, which is half the value used in Table 7.

Our theoretical asymmetry for the above SAMPLE kinematics, including all radiative corrections, and adding errors in quadrature, can be written to show the explicit dependence on the strange form factors:

$$A_p^{\rm th} = (-7.29 \pm 0.65) + (3.61 \pm 0.07) G_M^s(0.1) + 1.94 G_E^s(0.1), \qquad (138)$$

$$A_d^{\rm th} = (-8.74 \pm 0.89) + (0.82 \pm 0.05) G_M^s(0.1) + 1.46 G_E^s(0.1). \qquad (139)$$

For no strange quark contribution, the measured asymmetries are smaller than the theoretical ones. The discrepancy between the theoretical and experimental values for A_p and A_d are about the same, whereas the coefficients of the dominant G_M^s term are considerably different.

In our analysis we have used the recent nucleon electromagnetic form factors determined by Brash *et al.* [13]. At $Q^2 = 0.1$ GeV, these nucleon form factors tend to be smaller than in the Galster parameterization, thereby exacerbating the discrepancy between theoretical and experimental values noted in previous work [41, 54]. The axial form factors are taken to be a simple dipole form, following Refs. [45, 41].

The contribution from G_E^s for these kinematics is expected to be small. For the range of values of the strange radius $r_s^2 = \pm 0.22$ found in the literature, we expect $G_E^s(0.1)$ to be in the range ∓ 0.10. For comparison, the neutron electric form factor has the value $G_E^n(0.1) = 0.036$. HAPPEX [4] has measured the asymmetry A_p at $\theta = 12.3^\circ$ and $Q^2 = 0.477$. They find the linear combination $(G_E^s + 0.392 G_M^s) = 0.025 \pm 0.020 \pm 0.014$, which would seem to favor a positive value of G_E^s. A measurement at $Q^2 = 0.1$ is underway, and could shed some light on the SAMPLE result.

Because the largest overall uncertainty in the theoretical calculations is from $R_A^{T=1}$, it is useful to follow the analysis of the SAMPLE papers [41] and isolate this term

explicitly. In this case, we have

$$A_p^{\rm th} = (-5.93 \pm 0.27) + (3.61 \pm 0.07) G_M^s(0.1) + (2.34 \pm 0.03) G_A^{Z,T=1}(0.1), \quad (140)$$

$$A_d^{\rm th} = (-7.10 \pm 0.40) + (0.82 \pm 0.05) G_M^s(0.1) + (2.83 \pm 0.04) G_A^{Z,T=1}(0.1). \quad (141)$$

We have dropped the G_E^s terms, and have added (in quadrature) an additional uncertainty ± 0.18 to A_p and ± 0.14 to A_d. The isoscalar terms in G_A^Z, shown in Eq. (43) have been absorbed into the constant term. The axial isovector contribution is

$$G_A^{Z,T=1}(0.1) = -(1 + R_A^{T=1}) G_A^{T=1}(0.1), \quad (142)$$

which has the theoretically expected value $G_A^{Z,T=1}(0.1) = -0.58 \pm 0.27$. This includes the large effect of the one quark axial correction ($R_A^{T=1} = -0.40 \pm 0.02$), and the highly uncertain many-quark contribution ($R_A^{T=1} = -0.06 \pm 0.24$) of Ref. [57]. Figure 13 demonstrates the excellent agreement of our calculated $G_A^{Z,T=1}$ value with an improved analysis of the SAMPLE deuterium and hydrogen data.

Because the coefficients of $G_A^{Z,T=1}$ in Eqs. (140) and (141) are roughly equal, changes in $G_A^{Z,T=1}$ will shift A_p and A_d by about the same amount. This is consistent with the uniform discrepancy between theory and experiment in A_p and A_d referred to above, and so it is useful to try to fit the data in this way. However, there may be other explanations for such a uniform discrepancy, including other physics, or

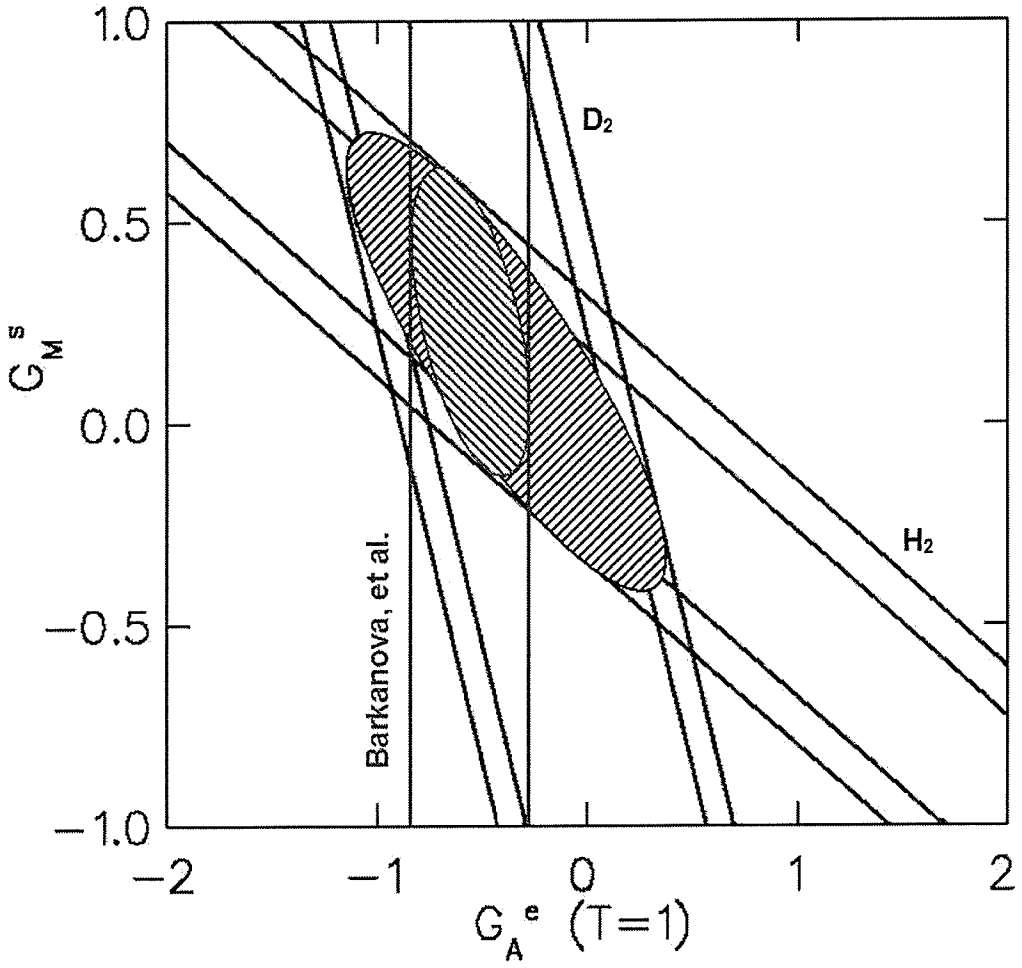

Figure 13: The theoretical expectation for the axial form factor vs updated results from the 200 MeV SAMPLE data.

systematic errors in the experimental analysis of the kind determined by Spayde [54]. Hence we regard this as simply a device for characterizing the data, and indicating possible directions for explanation.

Solving the pair of equations (140) and (141) for G_M^s and $G_A^{Z,T=1}$, and using the measured asymmetries from Eqs. (47) and (48), we find

$$G_M^s(Q^2 = 0.1) = 0.16 \pm 0.50, \tag{143}$$

$$G_A^{Z,T=1}(Q^2 = 0.1) = -0.11 \pm 0.49. \tag{144}$$

Combining the errors in the extracted value of G_A^Z and the theoretical value quoted above, the difference is about 1 σ.

There is some uncertainty about how to extrapolate $G_M^s(Q^2 = 0.1)$ to $\mu_s = G_M^s(Q^2 = 0)$. A simple dipole form consistent with the proton and neutron magnetic electromagnetic form factors would give $\mu_s = 0.21 \pm 0.65$. Using the extrapolation model proposed by Hemmert *et al.* [25], one instead finds a value of the strange magnetic moment $\mu_s = 0.04 \pm 0.50 \pm 0.07$. Here, the last value of the error was introduced in the extrapolation. A negative value of μ_s is consistent with expectations from a number of theoretical models [31, 15, 37, 34]. In particular, recent lattice QCD calculations find $\mu_s = -0.16 \pm 0.18$ [37] and $\mu_s = -0.28 \pm 0.10$ [34]. By contrast, a recent SU(3) chiral quark-soliton model gives $\mu_s = 0.074$ to 0.115 [53].

$R_{VA}^{ff'}$	Self Energy	Vertex (no γ)	Box (no γ)	Vetrex+Box (with γ)	Total
eu	-0.2852	-0.2228	0.0956	0.1126	-0.2998
ed	-0.2852	-0.1602	0.0217	-0.0925	0.5162
es	-0.2990	-0.1984	0.0216	-0.0886	0.5644
ue	-0.0604	-0.0146	0.0269	0.0130	-0.0351
de	-0.0249	0.0255	0.0024	-0.0010	0.0021
se	-0.0256	0.0255	0.0024	0.0094	0.0117

Table 8: Radiative corrections for one-quark currents at SAMPLE III kinematics ($E_{\rm lab} = 120$ MeV, $\theta = 146.2°$, $\Delta E = 77$ MeV).

4.1.2 SAMPLE III

We have repeated the above analysis for the SAMPLE III, which measured the parity-violating asymmetry in electron scattering on deuterium with lower beam energy of 125 MeV [30], yielding $Q^2 \simeq 0.038$ GeV^2. Using the same table structure as in the previous section, we give the radiative corrections for the $V(e) \times A(q)$ and $A(e) \times V(q)$ current interactions in the Table 8 for u, d, and s quarks separately, and the isoscalar and isovector representations $R_V^{T=0}$, $R_V^{T=1}$, $R_A^{T=0}$, and $R_A^{T=1}$ in Table 9.

Differences with the SAMPLE I and II results are mainly due to the bremsstrahlung corrections. This experiment is currently being analyzed. We find

	T=0	T=1	isosinglet	p	n
R_V	0.053	-0.012	0.024	-0.271	0.017
R_A	-0.216	-0.408	-0.781	-0.624	-0.192

Table 9: Radiative corrections for nucleon currents at SAMPLE III kinematics.

$$A_p^{\rm th} = (-2.13 \pm 0.08) + (1.07 \pm 0.02) G_M^s(0.043) + (1.06 \pm 0.01) G_A^{Z,T=1}(0.043), \quad (145)$$

$$A_d^{\rm th} = (-2.62 \pm 0.13) + (0.26 \pm 0.02) G_M^s(0.043) + (1.35 \pm 0.01) G_A^{Z,T=1}(0.043), \quad (146)$$

with the theoretically expected value $G_A^{Z,T=1}(0.043) = -0.62 \pm 0.28$. The overall asymmetries are smaller, and the uncertainties enter somewhat differently than in the SAMPLE I and II kinematics. This should help in determining the role of $G_A^{Z,T=1}$ in the asymmetries.

4.1.3 HAPPEX I

The HAPPEX experiment [7, 4] used $E_{electron} = 3.2$ GeV and $\Theta_{electron} = 12.3°$ yielding $Q^2 \simeq 0.477$ GeV^2. Radiative corrections, corresponding to these kinematics are given in Tables 10 and 11.

As one can see comparing radiative corrections calculated for SAMPLE III and

$R_{VA}^{ff'}$	Self Energy	Vertex (no γ)	Box (no γ)	Vetrex+Box (with γ)	Total
eu	-0.2970	-0.2210	0.0958	0.1434	-0.2788
ed	-0.2970	-0.1544	0.0219	-0.0205	-0.4500
es	-0.3040	-0.1985	0.0216	-0.0231	-0.5040
ue	-0.0625	-0.0147	0.0270	0.0683	0.0181
de	-0.0255	0.0255	0.0024	0.0475	0.0499
se	-0.0259	0.0255	0.0024	0.0520	0.0540

Table 10: Radiative corrections for one-quark currents at HAPPEX I kinematics ($E_{\rm lab} = 3.2$ GeV, $\theta = 12.3°$, $\Delta E = 2.95$ GeV).

	T=0	T=1	isosinglet	p	n
R_V	0.0937	0.0383	0.066	-0.1837	0.0629
R_A	-0.1715	-0.3650	-0.675	-0.5360	-0.1930

Table 11: Radiative corrections for nucleon currents at HAPPEX I kinematics.

HAPPEX I, for example, changing kinematics (the momentum transfer goes from $Q^2 \simeq 0.038$ GeV^2 to $Q^2 \simeq 0.477$ GeV^2 in this case) substantially changes the radiative corrections. The difference is especially noticeable for the corrections of R_V type (compare the first lines of Tables 9 and 11), where $R_V{}^{T=1}$ even changes the sign.

4.1.4 HAPPEX II

The HAPPEX II experiment will measure the PV asymmetry in the elastic scattering of 3.2 GeV electrons from a liquid hydrogen target at a scattering angle of $\Theta_{electron} = 6^\circ$, corresponding to an average $Q^2 \simeq 0.1$ GeV^2 [33]. Such a small change in input parameters comparing to HAPPEX I does not affect the radiative corrections significantly. The values listed in Tables 12 and 13 are not very different from those in Tables 10 and 11.

4.1.5 G0

The Jefferson Lab G0 experiment has a potential to provide the most complete set of observables by measuring backward asymmetries for both proton and deuteron as well as forward proton asymmetries. The experiment will be carried out in three stages, which we for convenience call here (a), (b), and (c). In the first stage of the G0 experiment, forward angle asymmetries are measured by detecting the recoil protons from elastic scattering. For this "forward mode", the beam energy is 3.2 GeV and

$R_{VA}^{ff'}$	Self Energy	Vertex (no γ)	Box (no γ)	Vetrex+Box (with γ)	Total
eu	-0.3070	-0.2190	0.0958	0.1352	-0.2950
ed	-0.3070	-0.1490	0.0216	-0.0270	-0.4614
es	-0.3100	-0.1990	0.0214	-0.0300	-0.5176
ue	-0.0642	-0.0150	0.0270	0.0605	0.0083
de	-0.0260	0.0254	0.0024	0.0411	0.0429
se	-0.0262	0.0255	0.0024	0.0443	0.0460

Table 12: Radiative corrections for one-quark currents at HAPPEX II kinematics ($E_{\rm lab} = 3.2$ GeV, $\theta = 6°$, $\Delta E = 3.12$ GeV).

	T=0	T=1	isosinglet	p	n
R_V	0.0905	0.0302	0.059	-0.2110	0.0570
R_A	-0.1670	-0.3770	-0.684	-0.5447	-0.2116

Table 13: Radiative corrections for nucleon currents at HAPPEX II kinematics.

$R_{VA}^{ff'}$	Self Energy	Vertex (no γ)	Box (no γ)	Vetrex+Box (with γ)	Total
eu	-0.2720	-0.2250	0.0957	0.1253	-0.2760
ed	-0.2720	-0.1670	0.0216	-0.0706	-0.4880
es	-0.2860	-0.1980	0.0216	-0.0676	-0.5300
ue	-0.0579	-0.0145	0.0269	0.0335	-0.0120
de	-0.0242	0.0256	0.0024	0.0132	0.0170
se	-0.0250	0.0256	0.0024	0.0232	0.0262

Table 14: Radiative corrections for one-quark currents at G0 (a) kinematics ($E_{\rm lab}$ = 424 MeV, $\theta = 110°$, $\Delta E = 244$ MeV).

Q^2 covers the entire range of 0.1 to 1 GeV^2. The scattered protons are detected at $\Theta_{proton} = 70° \pm 10°$.

The "backward mode" uses the same beam energy and scattering angles for both proton and deuteron. The scattered electrons are detected at $\Theta_{electron} \simeq 110°$. In the present thesis, only the results for 110° scattering angle are demonstrated. Tables 14 and 15 give the radiative corrections for the $V(e) \times A(q)$ and $A(e) \times V(q)$ current interactions for individual quark contributions, and the isoscalar and isovector representations, correspondingly, calculated for $E_{beam}^{(a)} = 424$ MeV. Tables 16, 17, and 18, 19, give the values obtained for $E_{beam}^{(b)} = 576$ MeV and $E_{beam}^{(c)} = 799$ MeV.

	T=0	T=1	isosinglet	p	n
R_V	0.0570	0.0064	0.0255	-0.1960	0.0288
R_A	-0.2121	-0.3820	-0.742	-0.5940	-0.1697

Table 15: Radiative corrections for nucleon currents at G0 (a) kinematics.

$R_{VA}^{ff'}$	Self Energy	Vertex (no γ)	Box (no γ)	Vetrex+Box (with γ)	Total
eu	-0.2670	-0.2260	0.0957	0.1253	-0.2720
ed	-0.2670	-0.1690	0.0216	-0.0666	-0.4810
es	-0.2820	-0.1980	0.0216	-0.0626	-0.5210
ue	-0.0571	-0.0144	0.0269	0.0353	-0.0093
de	-0.0240	0.0256	0.0024	0.0151	0.0191
se	-0.0247	0.0256	0.0024	0.0250	0.0283

Table 16: Radiative corrections for one-quark currents at G0 (b) kinematics ($E_{\text{lab}} =$ 576 MeV, $\theta = 110°$, $\Delta E = 296$ MeV).

	T=0	T=1	isosinglet	p	n
R_V	0.0580	0.0087	0.0296	-0.1890	0.0306
R_A	-0.2090	-0.3770	-0.7300	-0.5860	-0.1680

Table 17: Radiative corrections for nucleon currents at G0 (b) kinematics.

$R_{VA}^{ff'}$	Self Energy	Vertex (no γ)	Box (no γ)	Vetrex+Box (with γ)	Total
eu	-0.2622	-0.2270	0.0957	0.1239	-0.2696
ed	-0.2622	-0.1710	0.0217	-0.0635	-0.4750
es	-0.2770	-0.1980	0.0216	-0.0596	-0.5130
ue	-0.0562	-0.0144	0.0269	0.0364	-0.0073
de	-0.0237	0.0256	0.0024	0.0161	0.0204
se	-0.0245	0.0256	0.0024	0.0263	0.0298

Table 18: Radiative corrections for one-quark currents at G0 (c) kinematics ($E_{\rm lab}$ = 799 MeV, $\theta = 110°$, $\Delta E = 353$ MeV).

	T=0	T=1	isosinglet	p	n
R_V	0.0585	0.0102	0.0323	-0.1670	0.0317
R_A	-0.2050	-0.3720	-0.7184	-0.5780	-0.1670

Table 19: Radiative corrections for nucleon currents at G0 (c) kinematics.

$R_{VA}^{ff'}$	Self Energy	Vertex (no γ)	Box (no γ)	Vetrex+Box (with γ)	Total
eu	-0.2891	-0.2220	0.0957	0.1378	-0.2776
ed	-0.2891	-0.1580	0.0216	-0.0475	-0.4730
es	-0.2989	-0.1980	0.0216	-0.0467	-0.5220
ue	-0.0611	-0.0146	0.0269	0.0528	0.0040
de	-0.0251	0.0255	0.0024	0.0310	0.0338
se	-0.0261	0.0255	0.0024	0.0385	0.0403

Table 20: Radiative corrections for one-quark currents at A4 (a) kinematics ($E_{\rm lab}$ = 854.3 MeV, $\theta = 35°$, $\Delta E = 713$ MeV).

4.1.6 A4

As well as G0, the parity-violation A4 experiment at Mainz [38] will measure both forward and backward asymmetries, but for the proton only. Up to the moment, the measurements are done at 854.3 MeV and 570 MeV electron beam energy, which lead to momentum transfers of 0.23 GeV^2 and 0.1 GeV^2. The detector covers an angular range from 30° to 40°. We call the stage of the experiment using $E_{beam}^{(a)} = 570$ MeV "A4 (a)", and the stage using $E_{beam}^{(b)} = 799$ MeV as "A4 (b)", for convenience. For the scattering angle, we chose to input $\theta = 35°$. The resulting radiative corrections are given in Tables 20, 21, and 22, 23.

	T=0	T=1	isosinglet	p	n
R_V	0.0748	0.0228	0.0505	-0.1850	0.0459
R_A	-0.1952	-0.3752	-0.7174	-0.5700	-0.1800

Table 21: Radiative corrections for nucleon currents at A4 (a) kinematics.

$R_{VA}^{ff'}$	Self Energy	Vertex (no γ)	Box (no γ)	Vetrex+Box (with γ)	Total
eu	-0.2935	-0.2210	0.0957	0.1348	-0.2840
ed	-0.2935	-0.1560	0.0216	-0.0561	-0.4840
es	-0.3020	-0.1980	0.0216	-0.0556	-0.5340
ue	-0.0619	-0.0147	0.0269	0.0468	0.0029
de	-0.0253	0.0255	0.0024	0.0252	0.0278
se	-0.0258	0.0255	0.0024	0.0322	0.0344

Table 22: Radiative corrections for one-quark currents at A4 (b) kinematics ($E_{\rm lab}$ = 570 MeV, $\theta = 35°$, $\Delta E = 494$ MeV).

	T=0	T=1	isosinglet	p	n
R_V	0.0700	0.0166	0.0426	-0.1974	0.0403
R_A	-0.1995	-0.3840	-0.7340	-0.5833	-0.1843

Table 23: Radiative corrections for nucleon currents at A4 (b) kinematics.

$R_{VA}^{ff'}$	Self Energy	Vertex (no γ)	Box (no γ)	Vetrex+Box (with γ)	Total
eu	-0.3073	-0.2186	0.0957	0.1312	-0.2990
ed	-0.3073	-0.1488	0.0216	-0.0465	-0.4810
es	-0.3103	-0.1985	0.0219	-0.0478	-0.5347
ue	-0.0644	-0.0149	0.0270	0.0492	-0.0031
de	-0.0261	0.0254	0.0024	0.0294	0.0311
se	-0.0262	0.0255	0.0024	0.0340	0.0357

Table 24: Radiative corrections for one-quark currents at Q_{weak} kinematics ($E_{\rm lab}$ = 1.165 GeV, $\theta = 9°$, $\Delta E = 1.127$ GeV).

	T=0	T=1	isosinglet	p	n
R_V	0.0780	0.0186	0.0457	-0.2194	0.0450
R_A	-0.1823	-0.3900	-0.7167	-0.5723	-0.2077

Table 25: Radiative corrections for nucleon currents at Q_{weak} kinematics.

4.1.7 Q_{weak}

The Q_{weak} experiment will measure the parity violating asymmetry in elastic electron-proton scattering at $Q^2 = 0.028$ GeV^2 and $E_{beam} = 1.165$ GeV with the electrons collimated to $\theta_e = 9° \pm 2°$. We list radiative corrections calculated for these kinematics in Tables 24 and 25.

4.2 Analytical Results

To calculate the radiative corrections at given momentum transfer and conserve gauge invariance, one needs to consider a full set of one-loop Feynman diagrams, which can include up to several hundred of diagrams, depending on the particular scattering process. For electron-proton scattering, a full set contains a total of 446 one-loop graphs. The previous section, "Numerical Results", lists radiative corrections obtained by evaluating the full set of diagrams for each of the eight experiments. All of these graphs can be calculated only numerically, of course. New methods and a software package were developed to accomplish this task. However, this software package is not a single user-friendly routine, and it does not work on the "black box" principle, where one would just put the kinematic parameters in and get the radiative corrections out. It takes considerable time and skill to go though all of the steps described in Section 3.2. A faster and simpler method would be a great benefit for use by the growing experimental community.

To address this problem, using the numerical analysis, we singled out the diagrams giving the dominant contributions. Then, we derived analytical momentum-dependent expressions just for these diagrams. As a result, by substituting their own kinematical parameters into these expressions, experimentalists can obtain the applicable radiative corrections very easily and in a very good approximation. Depending on the precision requirements of a given experiment, this analytical estimate may or

may not have to be followed by exact numerical evaluations.

4.2.1 $\{\gamma - Z\}$ boxes

Let us begin from the general form of parity violating amplitude for a box diagram.

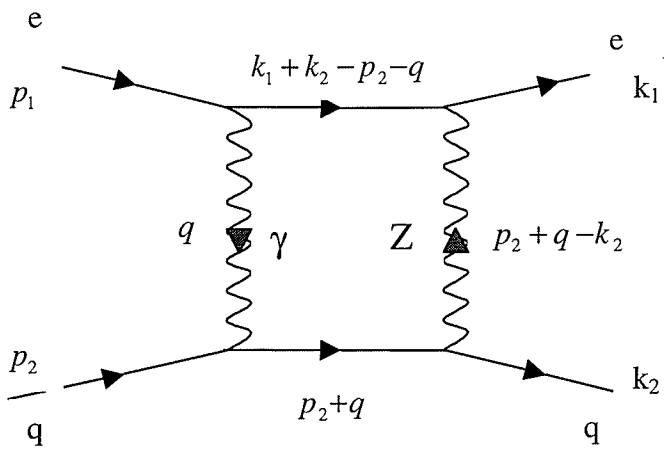

Figure 14: $\{\gamma - Z\}$ box

Although it is imperative to consider the set of all possible topological combinations for $\{\gamma - Z\}$ boxes, in the following example we will show only the $\{\gamma - Z\}$ box from Fig.(14). The final amplitude will be given for the complete set of $\{\gamma - Z\}$ boxes. Using Feynman rules derived from the Weinberg-Salam model, for Fig.(14) we can write:

$$\mathcal{M}^{\gamma-Z} = \frac{ie^4}{16\pi^4}\int d^4q \cdot \overline{u}\left(k_1, m_e\right)\gamma^\mu \left(g_L^{e-Z}\varpi_- + g_R^{e-Z}\varpi_+\right) \cdot \tag{147}$$

$$\cdot\frac{m_e+\not k_1+\not k_2-\not q-\not p_2}{(k_1+k_2-q-p_2)^2-m_e^2}\cdot$$

$$\cdot\gamma^\nu\left(g_L^{e-\gamma}\varpi_-+g_R^{e-\gamma}\varpi_+\right)u(p_1,m_e)\cdot\overline{u}(k_2,m_q)\,\gamma^\alpha\left(g_L^{q-Z}\varpi_-+g_R^{q-Z}\varpi_+\right)\cdot$$

$$\cdot\frac{m_q+\not q+\not p_2}{(q+p_2)^2-m_q^2}\gamma^\beta\left(g_L^{q-\gamma}\varpi_-+g_R^{q-\gamma}\varpi_+\right)u(p_2,m_q)\,\frac{g_{\nu\beta}}{q^2}\,\frac{g_{\mu\alpha}}{(q+p_2-k_2)^2-m_Z^2},$$

where $g_{L,R}^{\{e,q\}-\{\gamma,Z\}}$ are the coupling constants. In Chapter 2, we have the coupling constants defined according to Eq. (91). This is the form most usually found in North American literature. We show this for illustrative purposes only; in practice, it is more convenient to absorb the $1/\cos\theta_W\sin\theta_W$ term, found in every term of every amplitude (see Eq. (93), for example), into the coupling constants:

$$\begin{aligned} g_V^f &\rightarrow \frac{g_V^f}{\cos\theta_W\sin\theta_W}, \\ g_A^f &\rightarrow \frac{g_A^f}{\cos\theta_W\sin\theta_W}. \end{aligned} \tag{148}$$

In addition, in some cases we split g_V^f and g_A^f into left- and right-handed components, defined by

$$\begin{aligned} g_V^{f-Z} &= \frac{g_L^{f-Z}+g_R^{f-Z}}{2}, \\ g_A^{f-Z} &= \frac{g_L^{f-Z}-g_R^{f-Z}}{2}. \end{aligned} \tag{149}$$

Integration can be performed by using the tensor decomposition approach (see

Eq. (110)). The results are expressed as a combination of tensor coefficient functions multiplied by various form factors. Tensor coefficient functions can be reduced into a set of scalar integrals with the help of the tensor reduction algorithms. There is no need to provide details on the tensor reduction approach here because tensor coefficient functions have been computed numerically in the first place. We can leave tensor coefficient functions unevaluated in our analysis.

Before going into explicit details of the PV amplitude for $\{\gamma - Z\}$ boxes, let us adopt a new, shortened notation for four and three point tensor coefficient functions:

$$C_{ij}\left(T, m_q^2, m_q^2, m_x^2, m_y^2, m_q^2\right) \equiv C_{ij}^T\left(m_x^2, m_y^2\right), \tag{150}$$

$$D_{ij}\left(m_e^2, S, m_q^2, T, m_q^2, m_e^2, m_x^2, m_e^2, m_q^2, m_y^2\right) \equiv D_{ij}^{S,T}\left(m_x^2, m_y^2\right),$$

$$D_{ij}\left(m_e^2, T, m_q^2, U, m_e^2, m_q^2, m_e^2, m_x^2, m_y^2, m_q^2\right) \equiv D_{ij}^{T,U}\left(m_x^2, m_y^2\right).$$

Taking only the PV vector axial part of the amplitude (147), we obtain:

$$\mathcal{M}_{VA}^{\gamma-Z} = \frac{\alpha^2}{2} g^{e-\gamma} g^{q-\gamma} ((g_L^{e-Z} + g_R^{e-Z})(g_L^{q-Z} - g_R^{q-Z})[(m_e^2 + m_q^2 - S) D_0^{S,T}(0, m_Z^2) +$$

$$(2m_e^2 + m_q^2 - S)(D_1^{S,T}(0, m_Z^2) + 2D_{13}^{S,T}(0, m_Z^2)) + 2m_e^2 D_{11}^{S,T}(0, m_Z^2) +$$

$$(m_e^2 + 2m_q^2 - S)(D_2^{S,T}(0, m_Z^2) + 2D_{23}^{S,T}(0, m_Z^2)) + 2m_q^2 D_{22}^{S,T}(0, m_Z^2) +$$

$$2(m_e^2+m_q^2-S)(D_3^{S,T}(0,m_Z^2)+2D_{33}^{S,T}(0,m_Z^2))]+$$

(151)

$$+2\left(4g_L^{e-Z}g_L^{q-Z}+g_R^{e-Z}g_L^{q-Z}-g_L^{e-Z}g_R^{q-Z}-4g_R^{e-Z}g_R^{q-Z}\right)D_{00}^{S,T}\left(0,m_Z^2\right)+$$

$$\left(3g_L^{e-Z}g_L^{q-Z}+2g_R^{e-Z}g_L^{q-Z}-2g_L^{e-Z}g_R^{q-Z}-3g_R^{e-Z}g_R^{q-Z}\right)D_{12}^{S,T}\left(0,m_Z^2\right)\cdot$$

$$\cdot(m_e^2+m_q^2-S))\left(\overline{u}_e\gamma_\mu u_e\right)\left(\overline{u}_q\gamma_\mu\gamma_5 u_q\right),$$

and for the axial vector part

$$\mathcal{M}_{AV}^{\gamma-Z} = \frac{\alpha^2}{2}g^{e-\gamma}g^{q-\gamma}((g_L^{e-Z}-g_R^{e-Z})(g_L^{q-Z}+g_R^{q-Z})[(m_e^2+m_q^2-S)D_0^{S,T}(0,m_Z^2)+$$

$$(2m_e^2+m_q^2-S)(D_1^{S,T}(0,m_Z^2)+2D_{13}^{S,T}(0,m_Z^2))+2m_e^2D_{11}^{S,T}(0,m_Z^2)+$$

$$(m_e^2+2m_q^2-S)(D_2^{S,T}(0,m_Z^2)+2D_{23}^{S,T}(0,m_Z^2))+2m_q^2D_{22}^{S,T}(0,m_Z^2)+$$

$$2(m_e^2+m_q^2-S)(D_3^{S,T}(0,m_Z^2)+2D_{33}^{S,T}(0,m_Z^2))]+$$

(152)

$$+2\left(4g_L^{e-Z}g_L^{q-Z}-g_R^{e-Z}g_L^{q-Z}+g_L^{e-Z}g_R^{q-Z}-4g_R^{e-Z}g_R^{q-Z}\right)D_{00}^{S,T}\left(0,m_Z^2\right)+$$

$$\left(3g_L^{e-Z}g_L^{q-Z} - 2g_R^{e-Z}g_L^{q-Z} + 2g_L^{e-Z}g_R^{q-Z} - 3g_R^{e-Z}g_R^{q-Z}\right) D_{12}^{S,T}\left(0, m_Z^2\right) \cdot$$

$$\cdot(m_e^2 + m_q^2 - S)) \left(\overline{u}_e \gamma_\mu \gamma_5 u_e\right) \left(\overline{u}_q \gamma_\mu u_q\right).$$

Note that VA and AV amplitudes differ only by coefficients with combinations of left and right handed couplings. If all $\{\gamma - Z\}$ boxes are to be presented, the latter notation for couplings will make the final amplitude cumbersome. In this case, instead of left and right handed couplings between fermions and vector bosons, we shall use the couplings between the fermion's vector and axial vector currents to the vector boson, defined by Eq. (149).

The following properties of the many-point tensor coefficients also help to simplify the amplitude:

$$C_0^T(m_Z^2, 0) = C_0^T(0, m_Z^2), \tag{153}$$

$$D_{0,00,1,11,2,12,22}^{S,T}(0, m_Z^2) = D_{0,00,1,11,2,12,22}^{S,T}(m_Z^2, 0),$$

$$D_{13,23,3,33}^{S,T}(0, m_Z^2) = 0,$$

$$D_{1,11,12,13}^{T,U}(m_Z^2, 0) = D_{12,2,23}^{T,U}(0, m_Z^2) = 0,$$

$$D^{T,U}_{0,00,3,33}(0,m_Z^2) = D^{T,U}_{0,00,3,33}(m_Z^2,0).$$

Now, the final amplitude for $\{\gamma - Z\}$ boxes can be expressed as the following sum of vector-axial and axial-vector terms:

(1) vector-axial part:

$$\mathcal{M}^{\gamma-Z}_{VA} = -\frac{\alpha^2}{4} g^{e-\gamma} g^{q-\gamma} (g_A^{q-Z} g_V^{e-Z} [-8C_0^T(m_Z^2,0) + 4(m_e^2 + m_q^2 - S) D_0^{S,T}(m_Z^2,0) -$$

$$12m_e^2 D_0^{T,U}(m_Z^2,0) - 4(m_q^2 - T - U)(D_1^{S,T}(m_Z^2,0) + D_{13}^{S,T}(m_Z^2,0)) -$$

$$2(2m_e^2 + m_q^2 - S - T) D_1^{T,U}(0,m_Z^2) + 4m_e^2(2D_{11}^{S,T}(m_Z^2,0) + D_{11}^{T,U}(0,m_Z^2)) -$$

$$2(m_e^2 - T - U)(D_2^{S,T}(0,m_Z^2) + 2D_{23}^{S,T}(m_Z^2,0)) -$$

$$2(m_e^2 - 2m_q^2 - T - U) D_2^{S,T}(m_Z^2,0) - 2(4m_e^2 + m_q^2 - S - T) D_2^{T,U}(m_Z^2,0) +$$

$$8m_q^2 D_{22}^{S,T}(m_Z^2,0)) - 4(m_e^2 + m_q^2 - T - U)(D_3^{S,T}(m_Z^2,0) + D_{33}^{S,T}(m_Z^2,0))] + \tag{154}$$

$$4(5g_A^{q-Z} g_V^{e-Z} + 3g_V^{q-Z} g_A^{e-Z}) D_{00}^{S,T}(m_Z^2,0) + 12(g_A^{q-Z} g_V^{e-Z} + g_V^{q-Z} g_A^{e-Z}) D_{00}^{T,U}(0,m_Z^2) +$$

$$2((m_e^2+m_q^2-S)g_V^{q-Z}g_A^{e-Z}-(3m_e^2+3m_q^2+S-4T-4U)g_A^{q-Z}g_V^{e-Z})D_{12}^{S,T}(m_Z^2,0)+$$

$$((m_e^2+m_q^2-S)g_V^{q-Z}g_A^{e-Z}+(5m_e^2+m_q^2-S)g_A^{q-Z}g_V^{e-Z})D_{13}^{T,U}(0,m_Z^2)+$$

$$((m_e^2-3m_q^2-S)g_A^{q-Z}g_V^{e-Z}+(m_e^2+m_q^2-S)g_V^{q-Z}g_A^{e-Z})D_{23}^{T,U}(m_Z^2,0)+$$

$$2((m_e^2+m_q^2-S)g_V^{q-Z}g_A^{e-Z}-(9m_e^2+7m_q^2-3S-4T)g_A^{q-Z}g_V^{e-Z})D_3^{T,U}(m_Z^2,0)+$$

$$2(g_A^{q-Z}g_V^{e-Z}+g_V^{q-Z}g_A^{e-Z})(m_e^2+m_q^2-S)D_{33}^{T,U}(m_Z^2,0))\,(\overline{u}_e\gamma_\mu u_e)\,(\overline{u}_q\gamma_\mu\gamma_5 u_q)$$

(2) and axial-vector part:

$$\mathcal{M}_{AV}^{\gamma-Z}=-\frac{\alpha^2}{4}g^{e-\gamma}g^{q-\gamma}(g_V^{q-Z}g_A^{e-Z}[-8C_0^T(m_Z^2,0)+4(m_e^2+m_q^2-S)D_0^{S,T}(m_Z^2,0)-$$

$$8m_e^2D_0^{T,U}(m_Z^2,0)+2(2m_e^2+m_q^2-S)(D_1^{S,T}(m_Z^2,0)+2D_{13}^{S,T}(m_Z^2,0))+$$

$$2(4m_e^2+m_q^2-S)D_1^{S,T}(m_Z^2,0)-2(m_q^2-S-T)D_1^{T,U}(0,m_Z^2)-$$

$$4m_e^2(2D_{11}^{S,T}(m_Z^2,0)+D_{11}^{T,U}(0,m_Z^2))-\ 4(m_e^2+2m_q^2-S)\cdot$$

$$\cdot(D_2^{S,T}(0,m_Z^2)+D_{23}^{S,T}(m_Z^2,0))-2(4m_e^2+m_q^2-S-T)D_2^{T,U}(m_Z^2,0)+$$

$$8m_q^2D_{22}^{S,T}(m_Z^2,0))+4(m_e^2+m_q^2-S)(D_3^{S,T}(m_Z^2,0)+D_{33}^{S,T}(m_Z^2,0))]+ \tag{155}$$

$$4(5g_V^{q-Z}g_A^{e-Z}+3g_A^{q-Z}g_V^{e-Z})D_{00}^{S,T}(m_Z^2,0)+12(g_A^{q-Z}g_V^{e-Z}+g_V^{q-Z}g_A^{e-Z})D_{00}^{T,U}(0,m_Z^2)+$$

$$2(m_e^2+m_q^2-S)(g_A^{q-Z}g_V^{e-Z}+5g_V^{q-Z}g_A^{e-Z})D_{12}^{S,T}(m_Z^2,0)+$$

$$((m_e^2+m_q^2-S)g_A^{q-Z}g_V^{e-Z}+(5m_e^2+m_q^2-S)g_V^{q-Z}g_A^{e-Z})D_{13}^{T,U}(0,m_Z^2)+$$

$$((m_e^2-3m_q^2-S)g_V^{q-Z}g_A^{e-Z}+(m_e^2+m_q^2-S)g_A^{q-Z}g_V^{e-Z})D_{23}^{T,U}(m_Z^2,0)+$$

$$2((m_e^2+m_q^2-S)g_A^{q-Z}g_V^{e-Z}-(9m_e^2+7m_q^2-3S-4T)g_V^{q-Z}g_A^{e-Z})D_3^{T,U}(m_Z^2,0)+$$

$$2(g_A^{q-Z}g_V^{e-Z}+g_V^{q-Z}g_A^{e-Z})(m_e^2+m_q^2-S)D_{33}^{T,U}(m_Z^2,0))\cdot(\overline{u}_e\gamma_\mu\gamma_5u_e)(\overline{u}_q\gamma_\mu u_q)$$

4.2.2 $\{Z-Z\}$ boxes

Now let us continue with $\{Z-Z\}$ boxes. Here we have only two diagrams which all together give the following result after taking into account the properties of four point tensor coefficients.

Vector-axial part:

$$\mathcal{M}_{VA}^{Z-Z} = \frac{\alpha^2}{8}(4g_A^{q-Z}g_V^{q-Z}((g_A^{e-Z})^2+(g_V^{e-Z})^2)C_0^T(m_Z^2,m_Z^2)-$$

$$2(5g_A^{q-Z}g_V^{q-Z}((g_A^{e-Z})^2+(g_V^{e-Z})^2)+3g_A^{e-Z}g_V^{e-Z}((g_A^{q-Z})^2+(g_V^{q-Z})^2))D_{00}^{S,T}(m_Z^2,m_Z^2)- \tag{156}$$

$$6(g_A^{q-Z}g_V^{q-Z}((g_A^{e-Z})^2+(g_V^{e-Z})^2)+g_A^{e-Z}g_V^{e-Z}((g_A^{q-Z})^2+(g_V^{q-Z})^2))D_{00}^{T,U}(m_Z^2,m_Z^2)) \cdot$$

$$\cdot(\overline{u}_e\gamma_\mu u_e)(\overline{u}_q\gamma_\mu\gamma_5 u_q) \quad ;$$

axial-vector part:

$$\mathcal{M}_{AV}^{Z-Z} = \frac{\alpha^2}{8}(4g_A^{e-Z}g_V^{e-Z}((g_A^{q-Z})^2+(g_V^{q-Z})^2)C_0^T(m_Z^2,m_Z^2)-$$

$$2(5g_A^{e-Z}g_V^{e-Z}((g_A^{q-Z})^2+(g_V^{q-Z})^2)+3g_A^{q-Z}g_V^{q-Z}((g_A^{e-Z})^2+(g_V^{e-Z})^2))D_{00}^{S,T}(m_Z^2,m_Z^2)- \tag{157}$$

$$6(g_A^{q-Z}g_V^{q-Z}((g_A^{e-Z})^2+(g_V^{e-Z})^2)+g_A^{e-Z}g_V^{e-Z}((g_A^{q-Z})^2+(g_V^{q-Z})^2))D_{00}^{T,U}(m_Z^2,m_Z^2)) \cdot$$

$$\cdot \left(\overline{u}_e \gamma_\mu \gamma_5 u_e\right) \left(\overline{u}_q \gamma_\mu u_q\right) \quad .$$

4.2.3 $\{W^{\pm}\}$ boxes

In the case of $\{W^{\pm}\}$ boxes, mixing of three generations of quarks demands the use of CKM matrices. We start with the un-evaluated amplitude for $\{e - q_i^{up}\}$ scattering, where q_i^{up} is "up" type quark:

$$\begin{aligned}
\mathcal{M}_{up}^{W-W} &= \frac{ie^4}{16\pi^4} \sum_{j=1}^{3} \int d^4q \cdot \overline{u}\left(k_1, m_e\right) \gamma^\mu g_L^{e-W} \varpi_- \frac{\not{k}_1 + \not{k}_2 - \not{q} - \not{p}_2}{\left(k_1 + k_2 - q - p_2\right)^2} \cdot \\
&\cdot \gamma^\nu g_L^{e-W} \varpi_- u\left(p_1, m_e\right) \cdot \overline{u}\left(k_2, m_{q_i^{up}}\right) \gamma^\alpha g_L^{q-W} \varpi_- U_{ij} \cdot \\
&\cdot \frac{m_{q_j^{down}} + \not{q} + \not{p}_2}{\left(q + p_2\right)^2 - m_{q_j^{down}}^2} \gamma^\beta g_L^{q-W} \varpi_- U_{ij}^* u\left(p_2, m_{q_i^{up}}\right) \\
&\frac{g_{\nu\beta}}{q^2 - m_W^2} \frac{g_{\mu\alpha}}{\left(q + p_2 - k_2\right)^2 - m_W^2} .
\end{aligned} \tag{158}$$

Here U_{ij} are CKM matrix elements, where we have used the factorization approximation in order to preserve unitarity of the CKM matrix. For simplicity we will adopt the following notation:

$$D_{ij}\left(m_e^2, S, m_{q_i^{up}}^2, T, m_{q_i^{up}}^2, m_e^2, m_W^2, 0, m_{q_j^{down}}^2, m_y^2\right) \equiv D_{ij}^{S,T}\left(0, m_{q_j^{down}}^2\right). \tag{159}$$

Explicit integration leads to equal coefficients for axial-vector and vector-axial parts:

$$\mathcal{M}_{VA(up)}^{W-W} = 4\alpha^2 g_L^{e-W} g_L^{q-W} \sum_{j=1}^{3} |U_{ij}|^2 \left(m_e^2 + m_{q_i^{up}}^2 - S\right) D_{00}^{S,T}\left(0, m_{q_j^{down}}^2\right) \cdot \quad (160)$$

$$\cdot \left(\overline{u}_e \gamma_\mu u_e\right) \left(\overline{u}_q \gamma_\mu \gamma_5 u_q\right),$$

$$\mathcal{M}_{AV(up)}^{W-W} = 4\alpha^2 g_L^{e-W} g_L^{q-W} \sum_{j=1}^{3} |U_{ij}|^2 \left(m_e^2 + m_{q_i^{up}}^2 - S\right) D_{00}^{S,T}\left(0, m_{q_j^{down}}^2\right) \cdot \quad (161)$$

$$\cdot \left(\overline{u}_e \gamma_\mu \gamma_5 u_e\right) \left(\overline{u}_q \gamma_\mu u_q\right).$$

As for the $\left\{e - q_i^{down}\right\}$ scattering amplitude, we have:

$$\mathcal{M}_{down}^{W-W} = \frac{ie^4}{16\pi^4} \sum_{j=1}^{3} \int d^4q \cdot \overline{u}\left(k_1, m_e\right) \gamma^\mu g_L^{e-W} \varpi_- \frac{\not{q}}{q^2} \cdot \quad (162)$$

$$\cdot \gamma^\nu g_L^{e-W} \varpi_- u\left(p_1, m_e\right) \cdot \overline{u}\left(k_2, m_{q_i^{down}}\right) \gamma^\alpha g_L^{q-W} \varpi_- U_{ij}^* \cdot$$

$$\cdot \frac{m_{q_j^{up}} + \not{q} + \not{p}_2 - \not{k}_1}{\left(q + p_2 - k_1\right)^2 - m_{q_j^{up}}^2} \gamma^\beta g_L^{q-W} \varpi_- U_{ij}\, u\left(p_2, m_{q_i^{down}}\right)$$

$$\frac{g_{\nu\beta}}{\left(q - k_1\right)^2 - m_W^2} \frac{g_{\mu\alpha}}{\left(q + p_2 - k_1 - k_2\right)^2 - m_W^2}.$$

Using the following notations,

$$C_{ij}\left(T, m^2_{q_i^{down}}, m^2_{q_i^{down}}, m^2_W, m^2_W, m^2_{q_j^{up}}\right) \equiv C^T_{ij}\left(m^2_W, m^2_{q_j^{up}}\right), \quad (163)$$

$$D_{ij}\left(m^2_e, T, m^2_{q_i^{down}}, U, m^2_e, m^2_{q_i^{down}}, 0, m^2_W, m^2_W, m^2_{q_j^{up}}\right) \equiv D^{T,U}_{ij}\left(0, m^2_{q_j^{up}}\right),$$

we have

$$\mathcal{M}^{W-W}_{VA(down)} = \alpha^2 g_L^{e-W} g_L^{q-W} \sum_{j=1}^{3} |U_{ji}|^2 \left(-C^T_0\left(m^2_W, m^2_{q_j^{up}}\right) + \right. \quad (164)$$

$$\left. 3(m^2_e + m^2_{q_i^{down}} - S) D^{T,U}_{00}\left(0, m^2_{q_j^{up}}\right)\right) \cdot \left(\overline{u}_e \gamma_\mu u_e\right)\left(\overline{u}_q \gamma_\mu \gamma_5 u_q\right)$$

$$\mathcal{M}^{W-W}_{AV(down)} = \alpha^2 g_L^{e-W} g_L^{q-W} \sum_{j=1}^{3} |U_{ji}|^2 \left(-C^T_0\left(m^2_W, m^2_{q_j^{up}}\right) + \right.$$

$$\left. 3(m^2_e + m^2_{q_i^{down}} - S) D^{T,U}_{00}\left(0, m^2_{q_j^{up}}\right)\right) \cdot \left(\overline{u}_e \gamma_\mu \gamma_5 u_e\right)\left(\overline{u}_q \gamma_\mu u_q\right).$$

Many-point tensor coefficients finally can be reduced into a combination of scalar integrals $\{A_0, B_0, C_0 \text{ and } D_0\}$ by using the tensor reduction algorithm.

4.2.4 Self-Energy: $\{Z - Z\}$ Graphs

Self-Energy: fermions in the loop. It is convenient to split self-energy graphs, as in Fig.(15), into two sets, so that fermions and bosons in the loop can be considered

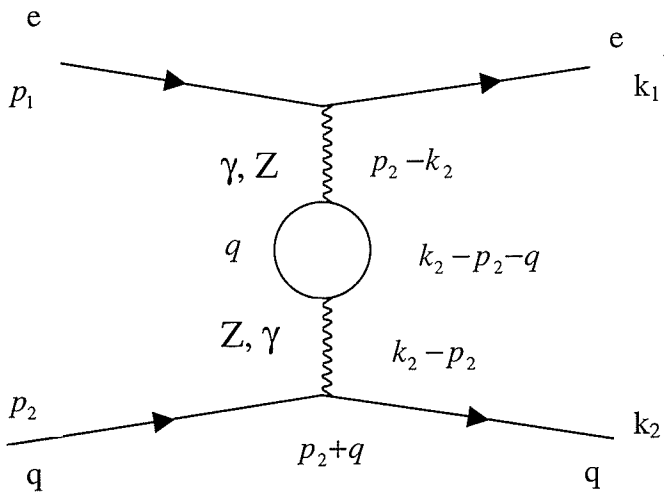

Figure 15: Self-Energy (in the loop, fermions only)

separately. Let us start from the self-energy $\{Z-Z\}$ graph with only fermions in the loop:

$$\mathcal{M}^{Z-Z} = -\frac{ie^4}{16\pi^4}\sum_{i=1}^{12} N_C^{f_i}\int d^4q \cdot \overline{u}\left(k_1, m_e\right)\gamma^\nu\left(g_L^{e-Z}\varpi_- + g_R^{e-Z}\varpi_+\right)u\left(p_1, m_e\right)\cdot \tag{165}$$

$$\overline{u}\left(k_2, m_q\right)\gamma^\mu\left(g_L^{q-Z}\varpi_- + g_R^{q-Z}\varpi_+\right)u\left(p_2, m_q\right)\cdot \mathrm{Tr}[\frac{m_{f_i} - \not{q}}{q^2 - m_{f_i}^2}\gamma^\alpha\left(g_L^{f_i-Z}\varpi_- + g_R^{f_i-Z}\varpi_+\right)\cdot$$

$$\frac{m_{f_i} + \not{k}_2 - \not{q} - \not{p}_2}{\left(k_2 - q - p_2\right)^2 - m_{f_i}^2}\gamma^\beta\left(g_L^{f_i-Z}\varpi_- + g_R^{f_i-Z}\varpi_+\right)]\frac{g_{\nu\beta}}{\left(p_2 - k_2\right)^2 - m_Z^2}\frac{g_{\mu\alpha}}{\left(k_2 - p_2\right)^2 - m_Z^2}.$$

The summation goes over all possible fermion pairs in the loop with $N_C^{f_i}$ standing for the number of colors the fermion f_i can have; $g_{L,R}^{f_i-Z}$ is the coupling constant

between f_i and the Z boson. The amplitude above is divergent, so appropriate counter terms should be added according to the renormalization procedure described previously. This will be done after the amplitudes have been expressed in terms of many-coefficient functions. Using the dimensional reduction scheme to regularize UV divergences, we arrive at the following un-renormalized amplitude:

$$\mathcal{M}^{Z-Z}_{VA(fermion)} = \frac{1}{4}\frac{1}{(T-m_Z^2)^2}\alpha^2 g_V^{e-Z} g_A^{q-Z} \sum_{i=1}^{12} N_C^{f_i} \left(2\left(g_A^{f_i-Z}\right)^2 m_{f_i}^2 B_0(T, m_{f_i}^2, m_{f_i}^2) + \right. \tag{166}$$

$$\left. \left(\left(g_A^{f_i-Z}\right)^2 + \left(g_V^{f_i-Z}\right)^2\right)\left(A_0(m_{f_i}^2) - 2B_{00}(T, m_{f_i}^2, m_{f_i}^2) + T\cdot B_1(T, m_{f_i}^2, m_{f_i}^2)\right)\right)$$

$$\cdot \left(\overline{u}_e \gamma_\mu u_e\right)\left(\overline{u}_q \gamma_\mu \gamma_5 u_q\right) \quad .$$

We have used Eq.(149) to simplify the above expression. As for the axial vector part, we have

$$\mathcal{M}^{Z-Z}_{AV(fermion)} = \frac{1}{4}\frac{1}{(T-m_Z^2)^2}\alpha^2 g_A^{e-Z} g_V^{q-Z} \sum_{i=1}^{12} N_C^{f_i} \left(2\left(g_A^{f_i-Z}\right)^2 m_{f_i}^2 B_0(T, m_{f_i}^2, m_{f_i}^2) + \right. \tag{167}$$

$$\left. \left(\left(g_A^{f_i-Z}\right)^2 + \left(g_V^{f_i-Z}\right)^2\right)\left(A_0(m_{f_i}^2) - 2B_{00}(T, m_{f_i}^2, m_{f_i}^2) + T\cdot B_1(T, m_{f_i}^2, m_{f_i}^2)\right)\right) \quad .$$

$$\cdot \left(\overline{u}_e \gamma_\mu \gamma_5 u_e\right)\left(\overline{u}_q \gamma_\mu u_q\right) .$$

Self-Energy: bosons in the loop. As the second step for $\{Z-Z\}$ diagrams, we include vector, scalar and unitary bosons in the loop (Fig.(16)):

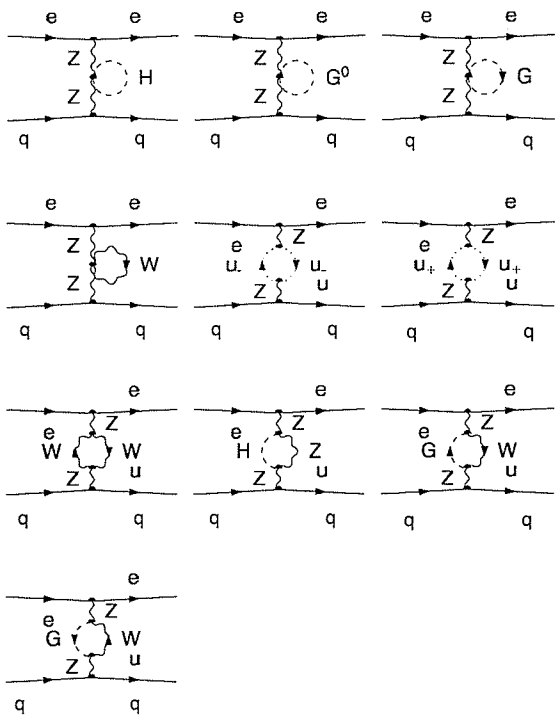

Figure 16: Self-energy (vector, scalar and unitary bosons in the loop)

Here G_0, G are scalar gauge fixing fields with masses of the bosons m_W and m_Z respectively. The unitary ghost fields $u_\pm$ with mass m_W have been introduced to cancel unphysical effects from the gauge fixing part. Because vector-vector, vector-scalar and vector-unitary couplings do not have axial and vector parts, it is more convenient to give final results with these couplings expanded. For the vector-axial

part of the amplitude, we have

$$\mathcal{M}^{Z-Z}_{VA(boson)} = \frac{\alpha^2}{16\, s_W^2\, c_W^4} \frac{g_V^{e-Z} g_A^{q-Z}}{(T-m_Z^2)^2} [(-(8m_W^2+20T)\, c_W^6 + 8m_W^2\ s_W^4\, c_W^2\,)\cdot$$

$$B_0(T,m_W^2,m_W^2) - 8\, c_W^6\, (4B_{00}(T,m_W^2,m_W^2) + T\ \cdot B_1(T,m_W^2,m_W^2)) +$$

(168)

$$c_W^2\, (A_0(m_H^2) + A_0(m_Z^2) + 2(9c_W^4 - 2\, s_W^2\ c_W^2 + s_W^4)\, A_0(m_W^2)) + 4m_W^2\, B_0(T,m_H^2,m_Z^2)] \quad \cdot$$

$$\cdot\, (\overline{u}_e \gamma_\mu u_e)\, (\overline{u}_q \gamma_\mu \gamma_5 u_q)$$

and for the axial-vector part

$$\mathcal{M}^{Z-Z}_{AV(boson)} = \frac{\alpha^2}{16\, s_W^2\, c_W^4} \frac{g_A^{e-Z} g_V^{q-Z}}{(T-m_Z^2)^2} [(-(8m_W^2+20T)\, c_W^6 + 8m_W^2\ s_W^4\, c_W^2\,)\cdot$$

$$B_0(T,m_W^2,m_W^2) - 8\, c_W^6\, (4B_{00}(T,m_W^2,m_W^2) + T\ \cdot B_1(T,m_W^2,m_W^2)) +$$

(169)

$$c_W^2\, (A_0(m_H^2) + A_0(m_Z^2) + 2(9c_W^4 - 2\, s_W^2\ c_W^2 + s_W^4)\, A_0(m_W^2)) + 4m_W^2\, B_0(T,m_H^2,m_Z^2)] \quad \cdot$$

$$\cdot\, (\overline{u}_e \gamma_\mu \gamma_5 u_e)\, (\overline{u}_q \gamma_\mu u_q)\,.$$

To shorten the expressions, notations s_W^2 and c_W^2 are used instead of $\sin_W^2$ and $\cos_W^2$, respectively.

Counterterms. The counterterm for the $\{Z-Z\}$ graph is defined through mass and field renormalization constants of the Z boson. The structure of the counter-terms has been derived from the electro-weak Lagrangian after replacing bare parameters of the Lagrangian with physical ones and corresponding renormalization constants. Thus, for the $\{Z-Z\}$ self-energy graph, we have

$$\delta\mathcal{M}^{Z-Z} = -ie^2\,\overline{u}\,(k_1,m_e)\,\gamma^\nu\left(g_L^{e-Z}\varpi_- + g_R^{e-Z}\varpi_+\right)u\,(p_1,m_e)\cdot$$

$$\overline{u}\,(k_2,m_q)\,\gamma^\mu\left(g_L^{q-Z}\varpi_- + g_R^{q-Z}\varpi_+\right)u\,(p_2,m_q)\,\frac{g_{\alpha\nu}}{(p_2-k_2)^2-m_Z^2}\cdot \tag{170}$$

$$\frac{g_{\beta\mu}}{(k_2-p_2)^2-m_Z^2}(-i\,\delta Z_{ZZ}\,(p_2-k_2)_\alpha\,(k_2-p_2)_\beta + i(\delta Z_{ZZ}\cdot m_Z^2+\delta m_Z^2)g_{\alpha\beta}+$$

$$+i\,\delta Z_{ZZ}\,((p_2-k_2)\cdot(k_2-p_2))\,g_{\alpha\beta}) \quad .$$

Index contraction leads to the following results for the vector-axial part

$$\delta\mathcal{M}_{VA}^{Z-Z} = -\alpha\pi\frac{g_V^{e-Z}g_A^{q-Z}}{(T-m_Z^2)^2}(\delta m_Z^2+\delta Z_{ZZ}(m_Z^2-T))\cdot(\overline{u}_e\gamma_\mu u_e)\,(\overline{u}_q\gamma_\mu\gamma_5 u_q)\,, \tag{171}$$

and the axial-vector part

$$\delta\mathcal{M}_{AV}^{Z-Z} = -\alpha\pi\frac{g_A^{e-Z}g_V^{q-Z}}{(T-m_Z^2)^2}(\delta m_Z^2+\delta Z_{ZZ}(m_Z^2-T))\cdot(\overline{u}_e\gamma_\mu\gamma_5 u_e)\,(\overline{u}_q\gamma_\mu u_q)\,. \tag{172}$$

Field and mass renormalization constants are determined from on-shell renormalization conditions:

$$Re\left[\hat{\sum}_{ZZ}\left(q^2 = m_Z^2\right)\right] = 0, \tag{173}$$

$$\frac{\partial}{\partial q^2} Re\left[\hat{\sum}_{ZZ}\left(q^2 = m_Z^2\right)\right] = 0. \tag{174}$$

Here, $\hat{\sum}$ represents the renormalized truncated self-energy graph, which is equal to

$$\hat{\sum}_{ZZ}\left(q^2\right) = \sum_{ZZ}^{\perp}\left(q^2\right) - \delta m_Z^2 + \delta Z_{ZZ}(q^2 - m_Z^2), \tag{175}$$

where $\sum^{\perp}(q^2)$ is the unrenormalized transverse part of the self-energy graph.

As one can see, Eq.(173) defines the renormalization constant for the Z mass as

$$\delta m_Z^2 = Re\left[\sum_{ZZ}^{\perp}\left(q^2 = m_Z^2\right)\right], \tag{176}$$

and for Z field renormalization we have used Eq.(174):

$$\frac{\partial}{\partial q^2} Re\left[\hat{\sum}_{ZZ}\left(q^2 = m_Z^2\right)\right] = \frac{\partial}{\partial q^2} Re\left[\sum_{ZZ}^{\perp}\left(q^2 = m_Z^2\right)\right] + \delta Z_{ZZ} = 0. \tag{177}$$

Applying the above renormalization conditions, we have the following renormalization constants for the self-energy graphs:

fermions in the loop: (all couplings between fermions and the Z boson have been expanded)

$$\delta m_Z^2 = \frac{\alpha}{24\pi\, s_W^2\, c_W^2} Re[((8\, s_W^4 - 4 s_W^2 + 1)\sum_{i=1}^{3}(-3\, A_0(m_{l_i}^2) +$$

$$6B_{00}(m_Z^2, m_{l_i}^2, m_{l_i}^2) - 3m_Z^2\ B_1(m_Z^2, m_{l_i}^2, m_{l_i}^2)) + (8\,s_W^4 - 12s_W^2 + 9)\cdot$$

$$\sum_{i=1}^{3}(-\,A_0(m_{q_i^{down}}^2) + 2B_{00}(m_Z^2, m_{q_i^{down}}^2, m_{q_i^{down}}^2) - m_Z^2\,B_1(m_Z^2, m_{q_i^{down}}^2, m_{q_i^{down}}^2))+$$

$$(32\,s_W^4 - 24s_W^2 + 9)\sum_{i=1}^{3}(-A_0(m_{q_i^{up}}^2) + 2B_{00}(m_Z^2, m_{q_i^{up}}^2, m_{q_i^{up}}^2)- \tag{178}$$

$$m_Z^2\,B_1(m_Z^2, m_{q_i^{up}}^2, m_{q_i^{up}}^2)) - 3\sum_{i=1}^{9} N_C^{f_i}\ m_{f_i}^2\,B_0(m_Z^2, m_{f_i}^2, m_{f_i}^2) + 18\,B_{00}(m_Z^2, 0, 0)-$$

$$9m_Z^2\,B_1(m_Z^2, 0, 0))]$$

and

$$\delta Z_{ZZ} = \frac{\alpha}{24\pi\,s_W^2\,c_W^2} Re[((8\,s_W^4 - 4s_W^2 + 1)\sum_{i=1}^{3}(3\,B_1(m_Z^2, m_{l_i}^2, m_{l_i}^2)-$$

$$6\,D[B_{00}(m_Z^2, m_{l_i}^2, m_{l_i}^2)] + 3m_Z^2\ D[B_1(m_Z^2, m_{l_i}^2, m_{l_i}^2)]) + (8\,s_W^4 - 12s_W^2 + 9)\cdot$$

$$\sum_{i=1}^{3}(B_1(m_Z^2, m_{q_i^{down}}^2, m_{q_i^{down}}^2) - 2D[B_{00}(m_Z^2, m_{q_i^{down}}^2, m_{q_i^{down}}^2)]+$$

$$m_Z^2 D[\,B_1(m_Z^2, m_{q_i^{down}}^2, m_{q_i^{down}}^2)]) + (32\,s_W^4 - 24s_W^2 + 9)\sum_{i=1}^{3}(B_1(m_Z^2, m_{q_i^{up}}^2, m_{q_i^{up}}^2)- \tag{179}$$

$$2D[B_{00}(m_Z^2, m_{q_i^{up}}^2, m_{q_i^{up}}^2)] + m_Z^2\, D[B_1(m_Z^2, m_{q_i^{up}}^2, m_{q_i^{up}}^2)])+$$

$$3\sum_{i=1}^{9} N_C^{f_i}\; m_{f_i}^2\, D[B_0(m_Z^2, m_{f_i}^2, m_{f_i}^2)] + 9\, B_1(m_Z^2, 0, 0) - 18\, D[B_{00}(m_Z^2, 0, 0)]+$$

$$9m_Z^2\, D[B_1(m_Z^2, 0, 0)])]$$

Here $m_{l_i}^2$, $m_{q_i^{up}}^2$ and $m_{q_i^{down}}^2$ are masses of massive leptons, "up", and "down" types of the quarks, respectively, and $D[B_{ij}(m_x^2, m_y^2, m_z^2)] \equiv \frac{\partial}{\partial q^2} B_{ij}(q^2, m_y^2, m_z^2)|_{q^2=m_x^2}$.

If only the bosons appear in the loops, the above renormalization constants have the structure:

bosons in the loops:

$$\delta m_Z^2 = \frac{\alpha}{16\pi\, s_W^2\, c_W^4} Re[(-(8m_W^2 + 20m_Z^2)c_W^6 + 8m_W^2\; s_W^4\, c_W^2\,)B_0(m_Z^2, m_W^2, m_W^2)+$$

$$+4m_W^2\, B_0(m_Z^2, m_H^2, m_Z^2) + (-36\, c_W^6 + 8s_W^2\, c_W^4 - 4s_W^4\, c_W^2)B_{00}(m_Z^2, m_W^2, m_W^2)- \tag{180}$$

$$4c_W^2\, B_{00}(m_Z^2, m_H^2, m_Z^2) - 8m_Z^2\, c_W^6\, B_1(m_Z^2, m_W^2, m_W^2) + c_W^2\, (A_0(m_H^2) + A_0(m_Z^2))$$

$$2(9c_W^4 - 2s_W^2\, c_W^2 + s_W^4)\, c_W^2\, A_0(m_W^2)] \quad ,$$

and

$$\delta Z_{ZZ} = \frac{\alpha}{4\pi\, s_W^2\, c_W^4} Re[((2m_W^2 + 5m_Z^2)c_W^6 - 2m_W^2\ s_W^4\, c_W^2\,) D[B_0(m_Z^2, m_W^2, m_W^2)] -$$

$$m_W^2\, D[B_0(m_Z^2, m_H^2, m_Z^2)] + (9\, c_W^6 - 2s_W^2\, c_W^4 + s_W^4\, c_W^2) D[B_{00}(m_Z^2, m_W^2, m_W^2)] + \tag{181}$$

$$c_W^2\, D[B_{00}(m_Z^2, m_H^2, m_Z^2)] + 2m_Z^2\, c_W^6 D[\, B_1(m_Z^2, m_W^2, m_W^2)] + c_W^6\ (5B_0(m_Z^2, m_W^2, m_W^2) +$$

$$2B_1(m_Z^2, m_W^2, m_W^2)] \quad .$$

4.2.5 Self-Energy: $\{Z - \gamma\}$ Graphs

As always, we start from the integral form of the amplitude, which in the $\{Z - \gamma\}$ mixing diagram case is constructed as

$$\mathcal{M}^{\gamma - Z} = -\frac{ie^4}{16\pi^4} \sum_{i=1}^{9} N_C^{f_i} \int d^4q \cdot (\overline{u}\,(k_1, m_e)\, \gamma^\nu\, g^{e-\gamma}\, u\,(p_1, m_e) \cdot$$

$$\overline{u}\,(k_2, m_q)\, \gamma^\mu \left(g_L^{q-Z} \varpi_- + g_R^{q-Z} \varpi_+\right) u\,(p_2, m_q) \cdot \mathrm{Tr}[\frac{m_{f_i} - \not{q}}{q^2 - m_{f_i}^2} \gamma^\alpha \left(g_L^{f_i - Z} \varpi_- + g_R^{f_i - Z} \varpi_+\right) \cdot \tag{182}$$

$$\frac{m_{f_i}+\not{k}_2-\not{q}-\not{p}_2}{(k_2-q-p_2)^2-m_{f_i}^2}\gamma^\beta\, g^{f_i-\gamma}\,]+\overline{u}\,(k_1,m_e)\,\gamma^\nu\left(g_L^{e-Z}\varpi_-+g_R^{e-Z}\varpi_+\right)u\,(p_1,m_e)\cdot$$

$$\overline{u}\,(k_2,m_q)\,\gamma^\mu\, g^{q-\gamma}\,u\,(p_2,m_q)\cdot \mathrm{Tr}[\frac{m_{f_i}-\not{q}}{q^2-m_{f_i}^2}\gamma^\alpha\, g^{f_i-\gamma}\cdot$$

$$\frac{m_{f_i}+\not{k}_2-\not{q}-\not{p}_2}{(k_2-q-p_2)^2-m_{f_i}^2}\gamma^\beta\left(g_L^{f_i-Z}\varpi_-+g_R^{f_i-Z}\varpi_+\right)])\frac{g_{\nu\beta}}{(p_2-k_2)^2-m_Z^2}\frac{g_{\mu\alpha}}{(k_2-p_2)^2}\quad . \tag{183}$$

Again, we consider fermions and bosons separately. For fermions only in the loops, the evaluation gives

$$\mathcal{M}^{\gamma-Z}_{VA(fermion)} = \frac{\alpha^2 g^{e-\gamma}g_A^{q-Z}}{T\,(T-m_Z^2)}\sum_{i=1}^{9}N_C^{f_i}\; g^{f_i-\gamma}\,g_V^{f_i-Z}\left(\begin{array}{c} A_0(m_{f_i}^2)-2B_{00}(T,m_{f_i}^2,m_{f_i}^2)+ \\ \\ +T\cdot B_1(T,m_{f_i}^2,m_{f_i}^2)\end{array}\right)\cdot \tag{184}$$

$$\cdot\,(\overline{u}_e\gamma_\mu u_e)\,(\overline{u}_q\gamma_\mu\gamma_5 u_q)$$

and

$$\mathcal{M}^{\gamma-Z}_{AV(fermion)} = \frac{\alpha^2 g^{q-\gamma}g_A^{e-Z}}{T\,(T-m_Z^2)}\sum_{i=1}^{9}N_C^{f_i}\; g^{f_i-\gamma}\,g_V^{f_i-Z}\left(\begin{array}{c} A_0(m_{f_i}^2)-2B_{00}(T,m_{f_i}^2,m_{f_i}^2)+ \\ \\ +T\cdot B_1(T,m_{f_i}^2,m_{f_i}^2)\end{array}\right)\cdot \tag{185}$$

$$\cdot \left(\overline{u}_e \gamma_\mu \gamma_5 u_e\right) \left(\overline{u}_q \gamma_\mu u_q\right) .$$

Here, we are summing over all possible fermions in the loop except for neutrinos (neutrinos do not couple to photons). When only vector, scalar and unitary bosons appear in the loop, the vector-axial part of the $\{\gamma - Z\}$ mixing amplitude is given by

$$\mathcal{M}^{\gamma-Z}_{VA(boson)} = \frac{\alpha^2}{2 s_W \; c_W} \frac{g^{e-\gamma}}{T\,(T - m_Z^2)} [(g_A^{q-Z} + 6\, g_V^{q-Z} c_W^2) A_0(m_W^2) + \tag{186}$$

$$g_A^{q-Z}((2m_W^2 + 5\, c_W^2\, T) B_0(T, m_W^2, m_W^2) + 2\,((5\, c_W^2 - s_W^2)\, B_{00}(T, m_W^2, m_W^2) +$$

$$c_W^2\, T \cdot B_1(T, m_W^2, m_W^2)))] \cdot \left(\overline{u}_e \gamma_\mu u_e\right) \left(\overline{u}_q \gamma_\mu \gamma_5 u_q\right) \quad ,$$

and the axial-vector part is given by:

$$\mathcal{M}^{\gamma-Z}_{AV(boson)} = -\frac{\alpha^2}{4 s_W \; c_W} \frac{g^{q-\gamma}}{T\,(T - m_Z^2)} [2 g_A^{e-Z} (5\, c_W^2 - s_W^2) A_0(m_W^2) - \tag{187}$$

$$2\, g_A^{e-Z} (2m_W^2 + 5\, c_W^2\, T)\, B_0(T, m_W^2, m_W^2) +$$

$$((g_A^{e-Z} + g_V^{e-Z})\, c_W - (21 g_A^{e-Z} + g_V^{e-Z})\, c_W^2 + 4 g_A^{e-Z}\, s_W^2)\, B_{00}(T, m_W^2, m_W^2) -$$

$$4 g_A^{e-Z}\, c_W^2\; T \cdot B_1(T, m_W^2, m_W^2)] \cdot \left(\overline{u}_e \gamma_\mu \gamma_5 u_e\right) \left(\overline{u}_q \gamma_\mu u_q\right) \quad .$$

Counterterms: $\{\gamma - Z\}$ mixing case. Counterterms derived from the $\{\gamma - Z\}$ mixing part of the Lagrangian contain only the $\gamma - Z$ mixing field renormalization constants. The parity violating part of the counterterm reads explicitly

$$\begin{aligned}
\delta\mathcal{M}_{VA}^{\gamma-Z} &= -\frac{\alpha\,\pi\, g_A^{q-Z} g^{e-\gamma}}{T\left(T-m_Z^2\right)}(\delta Z_{Z\gamma}(m_Z^2-T)-\delta Z_{\gamma Z}T)\cdot\left(\overline{u}_e\gamma_\mu u_e\right)\left(\overline{u}_q\gamma_\mu\gamma_5 u_q\right), \\
\delta\mathcal{M}_{AV}^{\gamma-Z} &= -\frac{\alpha\,\pi\, g_A^{e-Z} g^{q-\gamma}}{T\left(T-m_Z^2\right)}(\delta Z_{Z\gamma}(m_Z^2-T)-\delta Z_{\gamma Z}T)\cdot\left(\overline{u}_e\gamma_\mu\gamma_5 u_e\right)\left(\overline{u}_q\gamma_\mu u_q\right).
\end{aligned} \tag{188}$$

Renormalization constants $\delta Z_{Z\gamma}$ and $\delta Z_{\gamma Z}$ can be determined from the on-shell renormalization conditions:

$$\begin{aligned}
Re\left[\Gamma_{\gamma Z}^{\mu\nu}\left(q^2\right)\varepsilon_\nu\left(k\right)\right] \;\;|\;\; {}_{q^2=m_Z^2} &= 0, \\
Re\left[\Gamma_{\gamma Z}^{\mu\nu}\left(q^2\right)\varepsilon_\nu\left(k\right)\right] \;\;|\;\; {}_{q^2=0} &= 0,
\end{aligned} \tag{189}$$

implying that there is no $\gamma-Z$ mixing at the Z pole. Here, $\Gamma_{\gamma Z}^{\mu\nu}\left(q^2\right)$ is the truncated $\gamma-Z$ mixing self-energy renormalized graph. From the above renormalization conditions and the structure of the counterterm, it easy to see that

$$\begin{aligned}
\delta Z_{Z\gamma} &= 2\,Re\left[\frac{\sum_{\gamma Z}^{\perp}\left(q^2=0\right)}{m_Z^2}\right], \\
\delta Z_{\gamma Z} &= -2\,Re\left[\frac{\sum_{\gamma Z}^{\perp}\left(q^2=m_Z^2\right)}{m_Z^2}\right].
\end{aligned} \tag{190}$$

Explicit expressions for $\gamma - Z$ mixing renormalization constants come from self-energy graphs at $q^2 = 0$ and $q^2 = m_Z^2$. Although the $\gamma - Z$ mixing term of the parity violating amplitude was split into terms corresponding to fermions or bosons only in the loop, for counterterm renormalization constants we will include all of the particles in the loop:

$$\delta Z_{\gamma Z} = \frac{\alpha}{6\, c_W\, s_W\, \pi\, m_Z^2} Re[(4\, s_W^2 - 1) \sum_{i=1}^{3} (3A_0(m_{l_i}^2) - 6B_{00}(m_Z^2, m_{l_i}^2, m_{l_i}^2) +$$

$$3m_Z^2\, B_1(m_Z^2, m_{l_i}^2, m_{l_i}^2)) + (4\, s_W^2 - 3) \sum_{i=1}^{3} (A_0(m_{q_i^{down}}^2) - 2B_{00}(m_Z^2, m_{q_i^{down}}^2, m_{q_i^{down}}^2) +$$

(191)

$$m_Z^2 B_1(m_Z^2, m_{q_i^{down}}^2, m_{q_i^{down}}^2)) + (8\, s_W^2 - 3) \sum_{i=1}^{3} (2\, A_0(m_{q_i^{up}}^2) - 4B_{00}(m_Z^2, m_{q_i^{up}}^2, m_{q_i^{up}}^2) +$$

$$2m_Z^2 B_1(m_Z^2, m_{q_i^{up}}^2, m_{q_i^{up}}^2)) + (5\, c_W^2 - s_W^2)(3A_0(m_W^2) - 6B_{00}(m_Z^2, m_W^2, m_W^2)) -$$

$$3(2m_W^2 + 5c_W^2\, m_Z^2) B_0(m_Z^2, m_W^2, m_W^2) - 6\, c_W^2\; m_Z^2\, B_1(m_Z^2, m_W^2, m_W^2)] \quad ,$$

and

$$\delta Z_{Z\gamma} = -\frac{\alpha}{6\, c_W\, s_W\, \pi\, m_Z^2} Re[(4\, s_W^2 - 1) \sum_{i=1}^{3} (3A_0(m_{l_i}^2) - 6B_{00}(m_Z^2, m_{l_i}^2, m_{l_i}^2)) +$$

$$(4\, s_W^2 - 3) \sum_{i=1}^{3} (A_0(m_{q_i^{down}}^2) - 2B_{00}(m_Z^2, m_{q_i^{down}}^2, m_{q_i^{down}}^2)) +$$

(192)

$$(8\,s_W^2 - 3)\sum_{i=1}^{3}(2\,A_0(m_{q_i^{up}}^2) - 4B_{00}(m_Z^2, m_{q_i^{up}}^2, m_{q_i^{up}}^2))+$$

$$(5\,c_W^2 - s_W^2)(3A_0(m_W^2) - 6B_{00}(m_Z^2, m_W^2, m_W^2)) - \; 6m_W^2\,B_0(m_Z^2, m_W^2, m_W^2)] \quad .$$

By adding together term and counterterm parts of the parity-violating amplitude, we obtain the final result free of UV divergences.

4.2.6 Vertex corrections graphs

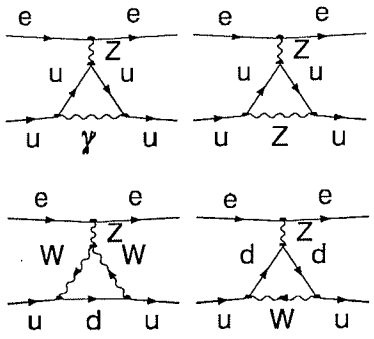

Figure 17: $\{Z - q\}$ vertex corrections (only vector bosons in the loop)

Generally, we have 146 vertex corrections graphs for electron and quark vertices all together, but the dominant contribution comes from only 21 graphs. The rest of the diagrams are needed to keep the total amplitude gauge invariant. As shown in Fig.(17), among $\{Z - q\}$ vertex corrections graphs, we will only consider those

with vector bosons in the loop. Note that "u" is an "up" type quark and "d" is a "down" type quark. This makes the presented amplitude not gauge invariant, but the numerical results are practically the same, agreeing with the gauge invariant version at level of a fraction of a percent.

The following notation has been adopted to keep the amplitude as short as possible

$$C_i\left(m^2_{q^{up}_j}, T, m^2_{q^{up}_j}, m^2_x, m^2_y, m^2_z\right) \equiv C_i\left(m^2_x, m^2_y, m^2_z\right) \tag{193}$$

along with following properties of three-point tensor coefficient functions:

$$C_1\left(m^2_W, m^2_{q^{down}_j}, m^2_{q^{down}_j}\right) = C_2\left(m^2_W, m^2_{q^{down}_j}, m^2_{q^{down}_j}\right) \tag{194}$$

$$C_1\left(m^2_{q^{down}_j}, m^2_W, m^2_W\right) = C_2\left(m^2_{q^{down}_j}, m^2_W, m^2_W\right)$$

$$C_1\left(m^2_Z, m^2_{q^{up}_j}, m^2_{q^{up}_j}\right) = C_2\left(m^2_Z, m^2_{q^{up}_j}, m^2_{q^{up}_j}\right)$$

$$C_1\left(0, m^2_{q^{up}_j}, m^2_{q^{up}_j}\right) = C_2\left(0, m^2_{q^{up}_j}, m^2_{q^{up}_j}\right)$$

Thus, for the set of diagrams on the Fig.(17), the vector-axial term is given by

$$\mathcal{M}^{q^{up}_i - Z}_{VA} = \frac{\alpha^2\, g_V^{e-Z}}{8\, s_W\, (T - m^2_Z)}[2\left(g_L^{q^{up}_i - W}\right)^2 (\sum_{j=1}^{3} |U_{ij}|^2\, [s_W\, ((g_A^{q^{down}_j - Z} - g_V^{q^{down}_j - Z}) \cdot$$

$$B_0(T, m^2_{q^{down}_j}, m^2_{q^{down}_j}) + (g_A^{q^{down}_j - Z}(m^2_{q^{down}_j} + m^2_{q^{up}_i} + m^2_W - T) +$$

$$g_V^{q_j^{down}-Z}(m^2_{q_j^{down}} - m^2_{q_i^{up}} - m^2_W + T))\, C_0(m^2_W, m^2_{q_j^{down}}, m^2_{q_j^{down}}) -$$

$$2(g_A^{q_j^{down}-Z} - g_V^{q_j^{down}-Z}) C_{00}(m^2_W, m^2_{q_j^{down}}, m^2_{q_j^{down}})) - 2\,\mathbf{i}\,(2\ c_W\ (m^2_{q_i^{up}} - T)\ \cdot$$

$$C_1(m^2_{q_j^{down}}, m^2_W, m^2_W) - \mathbf{i}\,(g_A^{q_j^{down}-Z} - g_V^{q_j^{down}-Z})\ s_W\ (T - 2\,m^2_{q_i^{up}})\cdot$$

$$C_1(m^2_W, m^2_{q_j^{down}}, m^2_{q_j^{down}}) + c_W\ (B_0(T, m^2_W, m^2_W) +$$

(195)

$$m^2_{q_j^{down}} C_0(m^2_{q_j^{down}}, m^2_W, m^2_W) + 2C_{00}(m^2_{q_j^{down}}, m^2_W, m^2_W))))]) +$$

$$g_A^{q_i^{up}-Z}\ s_W\ (\,4\left(g^{q_i^{up}-\gamma}\right)^2 (2m^2_{q_i^{up}} - T)\, C_0(0, m^2_{q_i^{up}}, m^2_{q_i^{up}}) -$$

$$8\left(g^{q_i^{up}-\gamma}\right)^2\ C_{00}(0, m^2_{q_i^{up}}, m^2_{q_i^{up}}) + 2((\left(g_A^{q_i^{up}-Z}\right)^2 + 3\left(g_V^{q_i^{up}-Z}\right)^2)\cdot$$

$$C_1(m^2_Z, m^2_{q_i^{up}}, m^2_{q_i^{up}}) + 4\left(g^{q_i^{up}-\gamma}\right)^2\ C_1(0, m^2_{q_i^{up}}, m^2_{q_i^{up}}))(2\,m^2_{q_i^{up}} - T)\ +$$

$$(\left(g_A^{q_i^{up}-Z}\right)^2 + 3\left(g_V^{q_i^{up}-Z}\right)^2 + 4\left(g^{q_i^{up}-\gamma}\right)^2) B_0(T, m^2_{q_i^{up}}, m^2_{q_i^{up}}) +$$

$$((2m_{q_i^{up}}^2 + m_Z^2 - T)\left(g_A^{q_i^{up}-Z}\right)^2 + (2m_{q_i^{up}}^2 + 3m_Z^2 - 3T)\left(g_V^{q_i^{up}-Z}\right)^2) \cdot$$

$$C_0(m_Z^2, m_{q_i^{up}}^2, m_{q_i^{up}}^2) - 2(\left(g_A^{q_i^{up}-Z}\right)^2 + 3\left(g_V^{q_i^{up}-Z}\right)^2) C_{00}(m_Z^2, m_{q_i^{up}}^2, m_{q_i^{up}}^2))] \cdot$$

$$\cdot (\overline{u}_e \gamma_\mu u_e)\,(\overline{u}_q \gamma_\mu \gamma_5 u_q)\,.$$

For the axial-vector part we have

$$\mathcal{M}_{AV}^{q_i^{up}-Z} = \frac{\alpha^2\, g_A^{e-Z}}{8\, s_W\, (T - m_Z^2)} [2\left(g_L^{q_i^{up}-W}\right)^2 (\sum_{j=1}^{3} |U_{ij}|^2\, [2\,\mathbf{i}\,((-2\,c_W\; C_1(m_{q_j^{down}}^2, m_W^2, m_W^2)$$

$$-\mathbf{i}\,(g_A^{q_j^{down}-Z} - g_V^{q_j^{down}-Z})\, s_W\; C_1(m_W^2, m_{q_j^{down}}^2, m_{q_j^{down}}^2))\,(T - 4\,m_{q_i^{up}}^2) +$$

$$c_W\; (B_0(T, m_W^2, m_W^2) + m_{q_j^{down}}^2 C_0(m_{q_j^{down}}^2, m_W^2, m_W^2) + 2C_{00}(m_{q_j^{down}}^2, m_W^2, m_W^2))) +$$

$$s_W\,((g_V^{q_j^{down}-Z} - g_A^{q_j^{down}-Z}) B_0(T, m_{q_j^{down}}^2, m_{q_j^{down}}^2) - (g_A^{q_j^{down}-Z} \begin{pmatrix} m_{q_j^{down}}^2 + 3m_{q_i^{up}}^2 + \\ \\ +m_W^2 - T \end{pmatrix}$$

$$+ g_V^{q_j^{down}-Z}\left(m_{q_j^{down}}^2 - 3m_{q_i^{up}}^2 - m_W^2 + T\right))\, C_0(m_W^2, m_{q_j^{down}}^2, m_{q_j^{down}}^2) +$$

$$2(g_A^{q_j^{down}-Z} - g_V^{q_j^{down}-Z})C_{00}(m_W^2, m_{q_j^{down}}^2, m_{q_j^{down}}^2))]) +$$

(196)

$$g_V^{q_i^{up}-Z}\, s_W\, (4\left(g^{q_i^{up}-\gamma}\right)^2 (2m_{q_i^{up}}^2 - T)\, C_0(0, m_{q_i^{up}}^2, m_{q_i^{up}}^2) -$$

$$8\left(g^{q_i^{up}-\gamma}\right)^2 C_{00}(0, m_{q_i^{up}}^2, m_{q_i^{up}}^2) + 2((\left(g_V^{q_i^{up}-Z}\right)^2 + 3\left(g_A^{q_i^{up}-Z}\right)^2) \cdot$$

$$C_1(m_Z^2, m_{q_i^{up}}^2, m_{q_i^{up}}^2) + 4\left(g^{q_i^{up}-\gamma}\right)^2 C_1(0, m_{q_i^{up}}^2, m_{q_i^{up}}^2))(4\, m_{q_i^{up}}^2 - T) +$$

$$(\left(g_V^{q_i^{up}-Z}\right)^2 + 3\left(g_A^{q_i^{up}-Z}\right)^2 + 4\left(g^{q_i^{up}-\gamma}\right)^2) B_0(T, m_{q_i^{up}}^2, m_{q_i^{up}}^2) +$$

$$((10m_{q_i^{up}}^2 + 3m_Z^2 - 3T)\left(g_A^{q_i^{up}-Z}\right)^2 + (2m_{q_i^{up}}^2 + m_Z^2 - T)\left(g_V^{q_i^{up}-Z}\right)^2) \cdot$$

$$C_0(m_Z^2, m_{q_i^{up}}^2, m_{q_i^{up}}^2) - 2(\left(g_V^{q_i^{up}-Z}\right)^2 + 3\left(g_A^{q_i^{up}-Z}\right)^2) C_{00}(m_Z^2, m_{q_i^{up}}^2, m_{q_i^{up}}^2))] \cdot$$

$$\cdot\, (\overline{u}_e \gamma_\mu \gamma_5 u_e)\, (\overline{u}_q \gamma_\mu u_q)\,.$$

Here, we have scattering of an electron on an "up"-type quark. To consider scattering of an electron on a "down" type quark, it is necessary to transpose the CKM matrix and replace "up" to "down" and "down" to "up" indices, correspondingly. This is

the only difference, so the amplitude has basically the same structure.

The above amplitudes are renormalized by the following counterterms:

$$\delta\mathcal{M}_{VA}^{q_i^{up}-Z} = -\frac{\mathbf{i}\,\alpha\,\pi\,g_V^{e-Z}}{12\,c_W^3\,s_W^3\,(T-m_Z^2)}(6\,s_W\;\delta s_W\,(1-2\,s_W^2) - 3\,c_W^2\,s_W^2\,(2\,\delta e + \delta Z_{ZZ}) + \tag{197}$$

$$2c_W^2\,s_W^2\;((4\,s_W^2-3)\;Re[\delta\,f_L^{(up)}] - 4\,s_W^2 Re[\delta\,f_R^{(up)}])) \cdot (\overline{u}_e\gamma_\mu u_e)\,(\overline{u}_q\gamma_\mu\gamma_5 u_q)\,,$$

$$\delta\mathcal{M}_{AV}^{q_i^{up}-Z} = \frac{\mathbf{i}\,\alpha\,\pi\,g_A^{e-Z}}{12\,c_W^3\,s_W^3\,(T-m_Z^2)}(2\,s_W\;\delta s_W\,(5\,s_W^2+3\,c_W^2) + c_W^2\,s_W^2\;\cdot \tag{198}$$

$$(8(2\,\delta e + \delta Z_{ZZ})\,s_W^2\; + 8\,c_W\;s_W\;\delta Z_{\gamma Z} - 3(2\,\delta e + \delta Z_{ZZ})) +$$

$$2c_W^2\,s_W^2\;((4\,s_W^2-3)\;Re[\delta\,f_L^{(up)}] + 4\,s_W^2 Re[\delta\,f_R^{(up)}])) \cdot (\overline{u}_e\gamma_\mu\gamma_5 u_e)\,(\overline{u}_q\gamma_\mu u_q)\,.$$

For the electron -"down" type quark scattering, the counterterms are

$$\delta\mathcal{M}_{VA}^{q_i^{down}-Z} = \frac{\mathbf{i}\,\alpha\,\pi\,g_V^{e-Z}}{12\,c_W^3\,s_W^3\,(T-m_Z^2)}(6\,s_W\;\delta s_W\,(1-2\,s_W^2) - 3\,c_W^2\,s_W^2\,(2\,\delta e + \delta Z_{ZZ}) + \tag{199}$$

$$2c_W^2\,s_W^2\;((2\,s_W^2-3)\;Re[\delta\,f_L^{(down)}] - 2\,s_W^2 Re[\delta\,f_R^{(down)}])) \cdot (\overline{u}_e\gamma_\mu u_e)\,(\overline{u}_q\gamma_\mu\gamma_5 u_q)\,,$$

$$\delta\mathcal{M}_{AV}^{q_i^{down}-Z} = -\frac{\mathbf{i}\,\alpha\,\pi\,g_A^{e-Z}}{12\,c_W^3\,s_W^3\,(T-m_Z^2)}(2\,s_W\;\delta s_W\,(\,s_W^2+3\,c_W^2) + c_W^2\,s_W^2\;\cdot$$

(200)

$$(4(2\,\delta e + \delta Z_{ZZ})\,s_W^2 + 4\,c_W\;s_W\;\delta Z_{\gamma Z} - 3(2\,\delta e + \delta Z_{ZZ})) +$$

$$2c_W^2\,s_W^2\;((2\,s_W^2 - 3)\;Re[\delta\,f_L^{(down)}] + 2\,s_W^2 Re[\delta\,f_R^{(down)}])) \cdot (\overline{u}_e\gamma_\mu\gamma_5 u_e)\,(\overline{u}_q\gamma_\mu u_q)\,.$$

Here, δe is the charge renormalization constant which was defined earlier in this work (see Eq. (124)). Renormalization constants δZ_{ZZ}, δs_W and $\delta Z_{\gamma Z}$ have also been calculated earlier. As for the renormalization constants of quark field $\delta\,f_{L,R}^{(up),(down)}$, we will give details at the end of this chapter.

Let us now consider the $\{\gamma - q\}$ vertex corrections for the parity violating amplitude as shown in Fig. (18). Seven particular $\{\gamma - q\}$ vertex correction graphs

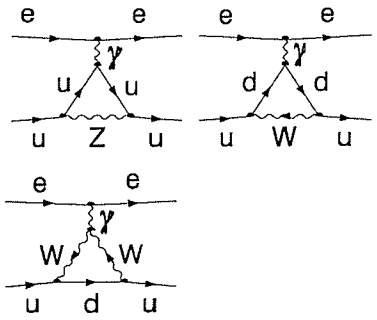

Figure 18: $\{\gamma - q\}$ vertex corrections graphs

contribute in total 95% of all the graphs of this type. Because the $\{e - \gamma\}$ vertex has only vector type coupling, the axial-vector part of the amplitude will be equal to

zero. Results for the vector-axial part of the amplitude are as follows:

$$\mathcal{M}_{VA}^{q_i^{up}-\gamma} = \frac{\alpha^2 g^{e-\gamma}}{T}(\left(g_L^{q_i^{up}-W}\right)^2 \sum_{j=1}^{3} |U_{ij}|^2 \,[(B_0(T, m_W^2, m_W^2) + m_{q_j^{down}}^2 C_0(m_{q_j^{down}}^2, m_W^2, m_W^2)$$

$$+2((C_1(m_{q_j^{down}}^2, m_W^2, m_W^2) + 2\mathbf{i}\, g^{q_j^{down}-\gamma} C_1(m_W^2, m_{q_j^{down}}^2, m_{q_j^{down}}^2))m_{q_i^{up}}^2 -$$

$$T\ (C_1(m_{q_j^{down}}^2, m_W^2, m_W^2) + \mathbf{i}\, g^{q_j^{down}-\gamma}\ C_1(m_W^2, m_{q_j^{down}}^2, m_{q_j^{down}}^2)) + \tag{201}$$

$$C_{00}(m_{q_j^{down}}^2, m_W^2, m_W^2)))\,\mathbf{i} - g^{q_j^{down}-\gamma}\,(B_0(T, m_{q_j^{down}}^2, m_{q_j^{down}}^2) +$$

$$(m_{q_i^{up}}^2 - m_{q_j^{down}}^2 + m_W^2 - T)C_0(m_W^2, m_{q_j^{down}}^2, m_{q_j^{down}}^2) - 2C_{00}(m_W^2, m_{q_j^{down}}^2, m_{q_j^{down}}^2))]$$

$$+g_A^{q_i^{up}-Z}\, g_V^{q_i^{up}-Z}\, g^{q_i^{up}-\gamma}[2(\,2m_{q_i^{up}}^2 - T\,)C_1(m_Z^2, m_{q_i^{up}}^2, m_{q_i^{up}}^2) + B_0(T, m_{q_i^{up}}^2, m_{q_i^{up}}^2) +$$

$$(m_Z^2 - T)C_0(m_Z^2, m_{q_i^{up}}^2, m_{q_i^{up}}^2) - 2C_{00}(m_Z^2, m_{q_i^{up}}^2, m_{q_i^{up}}^2)]) \cdot (\overline{u}_e \gamma_\mu u_e)\,(\overline{u}_q \gamma_\mu \gamma_5 u_q)$$

To obtain the vector-axial amplitude for the electron -"down" type scattering, we follow the same procedure as in $\{Z - q\}$ vertex corrections case, i.e. replace "up" with "down" index and transpose the CKM matrix. For the counterterm corresponding to

the electron -"up" type quark scattering, we have:

$$\delta\mathcal{M}_{VA}^{q_i^{up}-\gamma} = \frac{\mathbf{i}\alpha\pi g^{e-\gamma}}{6\,c_W\,s_W\,\cdot T}(3\,\delta Z_{Z\gamma} + 8\,c_W\,s_W\;Re[\,\delta\,f_R^{(up)} - \delta\,f_L^{(up)}]) \cdot (\overline{u}_e\gamma_\mu u_e)\,(\overline{u}_q\gamma_\mu\gamma_5 u_q)\,, \tag{202}$$

and for electron-"down" type quark scattering:

$$\delta\mathcal{M}_{VA}^{q_i^{down}-\gamma} = -\frac{\mathbf{i}\alpha\pi g^{e-\gamma}}{6\,c_W\,s_W\,\cdot T}(3\,\delta Z_{Z\gamma}+4\,c_W\,s_W\;Re[\,\delta\,f_R^{(down)}-\delta\,f_L^{(down)}])\cdot(\overline{u}_e\gamma_\mu u_e)\,(\overline{u}_q\gamma_\mu\gamma_5 u_q)\,. \tag{203}$$

99% of $\{e-Z\}$ vertex corrections graphs can be represented by only four diagrams shown at Fig.(19). With the assumption that $m_e^2 \approx 0$, as it appears in the kinematical

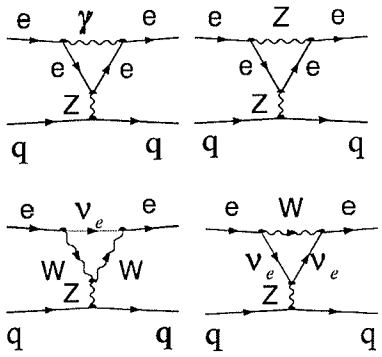

Figure 19: $\{e-Z\}$ vertex corrections graphs

coefficients, straightforward calculations show the following:

$$\mathcal{M}_{VA}^{e-Z} = \frac{\alpha^2 g_A^{q-Z}}{8\,s_W\,(T-m_Z^2)}[-4\mathbf{i}\,c_W\,\left(g_L^{e-W}\right)^2\,(B_0(T,m_W^2,m_W^2) + 2C_{00}(0,m_W^2,m_W^2))$$

$$+s_W\,[4\left(g_L^{e-W}\right)^2 g_L^{\nu_e-Z}(B_0(T,0,0)-2C_{00}(m_W^2,0,0)+m_W^2\,C_0(m_W^2,0,0))+$$

$$g_V^{e-Z}(-8\left(g^{e-\gamma}\right)^2 C_{00}(0,m_e^2,m_e^2)+(3\left(g_A^{e-Z}\right)^2+4\left(g^{e-\gamma}\right)^2+\left(g_V^{e-Z}\right)^2)\cdot$$

$$B_0(T,m_e^2,m_e^2)-(3\left(g_A^{e-Z}\right)^2+\left(g_V^{e-Z}\right)^2)\begin{pmatrix} 2C_{00}(m_Z^2,m_e^2,m_e^2)- \\ \\ -m_Z^2\,C_0(m_W^2,m_e^2,m_e^2) \end{pmatrix})]$$

$$-T(4\left(g_L^{e-W}\right)^2(g_L^{\nu_e-Z}s_W\,(C_0(m_W^2,0,0)+2C_1(m_W^2,0,0))-2\mathbf{i}\,c_W\,C_1(0,m_W^2,m_W^2)) \tag{204}$$

$$+g_V^{e-Z}\,s_W\,(4\left(g^{e-\gamma}\right)^2(C_0(0,m_e^2,m_e^2)+2C_1(0,m_e^2,m_e^2))+(C_0(m_Z^2,m_e^2,m_e^2)+$$

$$2C_1(m_Z^2,m_e^2,m_e^2))(3\left(g_A^{e-Z}\right)^2+\left(g_V^{e-Z}\right)^2))))]\cdot(\overline{u}_e\gamma_\mu u_e)\,(\overline{u}_q\gamma_\mu\gamma_5 u_q)\,,$$

and

$$\mathcal{M}_{AV}^{e-Z}=\frac{\alpha^2 g_V^{q-Z}}{8\,s_W\,(T-m_Z^2)}[4\mathbf{i}\,c_W\,\left(g_L^{e-W}\right)^2(B_0(T,m_W^2,m_W^2)+2C_{00}(0,m_W^2,m_W^2))$$

$$+s_W\,[-4\left(g_L^{e-W}\right)^2 g_L^{\nu_e-Z}(B_0(T,0,0)-2C_{00}(m_W^2,0,0)+m_W^2\,C_0(m_W^2,0,0))+ \tag{205}$$

$$g_A^{e-Z}(-8\left(g^{e-\gamma}\right)^2 C_{00}(0,m_e^2,m_e^2)+((\left(g_A^{e-Z}\right)^2+4\left(g^{e-\gamma}\right)^2+3\left(g_V^{e-Z}\right)^2)\cdot$$

$$B_0(T,m_e^2,m_e^2)-((g_A^{e-Z})^2+3\,(g_V^{e-Z})^2)\left(\begin{array}{c}2C_{00}(m_Z^2,m_e^2,m_e^2)-\\ \\ -m_Z^2\,C_0(m_W^2,m_e^2,m_e^2)\end{array}\right)]$$

$$-T(4\,(g_L^{e-W})^2\,(g_L^{\nu_e-Z}s_W\,(C_0(m_W^2,0,0)+2C_1(m_W^2,0,0))-2\mathbf{i}\,c_W\,C_1(0,m_W^2,m_W^2))$$

$$+g_A^{e-Z}\,s_W\,(4\,(g^{e-\gamma})^2\,(C_0(0,m_e^2,m_e^2)+2C_1(0,m_e^2,m_e^2))+(C_0(m_Z^2,m_e^2,m_e^2)+$$

$$2C_1(m_Z^2,m_e^2,m_e^2))((g_A^{e-Z})^2+3\,(g_V^{e-Z})^2)))]\cdot(\overline{u}_e\gamma_\mu\gamma_5 u_e)\,(\overline{u}_q\gamma_\mu u_q)\,.$$

Counterterms for the electron vertex correction have been simplified as

$$\delta\mathcal{M}_{VA}^{e-Z}=-\frac{\mathbf{i}\alpha\,\pi\,g_A^{q-Z}}{4\,c_W^3\,s_W^2\,(T-m_Z^2)}[4\,c_W^3\;s_W^2\;\delta Z_{\gamma Z}+c_W^2\,(2\,\delta s_W+ \tag{206}$$

$$s_W\;(2\delta e+\delta Z_{ZZ}))+2s_W\;c_W^2\,((2\,s_W^2-1)Re[\delta f_L^{(e)}]+$$

$$2\,s_W^2\,Re[\delta f_R^{(e)}])+6\,s_W^2\;\delta s_W\,]\cdot(\overline{u}_e\gamma_\mu u_e)\,(\overline{u}_q\gamma_\mu\gamma_5 u_q)\,,$$

and

$$\delta\mathcal{M}_{AV}^{e-Z}=\frac{\mathbf{i}\alpha\,\pi\,g_V^{q-Z}}{4\,c_W^3\,s_W^2\,(T-m_Z^2)}[c_W^2\,(2\,\delta s_W-s_W\,(4s_W^2-1)(2\delta e+\delta Z_{ZZ}))+$$

(207)

$$2s_W\ c_W^2\left((2\,s_W^2-1)Re[\delta f_L^{(e)}]-2\,s_W^2\ Re[\delta f_R^{(e)}]\right)-2\ s_W^2\ \delta s_W\,]\cdot$$

$$\cdot\,(\overline{u}_e\gamma_\mu\gamma_5 u_e)\,(\overline{u}_q\gamma_\mu u_q)\,.$$

Now let us consider Fig.(20) representing the $\{e-\gamma\}$ vertex corrections. As one can

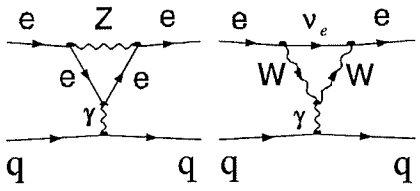

Figure 20: $\{e-\gamma\}$ vertex corrections diagrams

see, the $\{\gamma-q\}$ vertex has only the vector part of the coupling, so the vector-axial part of the PV amplitude is equal to zero. The resulting amplitude has a very simple form:

$$\mathcal{M}_{AV}^{e-\gamma}=\frac{\alpha^2 g^{q-\gamma}}{T}[-\mathbf{i}\,\left(g_L^{e-W}\right)^2(B_0(T,m_W^2,m_W^2)+2C_{00}(0,m_W^2,m_W^2)-$$

(208)

$$2T\,C_1(0,m_W^2,m_W^2)\,)+g_A^{e-Z}g^{e-\gamma}g_V^{e-Z}(B_0(T,m_e^2,m_e^2)-2C_{00}(m_Z^2,m_e^2,m_e^2)+$$

$$(m_Z^2\ -T\,)C_0(m_Z^2,m_e^2,m_e^2)-2T\,C_1(m_Z^2,m_e^2,m_e^2))]\cdot(\overline{u}_e\gamma_\mu\gamma_5 u_e)\,(\overline{u}_q\gamma_\mu u_q)$$

with the counterterm

$$\delta\mathcal{M}_{AV}^{e-\gamma} = -\frac{\mathbf{i}\alpha\pi\ g^{q-\gamma}}{2\,c_W\,s_W\,T}[\delta Z_{Z\gamma} + 4\,s_W\,c_W(Re[\delta f_R^{(e)}] - Re[\delta f_L^{(e)}])]\cdot(\overline{u}_e\gamma_\mu\gamma_5 u_e)\,(\overline{u}_q\gamma_\mu u_q)\,. \tag{209}$$

As the final step for this chapter, we are going to give some details on the fermion field renormalization constants $\delta f_{R,L}^{(e)}$ and $\delta f_{R,L}^{(up),(down)}$. Using expression Eq. (117) and expanding the fermion's truncated self-energy graphs, one can arrive at the following results:

$$\begin{aligned}
\delta f_R^{(e)} &= \frac{\alpha}{2\pi\,c_W^2}Re[c_W^2\ B_1(m_e^2,m_e^2,0) + s_W^2\,B_1(m_e^2,m_e^2,m_Z^2)], \\
\delta f_L^{(e)} &= \frac{\alpha}{8\pi\,c_W^2\,s_W^2}Re[\,(1-2\,s_W^2)\,B_1(m_e^2,m_e^2,m_Z^2) + 2\,c_W^2\,B_1(m_e^2,0,m_W^2) \\
&\qquad 4c_W^2\,s_W^2\ B_1(m_e^2,m_e^2,0)].
\end{aligned} \tag{210}$$

It should be noted here that the terms proportional to m_e^2 have been omitted from the above expressions.

For the quark field renormalization constants, we obtain

$$\delta f_R^{q_i^{up}} = \frac{\alpha}{72\,\pi\,c_W^2\,s_W^2}Re[16\,s_W^2\,(c_W^2\ B_1(m_{q_i^{up}}^2,m_{q_i^{up}}^2,0) + s_W^2\ B_1(m_{q_i^{up}}^2,m_{q_i^{up}}^2,m_Z^2)) -$$

$$-16\,s_W^2\,m_{q_i^{up}}^2((3-4s_W^2)DB_0(m_{q_i^{up}}^2,m_{q_i^{up}}^2,m_Z^2) - 4\,c_W^2\,DB_0(m_{q_i^{up}}^2,0,m_{q_i^{up}}^2)) +$$

(211)

$$m^2_{q_i^{up}}((3-4s^2_W)^2 DB_1(m^2_{q_i^{up}}, m^2_{q_i^{up}}, m^2_Z) + 32\, c^2_W\, s^2_W\, DB_1(m^2_{q_i^{up}}, m^2_{q_i^{up}}, 0) +$$

$$16\, s^4_W\, DB_1(m^2_{q_i^{up}}, m^2_{q_i^{up}}, m^2_Z) + 18\, c^2_W \sum_{j=1}^{3} |U_{ij}|^2\, DB_1(m^2_{q_i^{up}}, m^2_{q_j^{down}}, m^2_W)),$$

and

$$\delta f_R^{q_i^{down}} = \frac{\alpha}{72\,\pi\, c^2_W\, s^2_W} Re[4\, s^2_W\, (c^2_W\; B_1(m^2_{q_i^{down}}, m^2_{q_i^{down}}, 0) +$$

$$s^2_W\; B_1(m^2_{q_i^{down}}, m^2_{q_i^{down}}, m^2_Z)) - 8\, s^2_W\, m^2_{q_i^{down}}((3-4s^2_W) DB_0(m^2_{q_i^{down}}, m^2_{q_i^{down}}, m^2_Z) -$$

(212)

$$2\, c^2_W\, DB_0(m^2_{q_i^{down}}, 0, m^2_{q_i^{down}})) + m^2_{q_i^{down}}((3-4s^2_W)^2 DB_1(m^2_{q_i^{down}}, m^2_{q_i^{down}}, m^2_Z) +$$

$$+8\, c^2_W\, s^2_W\, DB_1(m^2_{q_i^{down}}, m^2_{q_i^{down}}, 0) + 4\, s^4_W\, DB_1(m^2_{q_i^{down}}, m^2_{q_i^{down}}, m^2_Z) +$$

$$18\, c^2_W \sum_{j=1}^{3} |U_{ji}|^2\, DB_1(m^2_{q_i^{down}}, m^2_{q_j^{up}}, m^2_W)).$$

Similarly, for the left handed quark field, we find:

$$\delta f_L^{q_i^{up}} = \frac{\alpha}{72\,\pi\, c^2_W\, s^2_W} Re[16\, s^2_W\, c^2_W\; B_1(m^2_{q_i^{up}}, m^2_{q_i^{up}}, 0) +$$

$$(3-4\, s^2_W)^2\; B_1(m^2_{q_i^{up}}, m^2_{q_i^{up}}, m^2_Z) - 16\, s^2_W\, m^2_{q_i^{up}}((3-4s^2_W) DB_0(m^2_{q_i^{up}}, m^2_{q_i^{up}}, m^2_Z) -$$

(213)

$$4\,c_W^2\,DB_0(m_{q_i^{up}}^2,0,m_{q_i^{up}}^2))+\ m_{q_i^{up}}^2((3-4s_W^2)^2DB_1(m_{q_i^{up}}^2,m_{q_i^{up}}^2,m_Z^2)+$$

$$32\,c_W^2\,s_W^2\,DB_1(m_{q_i^{up}}^2,m_{q_i^{up}}^2,0)+\ 16\,s_W^4\,DB_1(m_{q_i^{up}}^2,m_{q_i^{up}}^2,m_Z^2))+$$

$$18\,c_W^2\,\sum_{j=1}^{3}|U_{ij}|^2\,(B_1(m_{q_i^{up}}^2,m_{q_j^{down}}^2,m_W^2)+m_{q_i^{down}}^2\,DB_1(m_{q_i^{up}}^2,m_{q_j^{down}}^2,m_W^2)),$$

and

$$\delta f_L^{q_i^{down}}=\frac{\alpha}{72\,\pi\,c_W^2\,s_W^2}Re[4\,s_W^2\,c_W^2\ B_1(m_{q_i^{down}}^2,m_{q_i^{down}}^2,0)+$$

$$(3-2\,s_W^2)^2\ B_1(m_{q_i^{down}}^2,m_{q_i^{down}}^2,m_Z^2)-8\,s_W^2\,m_{q_i^{down}}^2((3-2s_W^2)\cdot$$

(214)

$$DB_0(m_{q_i^{down}}^2,m_{q_i^{down}}^2,m_Z^2)-\ 2\,c_W^2\,DB_0(m_{q_i^{down}}^2,0,m_{q_i^{down}}^2))+$$

$$m_{q_i^{down}}^2((3-2s_W^2)^2DB_1(m_{q_i^{down}}^2,m_{q_i^{down}}^2,m_Z^2)+$$

$$8\,c_W^2\,s_W^2\,DB_1(m_{q_i^{down}}^2,m_{q_i^{down}}^2,0)+\ 4\,s_W^4\,DB_1(m_{q_i^{down}}^2,m_{q_i^{down}}^2,m_Z^2))+$$

$$18\,c_W^2\,\sum_{j=1}^{3}|U_{ji}|^2\,(B_1(m_{q_i^{down}}^2,m_{q_j^{up}}^2,m_W^2)+m_{q_i^{down}}^2\,DB_1(m_{q_i^{down}}^2,m_{q_j^{up}}^2,m_W^2)).$$

5 Discussion and Analysis

The present research project is focused on extracting nucleon strange form factors from the measured asymmetry of the lepton-nucleon cross-sections, which requires evaluating radiative corrections to electro-weak scattering at the few percent level. Electroweak radiative corrections to intermediate energy, parity non-conserving semi-leptonic neutral current interactions have been addressed previously by Musolf and collaborators (see, for example, [45] and [57]). In these works, radiative corrections are constructed from the underlying fundamental weak interaction between electron and quarks. Broadly, such corrections are denoted as being either one-quark or many-quark effects. The one-quark corrections involve the interaction of the electron with a single quark. The many-quark contributions involve two or more quarks, and include effects due to an intrinsic weak interaction in the nucleon (e.g. the anapole moment).

As far as we know, one-loop processes involving the elementary particles of the Standard Model ("one-quark" type) give the dominant contribution to radiative corrections. Our primary aim is to considerably improve the precision for corrections involving only Standard Model constituents; and then move on to address many-body effects. These calculations should be performed for a variety of lepton-nucleon scattering experiments, in order to obtain the form factor values at different momentum transfers.

Evaluation of "one-quark" corrections with maximum precision requires renormal-

ization performed with careful inclusion of bremsstrahlung, and ensuring that any dependences on poorly constrained parameters of the Standard Model are analyzed and controlled. The new method of constrained differential renormalization was used. To calculate the radiative corrections at given momentum transfer and conserve gauge invariance, one needs to consider a full set of one-loop Feynman diagrams, which can include up to several hundreds of them, depending on particular scattering process. We have developed new methods and a software package to accomplish this task.

The partially computerized procedure we have developed allows performing an extensive analysis of the kinematical dependence and the dependence on all kinematic and Standard Model parameters. A set of two and three dimensional graphs was constructed, reproducing the dependence of all types of calculated radiative corrections (see Tables 6 and 7) on various kinematic variables and poorly-constrained SM parameters. In addition to helping to gain a better "feel" for the radiative correction behaviour, such analysis is essential for checking for irregular behavior (none was found), and accounting for the uncertainties of input parameters. Six graphs are selected to be presented here as the most illustrative: dependencies of total radiative correction $R_A^{T=1}$ and R_V^p on the electron scattering angle and beam energy in the lab frame, detector acceptance, unknown fraction of four dimensional momenta carried by quarks in the nucleon, and the not too well known masses of the top quark and Higgs boson. All six graphs are evaluated for kinematics appropriate for the SAMPLE

I experiment.

The total radiative corrections $R_A^{T=1}$ and R_V^p are large because the tree level amplitudes are suppressed by $(1-4\sin^2\theta_W)$. We have found only a weak dependence of the radiative corrections on scattering angle θ and electron energy $E_{\rm lab}$, as seen in Fig.(21 and Fig. (22), where $R_A^{T=1}$ is shown by dashed line and R_V^P by the solid one. In Fig. (22) we show the (logarithmic) dependence of R_V^p and $R_A^{T=1}$ on the the photon detection parameter ΔE.

In our single quark calculations, we have to account for the fraction of four dimensional momenta carried by quarks in the nucleon. Although some reasonable constraints can be imposed, this value is not known. However, it does not affect the precision of our calculations, since, in the region considered, the dependence of the corrections on this value is very weak (Fig.(24)).

In Fig.(25), the corrections show only a slight dependence on the Higgs mass M_H, which is quite fortunate, too, as the Higgs mass is not well known. As we can see from Fig.(26), radiative corrections appear to be highly sensitive to the mass of the top quark. This graph facilitates comparison with previous work [43], which used $m_t = 120$ MeV. This strong dependence on m_t arises from the large mass splitting within the top-bottom fermion doublet. The mass of the top quark is much better known now ($m_t = 174.3 \pm 5.1$ MeV according to [46]), so this value does not introduce any significant uncertainty into our evaluations. All of the numbers listed in Sections

4.1 ("Numerical Results") should be updated when a more precise value of top quark mass becomes available.

It is not easy to calculate uncertainties in a theoretical work, and only a limited discussion can be provided here. If we use the same renormalization scheme (CDR in this case), keep momentum dependence, but do not include the hard photon bremsstrahlung term, then the uncertainty introduced by the variation of the Standard Model parameters does not exceed one percent for the large axial-vector radiative corrections. Addition of the hard photon bremsstrahlung term may change them up to 10%. However, this discrepancy is still small comparing to the uncertainty in many-quark radiative effects (recall $R_A^{T=1} = -0.06 \pm 0.24$ from [57]) introduced by a large model dependence. Our results for the one-quark terms are consistent with results reported in the previous works [42, 43, 44, 45, 57], although the direct numerical term-by-term comparison is not particularly meaningful due to the significant difference in calculation methods used.

So far we have calculated the "one-quark" radiative corrections for electron-proton scattering for the specific kinematics of SAMPLE I and SAMPLE II (MIT-Bates) experiments, as well as the HAPPEX I and II, G0, A4 and Q_{weak} experiments at Jefferson Lab. Special attention was paid to including the proper combination of single-quark parameters corresponding to specific corrections for proton and neutron.

However, even after regulating IR divergences through soft-photon emission, the

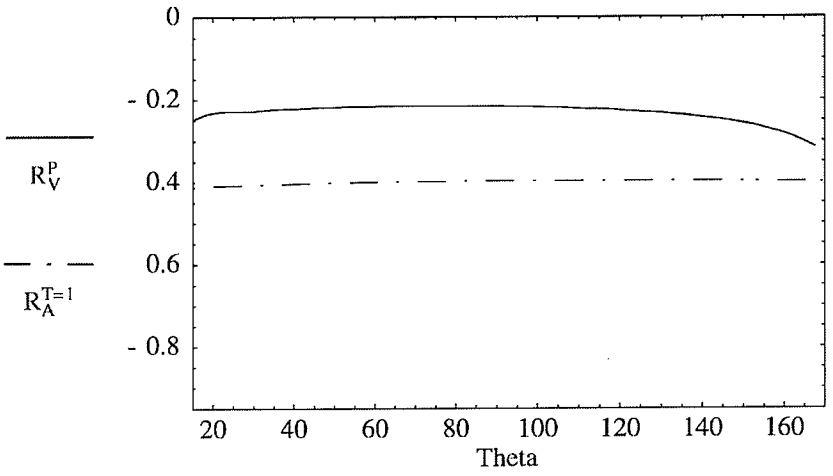

Figure 21: $R_A^{T=1}$ (dashed line) and R_V^P (solid line) as a function of the scattering angle (in degrees).

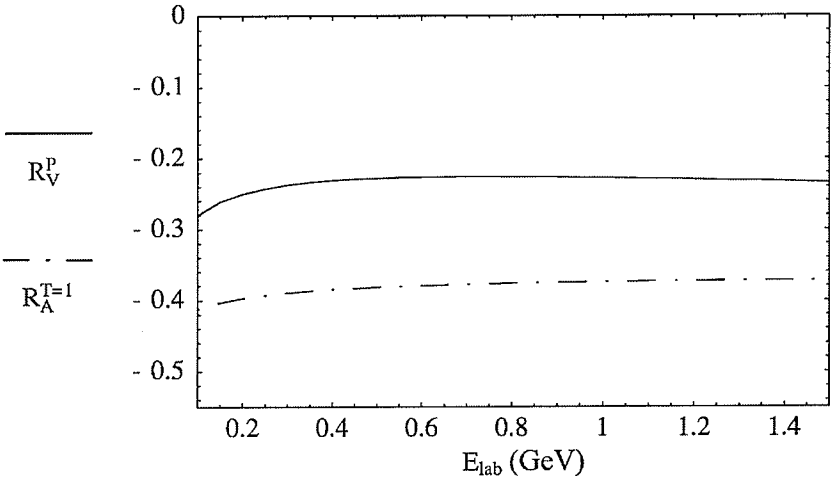

Figure 22: $R_A^{T=1}$ (dashed line) and R_V^P (solid line) as a function of the beam energy in laboratory frame E_{lab} (in GeV).

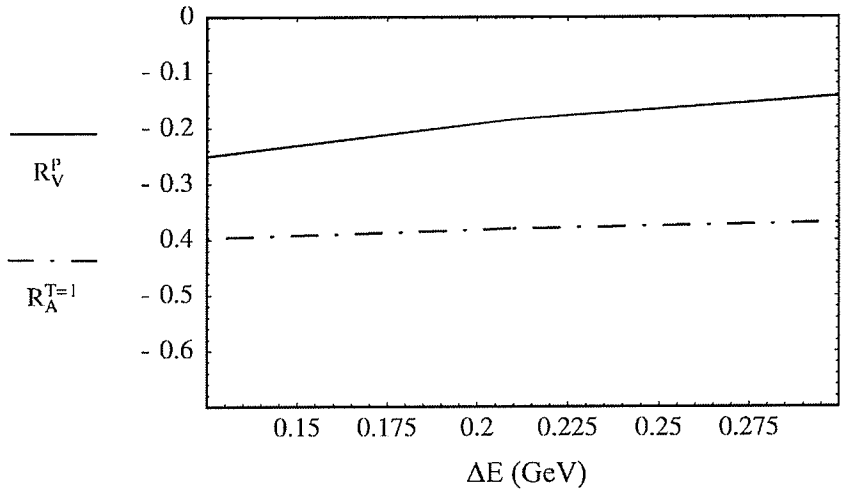

Figure 23: $R_A^{T=1}$ (dashed line) and R_V^P (solid line) as a function of the photon detection parameter ΔE (in MeV).

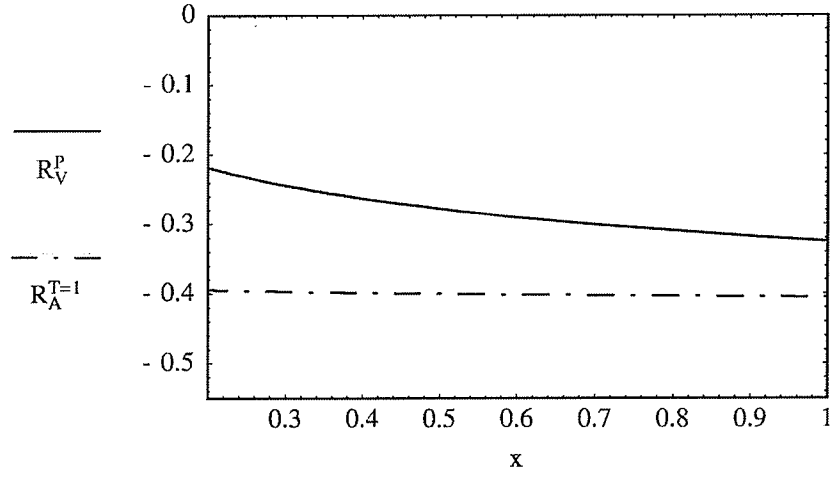

Figure 24: $R_A^{T=1}$ (dashed line) and R_V^P (solid line) as a function of the fraction of nucleon momentum carried by a quark.

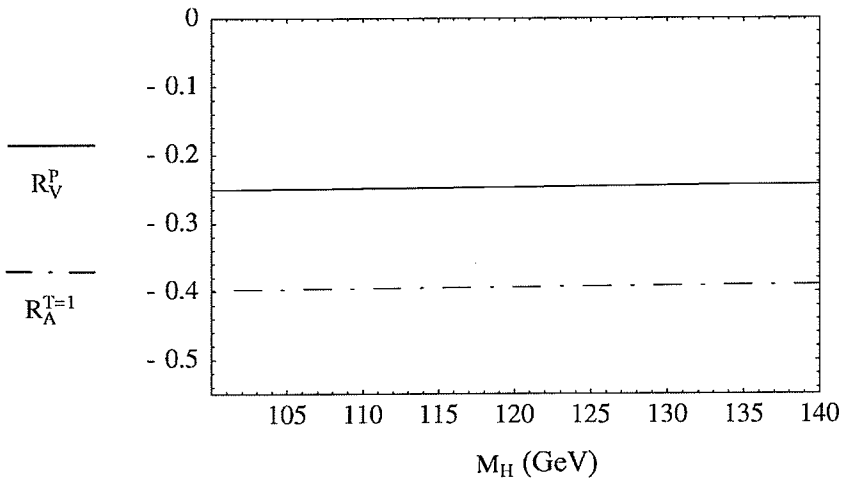

Figure 25: $R_A^{T=1}$ (dashed line) and R_V^P (solid line) as a function of the mass of the Higgs boson $M_{\rm H}$ (in GeV).

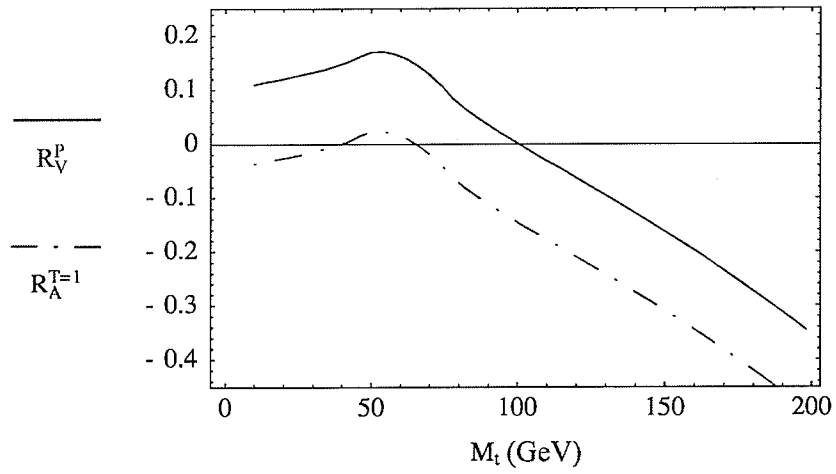

Figure 26: $R_A^{T=1}$ (dashed line) and R_V^P (solid line) as a function of the mass of the top quark (in GeV).

calculated one-quark radiative corrections showed a logarithmic dependence on the detector's photon acceptance parameter ΔE. Elimination of this dependence can be achieved by adding the hard photon bremsstrahlung (HPB) term. For one-quark radiative corrections, the HPB term is hard to account for due to the poorly known quark dynamics. In case of HPB computation for electron-proton scattering, we can avoid this problem by representing quark dynamics directly through an experimentally determined set of form factors.

Using the dipole approximation, we can modify general electro-weak couplings by inserting appropriate form factors into vertices and construct the HPB factor as a function of Mandelstam invariants. Taking into account experimental constraints, integration over the emitted photon phase space can be performed numerically. The first experiment on which we would like to try this for is Q_{weak}. Having considered the HPB factor purely for electron-proton scattering, we have to calculate radiative corrections and the soft photon factor with modified couplings for the set of IR divergent graphs (two vertex correction and four $\{\gamma - Z\}$ boxes) in order to achieve cancellation of IR divergences and ΔE dependence all together. $\{\gamma - Z\}$ box graphs have been estimated by [39] without momentum dependence in the Born part. We just completed a calculation for box graphs using the tensor decomposition technique without the zero momentum transfer approximation, and plan to include nucleonic delta resonances as well. Vertex correction graphs will have to be considered next.

To perform voluminous algebraic computation, our computational techniques already developed and tested for one-quark radiative corrections have to be expanded to allow inclusion of form factors into the vertices. It will be important to take into account up-to-date nucleon electric and magnetic form factors measured for appropriate momentum transfer by the University of Regina SPARRO group [13].

New experiments are under way or planned for the near future. The experimental techniques continue to be developed and improved, so they will require more precise contributions from theory. Some of the methods described in this work can be employed to provide theoretical input for these new experiments, extending calculations by including new types of corrections as needed.

It is worth noting here that one of the reasons for choosing the constrained differential renormalization (CDR) scheme for our calculations is that CDR can be easily expanded for the minimal super symmetric model (MSSM). Including SuperPartner particles is something we might have to consider in the future. In general, our calculation routines, tested for electron-quark scattering, are valid for any electroweak processes involving elementary particles of Standard Model, which means they might be helpful for neutrino scattering as well.

6 Appendix

6.1 Coupling Constants

At a generic level, for vertex $\{F - F - V_\mu\}$ we can write

$$\{F - F - V_\mu\} \rightarrow \overline{u}_F C\left(F, F, V_\mu\right) u_F, \tag{215}$$

where $C\left(F, F, V_\mu\right)$ is a generic coupling defined from the SM Lagrangian as

$$C\left(F, F, V_\mu\right) = \left(\begin{array}{cc} \gamma_\mu \varpi_- & \gamma_\mu \varpi_+ \end{array} \right) \overrightarrow{G}_{FFV} \tag{216}$$

where $\overrightarrow{G}_{FFV}$ is a coupling matrix containing couplings of the classes up to the desired counterterm order. In the case of one-loop calculations, we restrict coupling matrices up to the first counterterm order only (zero order- tree level, first order - one loop, etc.). We define five types of fermion - fermion - vector boson coupling matrix $\overrightarrow{G}_{FFV}$: $\overrightarrow{G}_{f,f,\gamma}$ (any fermions, photon), $\overrightarrow{G}_{f,f,Z}$ (any fermions, Z-boson), $\overrightarrow{G}_{l,l',W}$ (leptons only, charged W-boson), $\overrightarrow{G}_{q_i^{(up)},q_j^{(down)},W}$ (up and down type quarks only, W^--boson), and $\overrightarrow{G}_{q_i^{(down)},q_j^{(up)},W}$ (down and up type quarks only, W^+-boson).

Let us start with the coupling matrix $\overrightarrow{G}_{f,f,\gamma}$ (fermion-fermion-photon vertex):

$$\overrightarrow{G}_{f,f,\gamma} = ie \left(\begin{array}{cc} -Q_f & -Q_f(\delta e + \frac{\delta Z_{\gamma\gamma}}{2} + \mathrm{Re}[\delta f_L^f]) + g_L^{l-Z} \frac{\delta Z_{Z\gamma}}{2} \\ -Q_f & -Q_f(\delta e + \frac{\delta Z_{\gamma\gamma}}{2} + \mathrm{Re}[\delta f_R^f]) + g_R^{l-Z} \frac{\delta Z_{Z\gamma}}{2} \end{array} \right), \tag{217}$$

where the first column represents the tree level coupling and the second one, the one loop counter term. Furthermore, we give a list of the generic couplings for various

interactions, as well as coupling matrices up to the first order counterterm, where necessary.

The rest of the coupling matrices entering Eq. 216 have the following structure:

$$\overrightarrow{G}_{f,f,Z} = ie \begin{pmatrix} g_L^{f-Z} & g_L^{f-Z}\frac{\delta Z_{ZZ}}{2} + \delta g_L^{f-Z} - Q_f \frac{\delta Z_{\gamma Z}}{2} + g_L^{f-Z}\,\mathrm{Re}[\delta f_L^f] \\ g_R^{f-Z} & g_R^{f-Z}\frac{\delta Z_{ZZ}}{2} + \delta g_R^{f-Z} - Q_f \frac{\delta Z_{\gamma Z}}{2} + g_R^{f-Z}\,\mathrm{Re}[\delta f_R^f] \end{pmatrix}, \tag{218}$$

$$\overrightarrow{G}_{l,l',W} = ie \begin{pmatrix} \frac{1}{\sqrt{2}s_W} \\ 0 \end{pmatrix}, \tag{219}$$

$$\overrightarrow{G}_{q_i^{(up)},q_j^{(down)},W} = ie \begin{pmatrix} \frac{1}{\sqrt{2}s_W} U_{ij} \\ 0 \end{pmatrix}, \tag{220}$$

$$\overrightarrow{G}_{q_i^{(down)},q_j^{(up)},W} = ie \begin{pmatrix} \frac{1}{\sqrt{2}s_W} U_{ij}^* \\ 0 \end{pmatrix}. \tag{221}$$

Combining Eq. 216 with Eq. 217 and Eq. 218- Eq. 221, we obtain the couplings needed to construct vertex, boxes and self-energy graphs.

To construct counterterm amplitudes for self-energy graphs, the generic coupling for $C\left(V_\mu\left(k_1\right), V_\nu\left(k_2\right)\right)$ has been used:

$$C\left(V_\mu\left(k_1\right), V_\nu\left(k_2\right)\right) = \begin{pmatrix} -g_{\mu\nu}\left(k_1 k_2\right) & g_{\mu\nu} & -k_{1\mu}k_{2\nu} \end{pmatrix} \overrightarrow{G}_{VV}, \tag{222}$$

where

$$\overrightarrow{G}_{ZZ} = i \begin{pmatrix} 0 & \delta Z_{ZZ} \\ 0 & m_Z^2\, \delta Z_{ZZ} + \delta m_Z^2 \\ 0 & -\delta Z_{ZZ} \end{pmatrix}, \tag{223}$$

and

$$\overrightarrow{G}_{\gamma Z} = \frac{i}{2} \begin{pmatrix} 0 & \delta Z_{\gamma Z} + \delta Z_{Z\gamma} \\ 0 & m_Z^2\, \delta Z_{\gamma Z} \\ 0 & -\delta Z_{\gamma Z} - \delta Z_{Z\gamma} \end{pmatrix}. \tag{224}$$

6.2 Feynman Graphs Gallery

We choose to split all diagrams in three groups: boxes, self-energy loops and triangles. In a given group, each diagram has the number of the form T1 P2 N23 underneath. Here, T1 means "Topology 1", P2 corresponds to class insertion 2, and N23 is the running number in a given group. N runs from 1 to 44 for boxes, 1 to 262 for self-energy loops and 1 to 140 for triangles, which gives as a total of 446 one-loop graphs. Only 235 of them are parity-violating. It was found instructive to calculate a complete set of one-loop diagrams with all Standard Model elementary particles included because the full set gives us a possibility to perform such important self-checks as verifying gauge invariance.

For one-loop case, only two topologies are possible in each group:

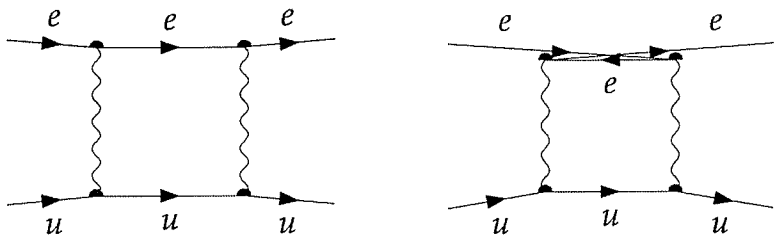

Box T1 and crossed box T2

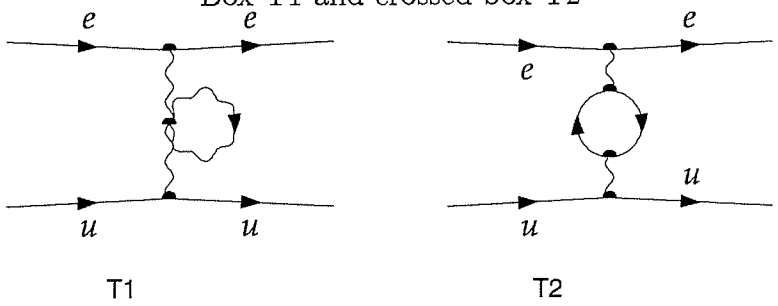

Self-energy T1 and vacuum polarization T2

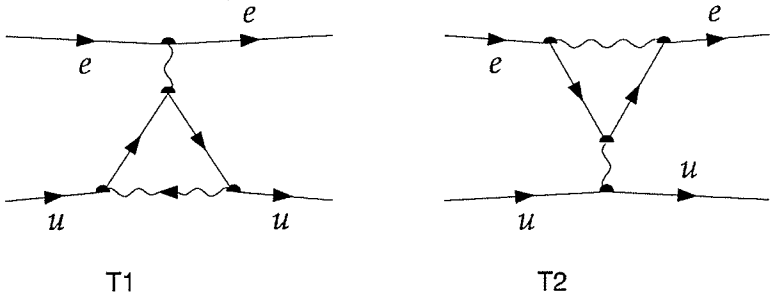

Triange base down T1 and base up T2

6.2.1 Boxes

6.2.2 Self-Energy

6.2.3 Self-Energy Counterterms

6.2.4 Triangles

6.2.5 Triangles Counterterms

$e \quad u \rightarrow e \quad u$

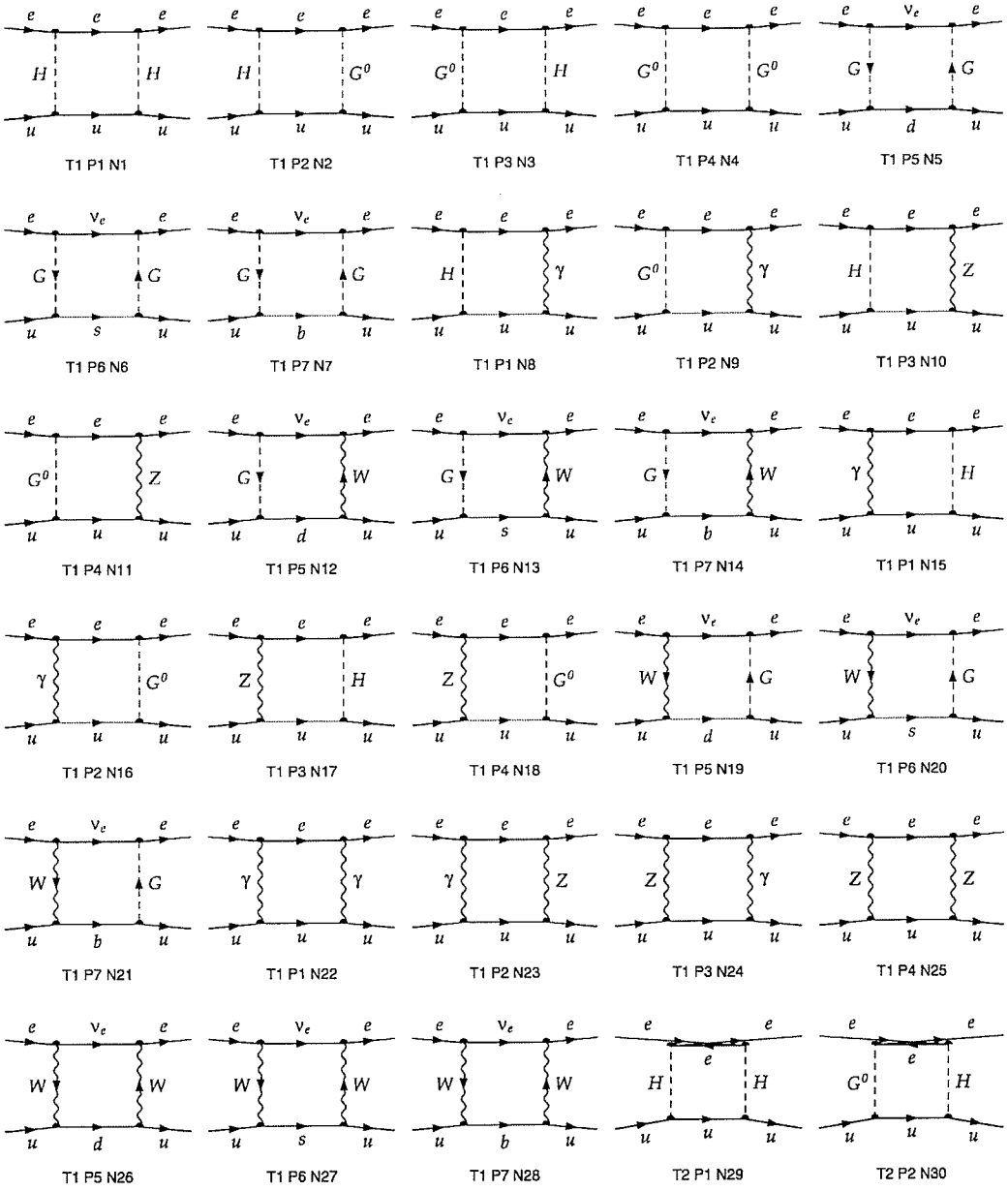

Figure 27: Boxes N1-N30

$e \quad u \rightarrow e \quad u$

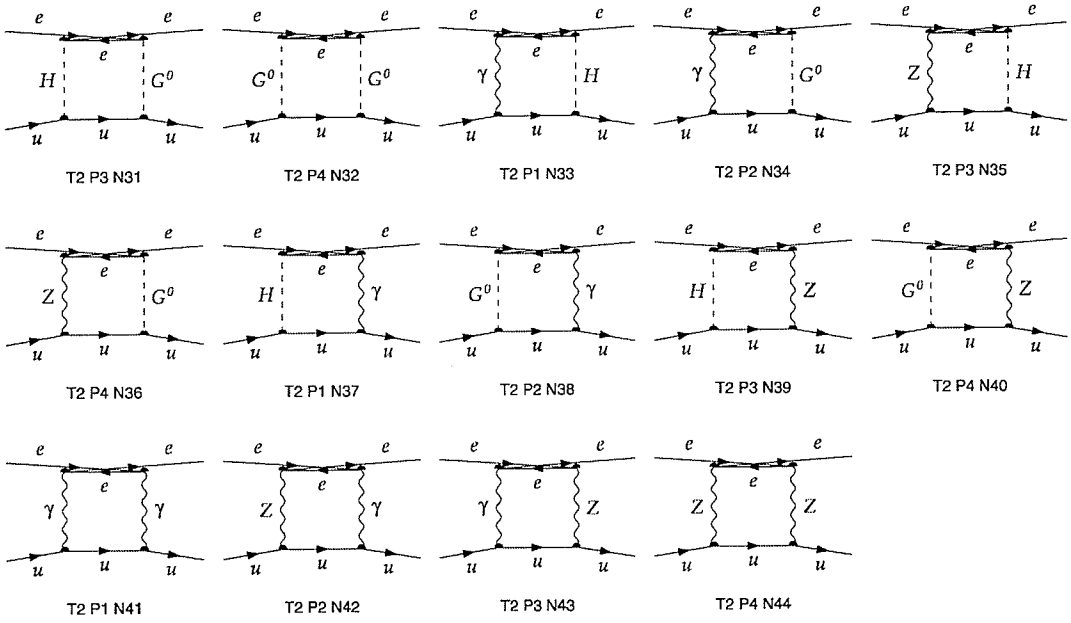

Figure 28: Boxes N31-N44

$e \quad u \rightarrow e \quad u$

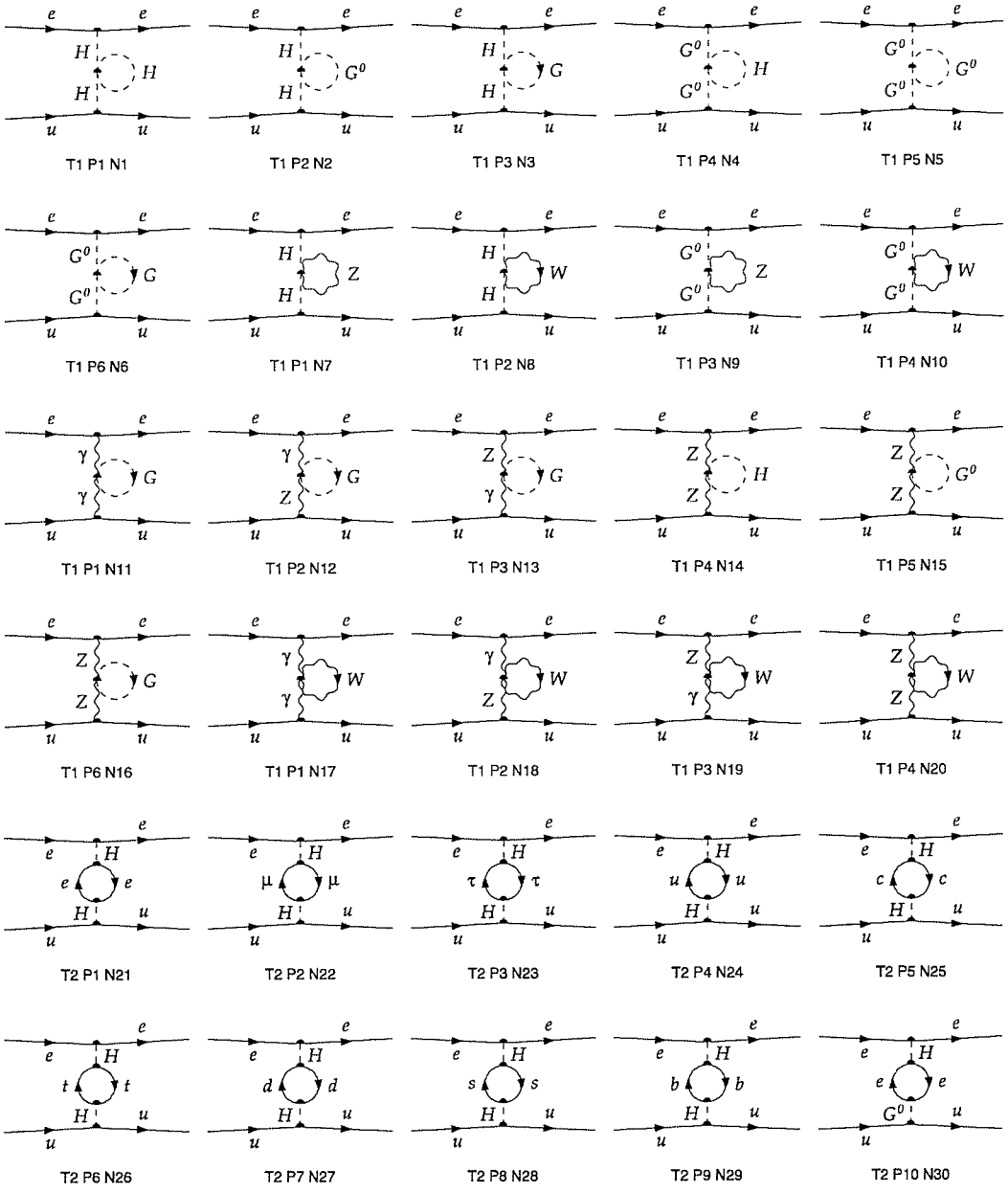

Figure 29: Self-energy N1-N30

$e \quad u \rightarrow e \quad u$

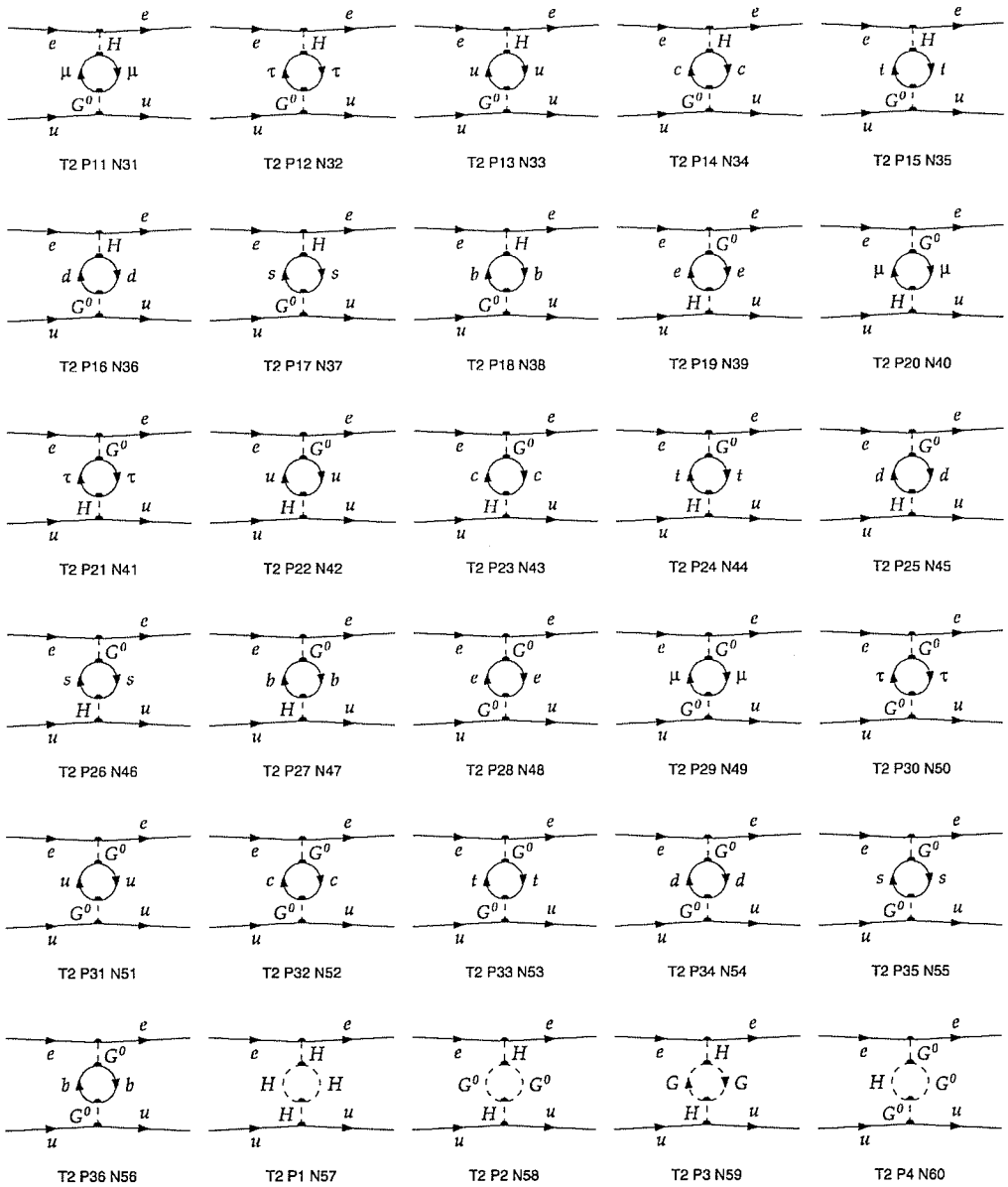

Figure 30: Self-energy N31-N60

$e \quad u \rightarrow e \quad u$

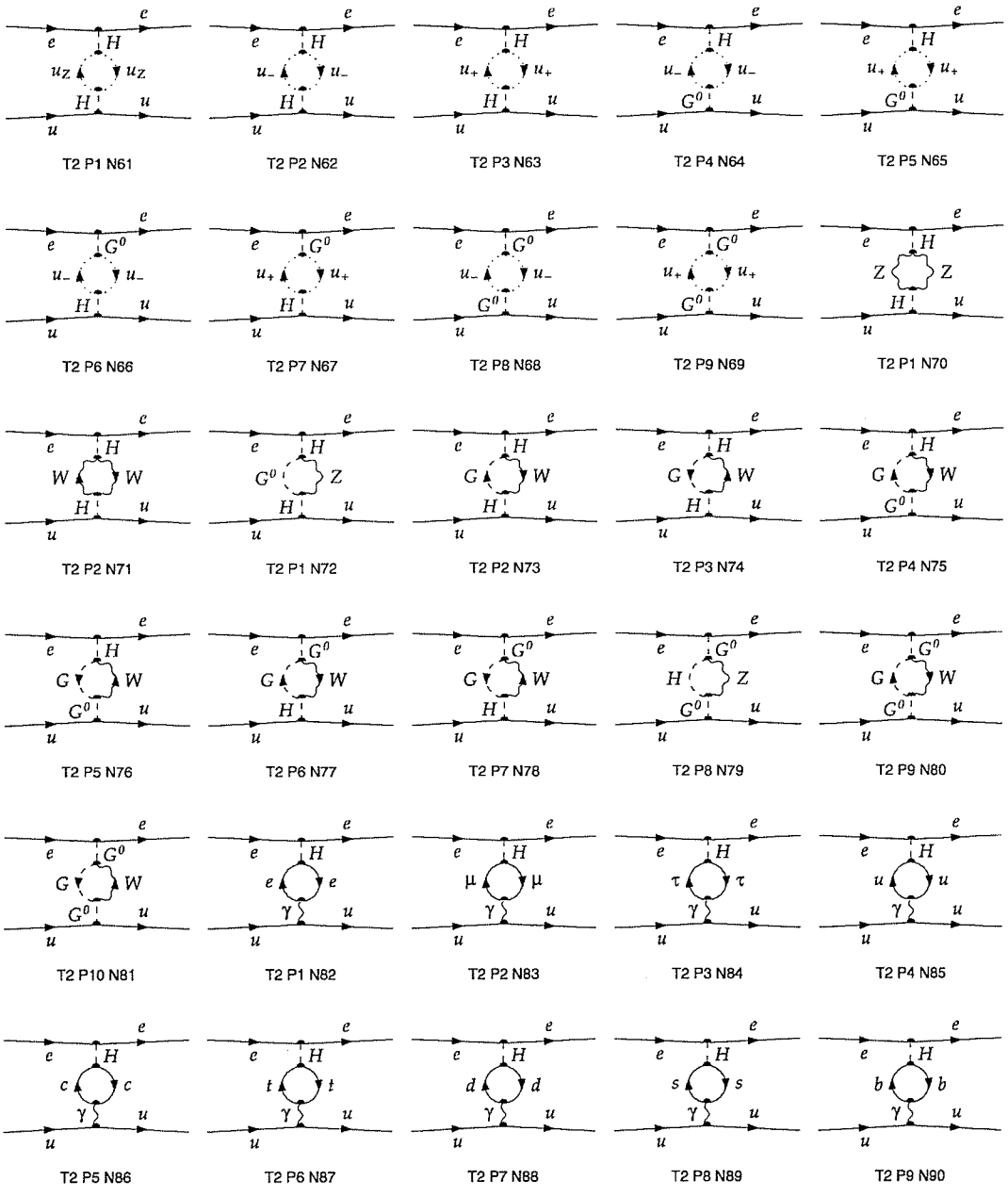

Figure 31: Self-energy N61-N90

$e \quad u \rightarrow e \quad u$

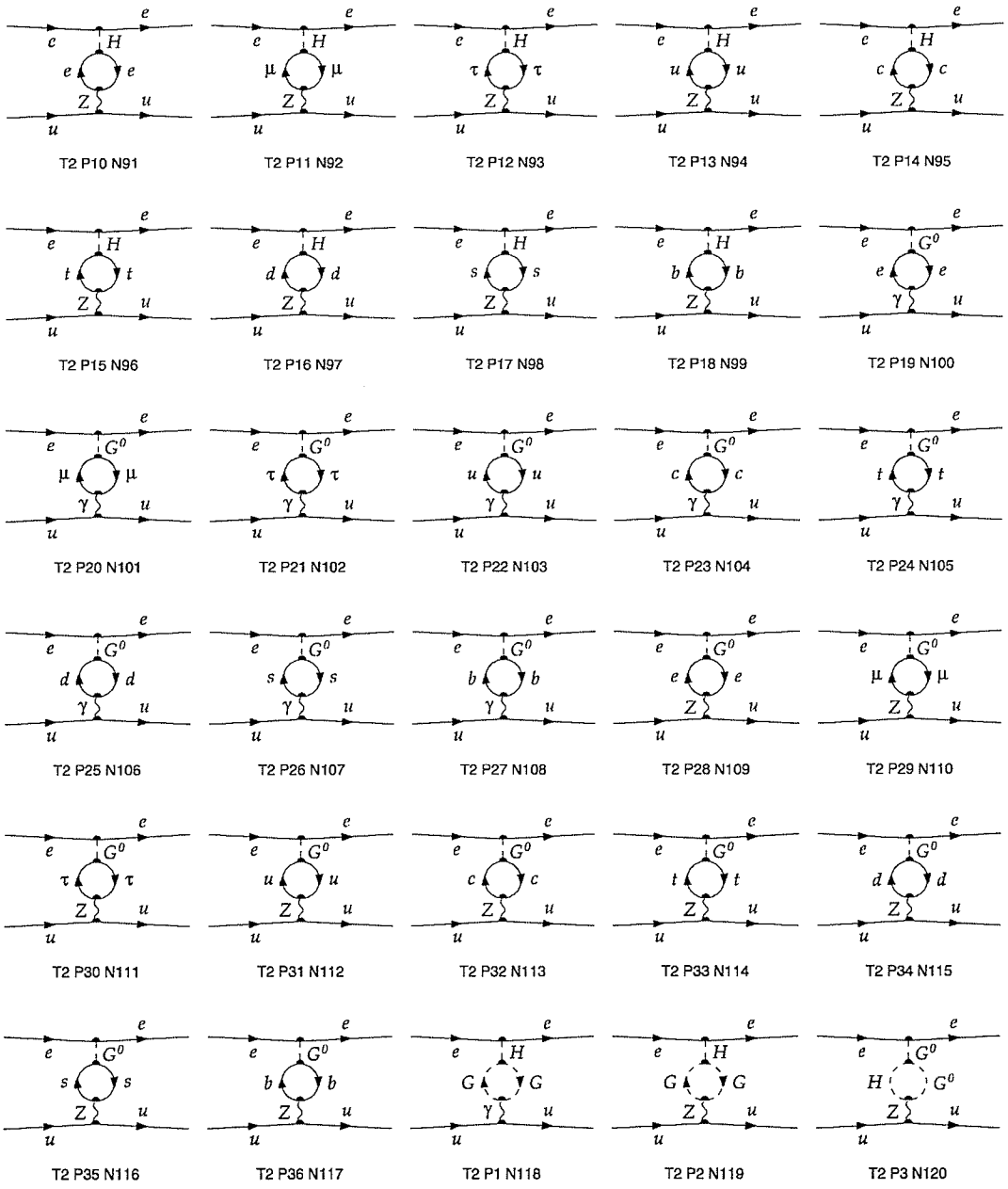

Figure 32: Self-energy N91-N120

$e \quad u \rightarrow e \quad u$

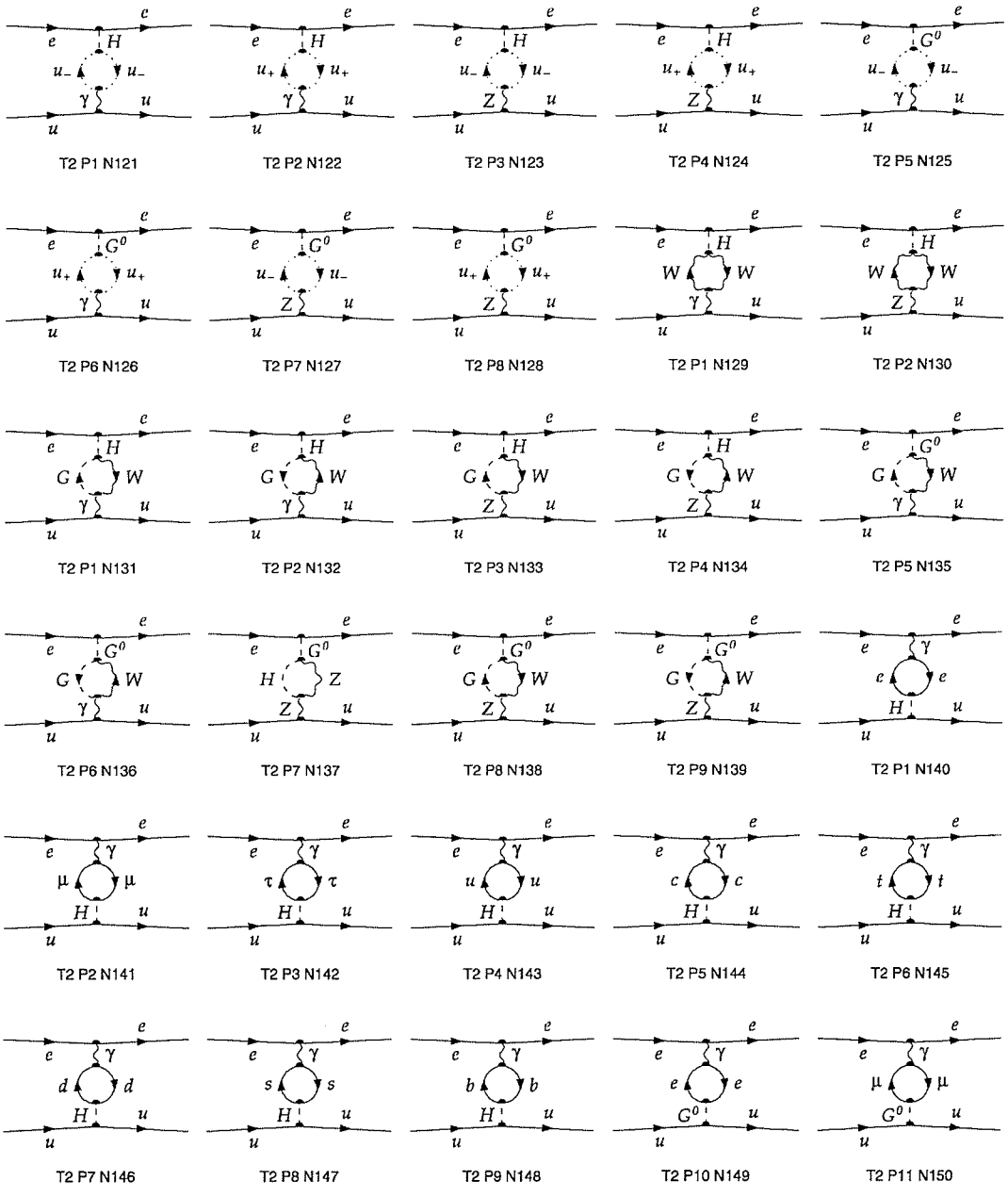

Figure 33: Self-energy N121-N150

$e \quad u \rightarrow e \quad u$

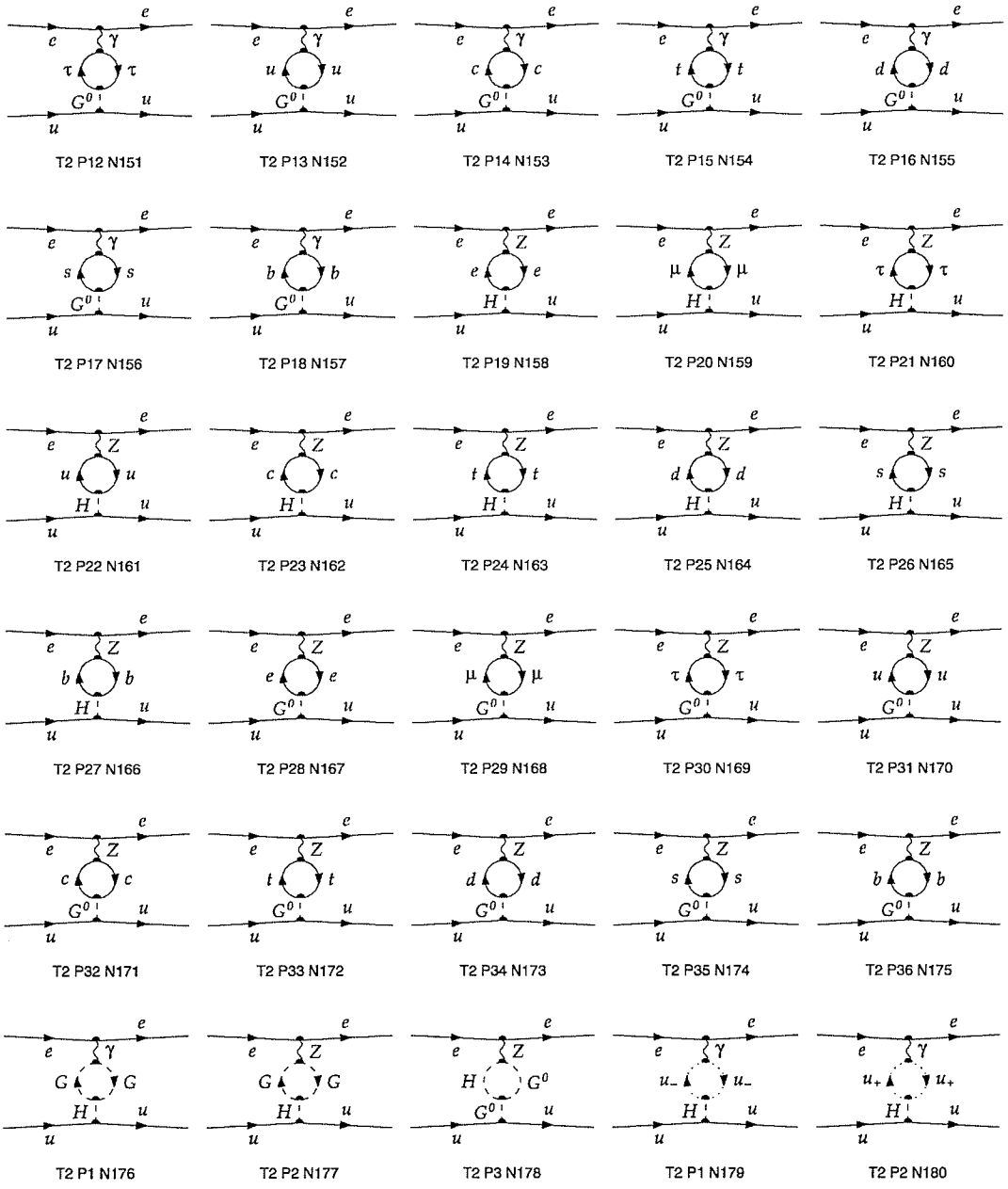

Figure 34: Self-energy N151-N180

$e \quad u \rightarrow e \quad u$

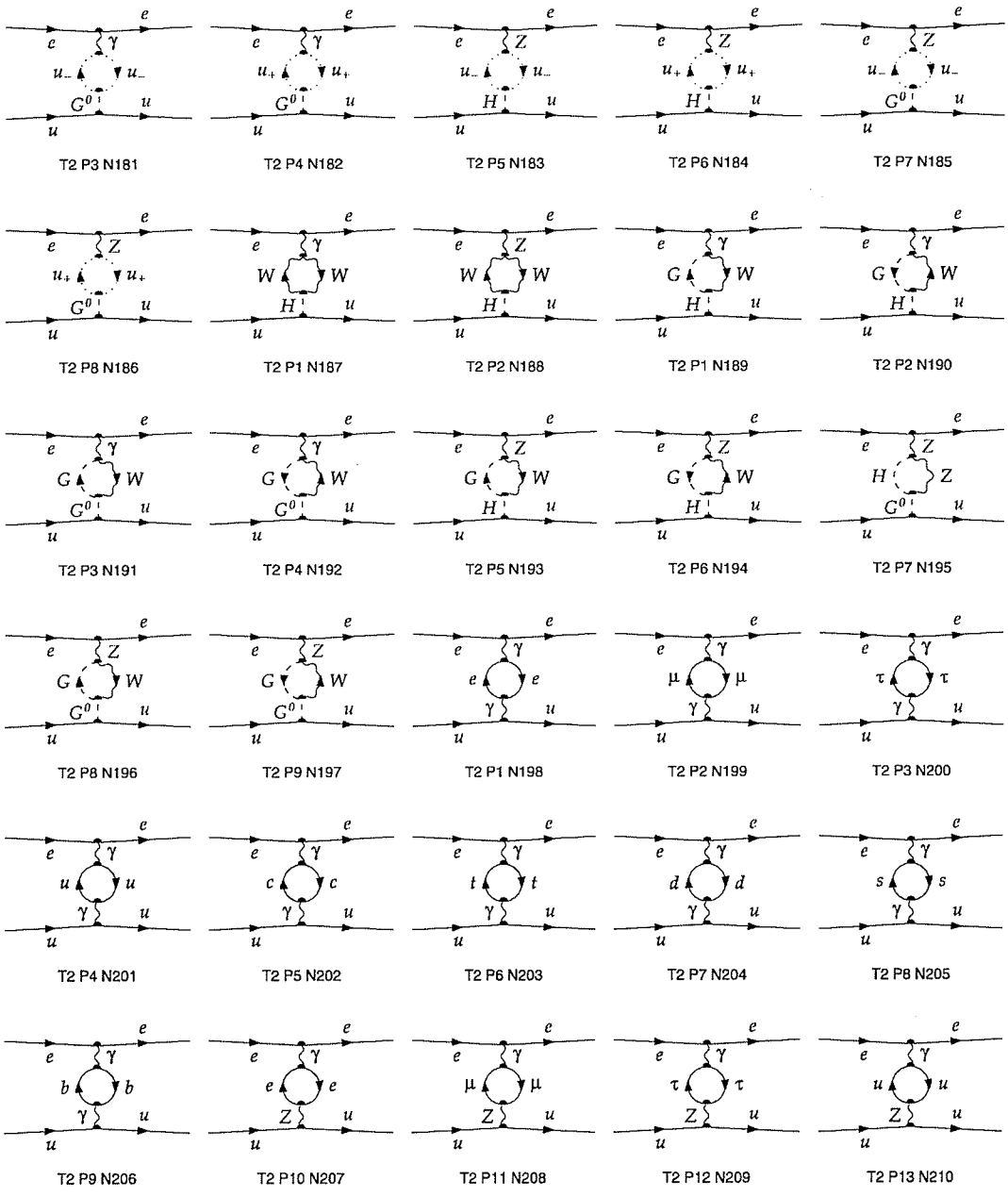

Figure 35: Self-energy N181-N210

$e \quad u \rightarrow e \quad u$

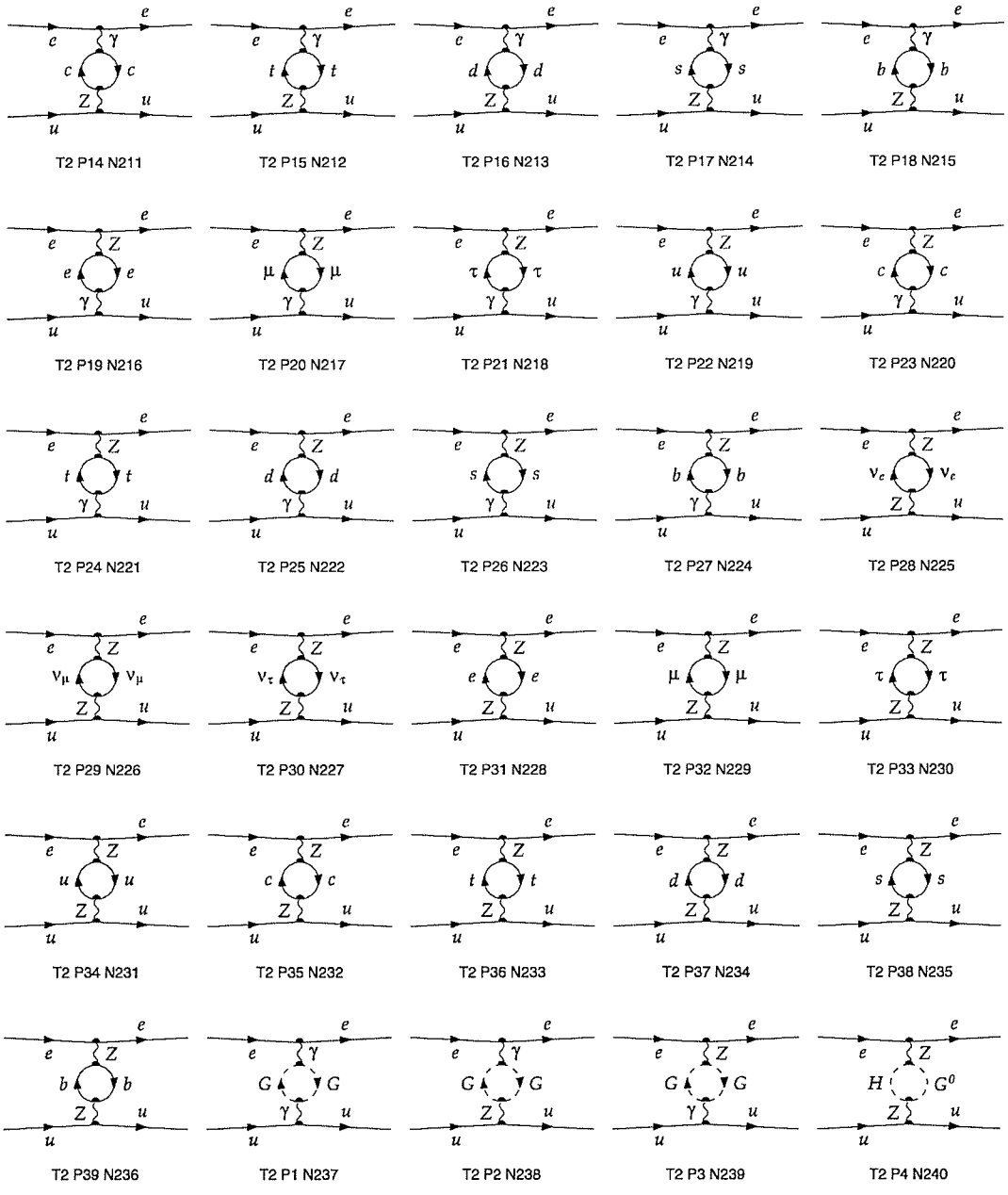

Figure 36: Self-energy N211-N240

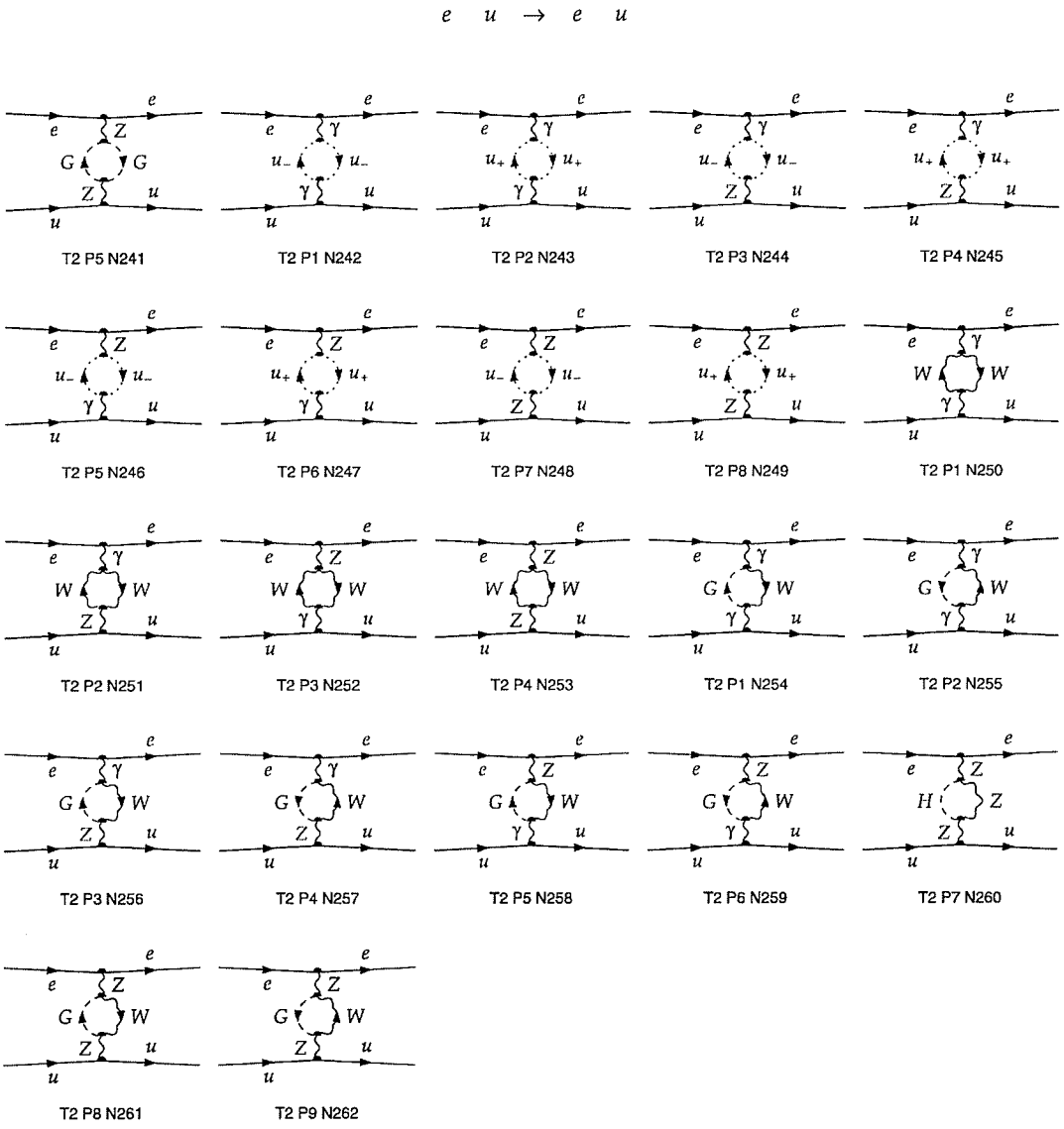

Figure 37: Self-energy N241-N262

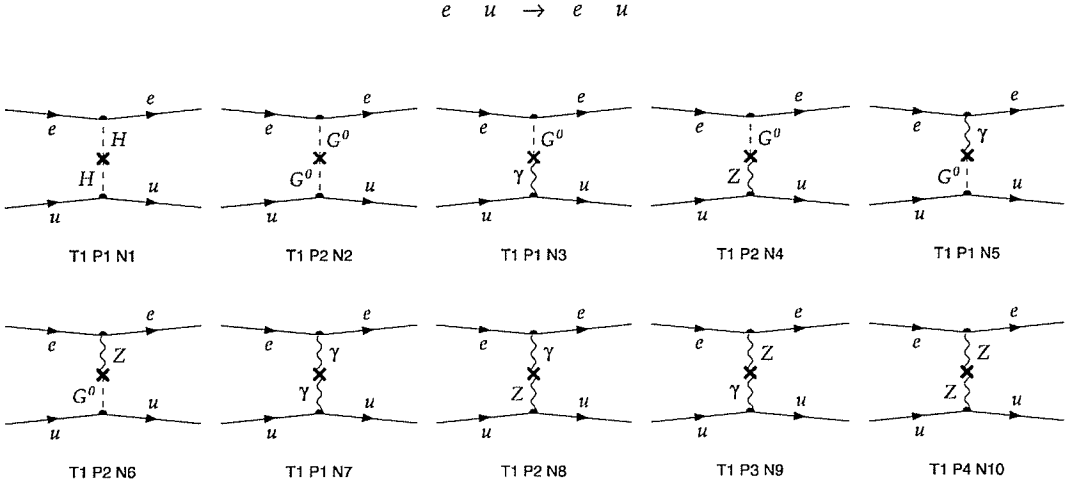

Figure 38: Self-energy counterterms N1-N10

$e \quad u \rightarrow e \quad u$

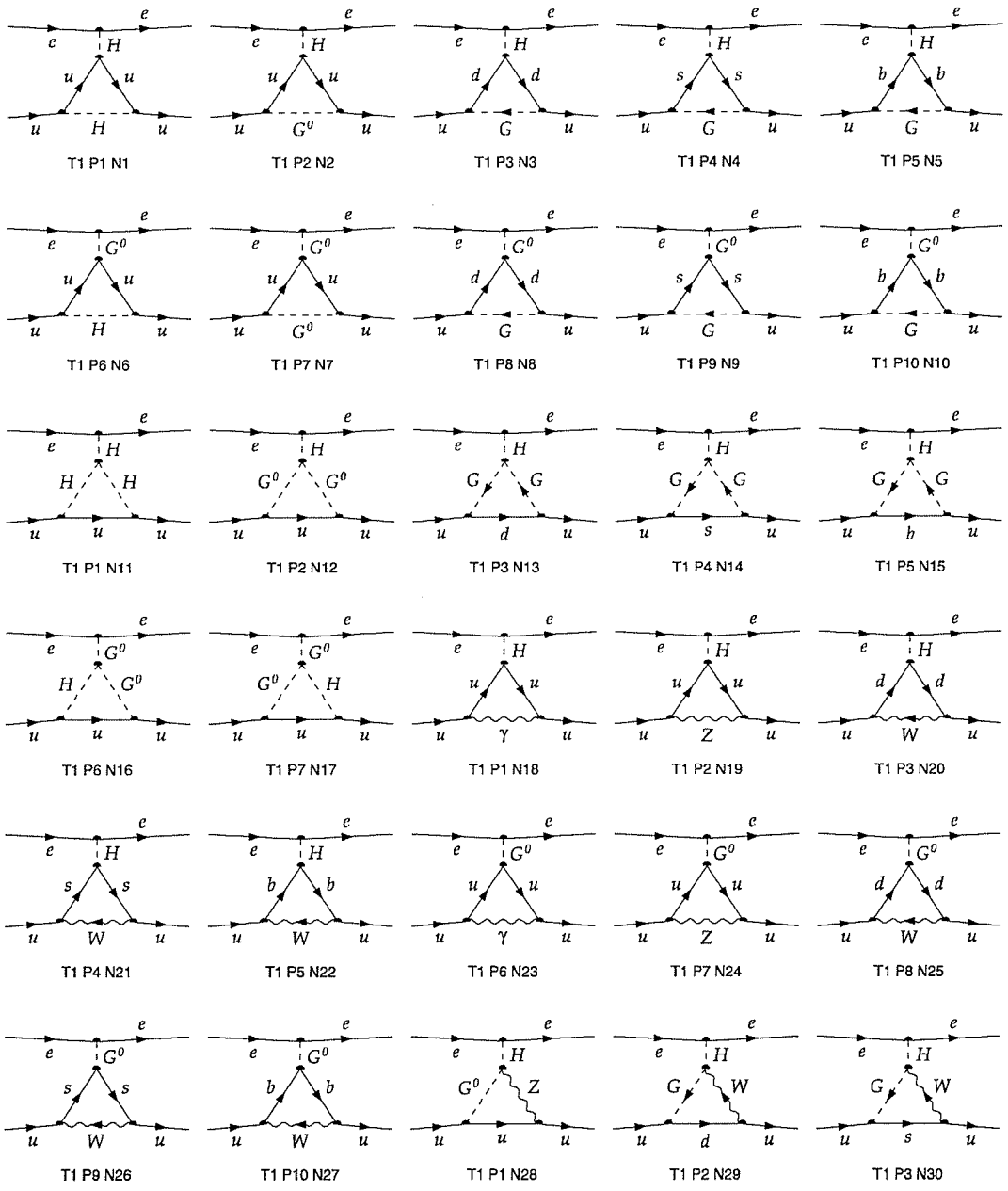

Figure 39: Triangles N1-N30

$e \quad u \rightarrow e \quad u$

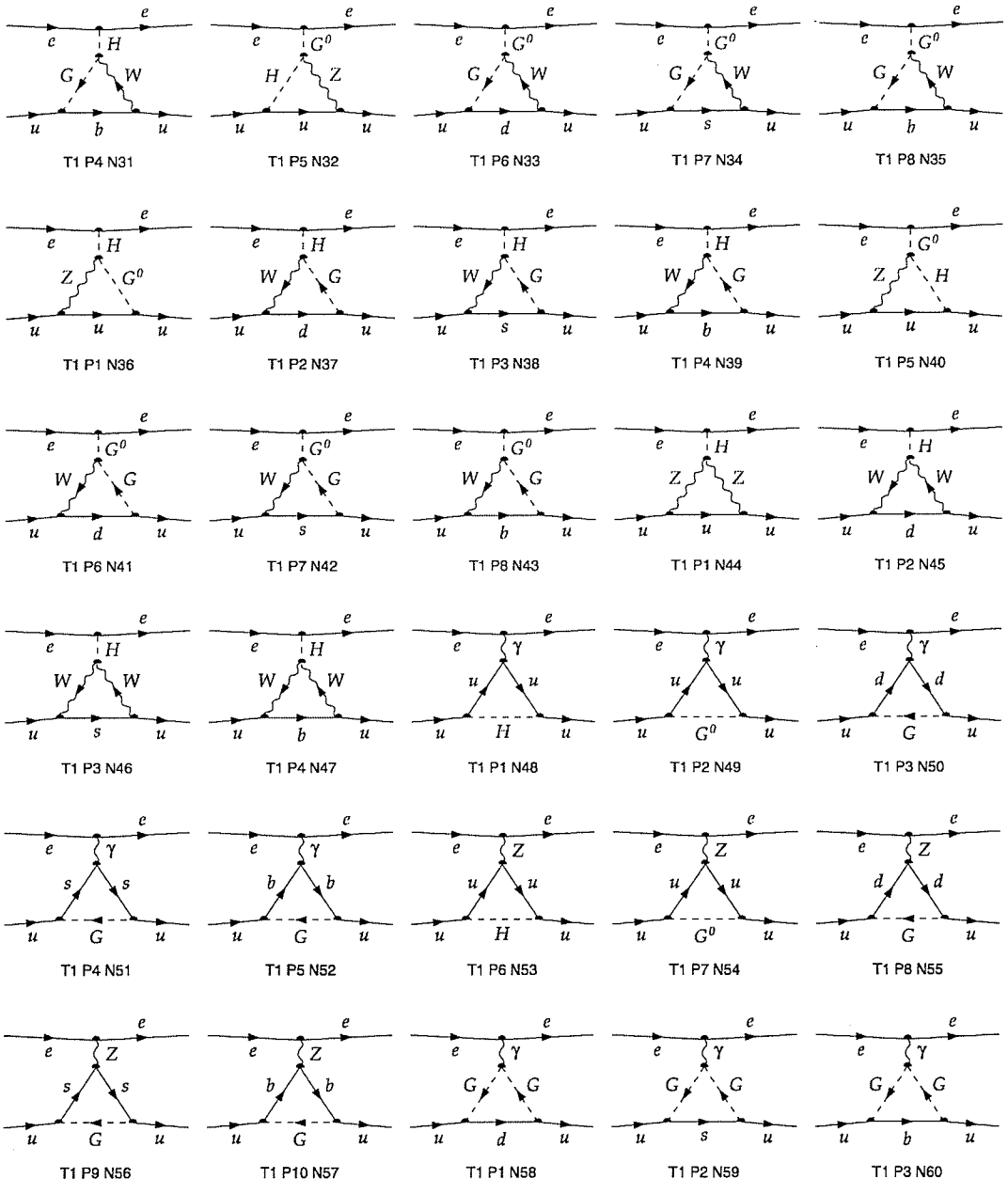

Figure 40: Triangles N31-N60

$e \quad u \rightarrow e \quad u$

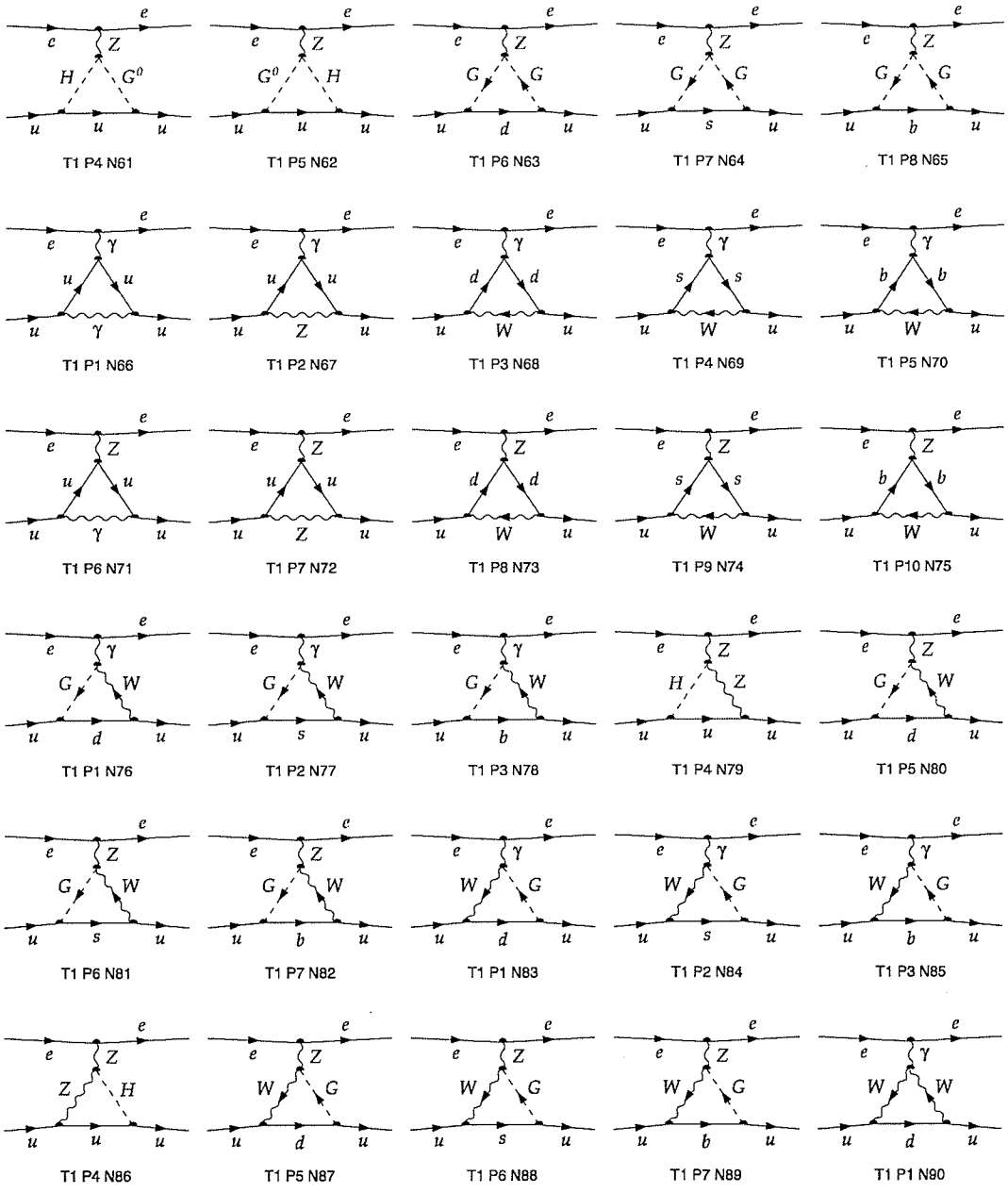

Figure 41: Triangles N61-N90

$e \quad u \rightarrow e \quad u$

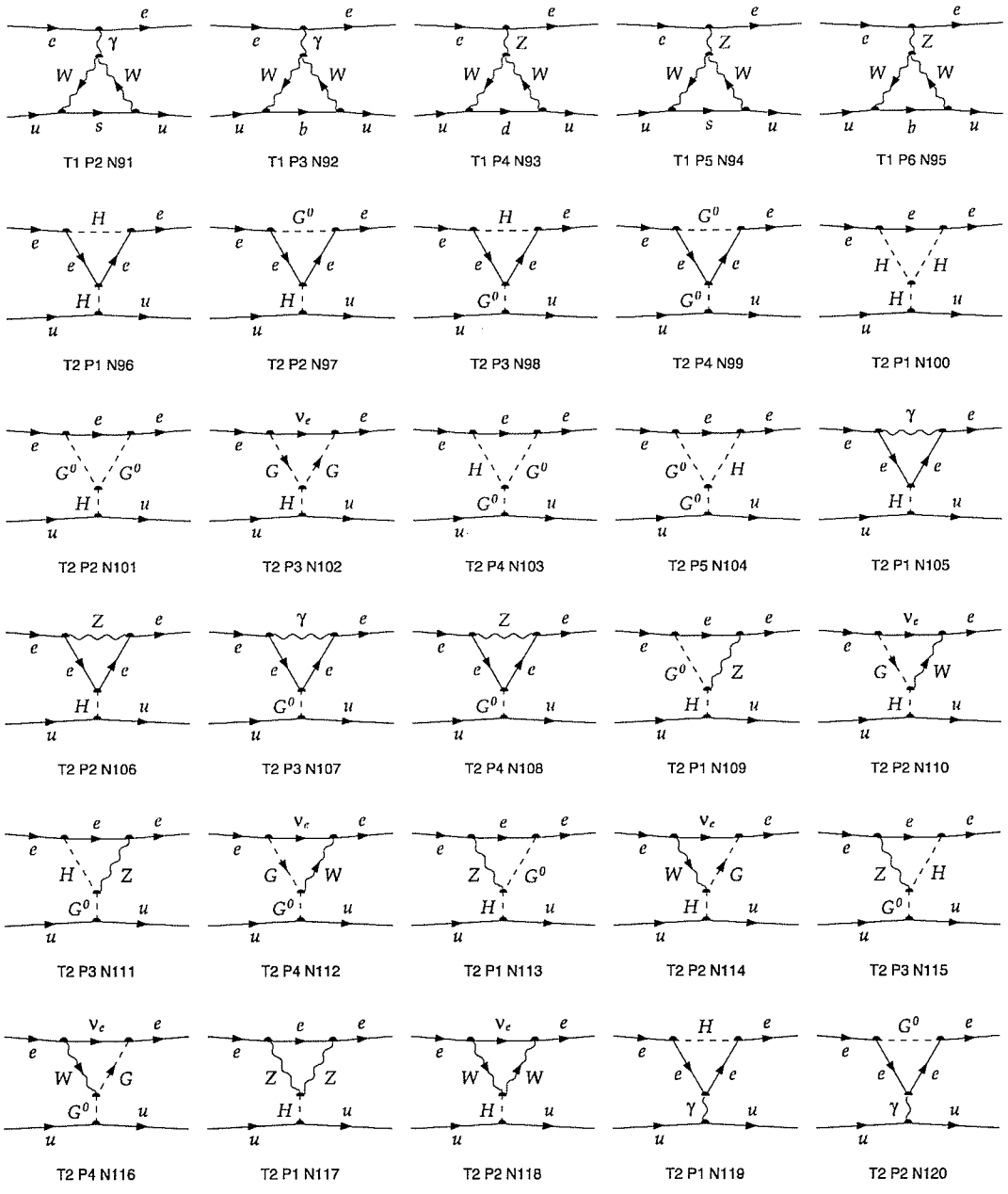

Figure 42: Triangles N91-N120

$e \quad u \rightarrow e \quad u$

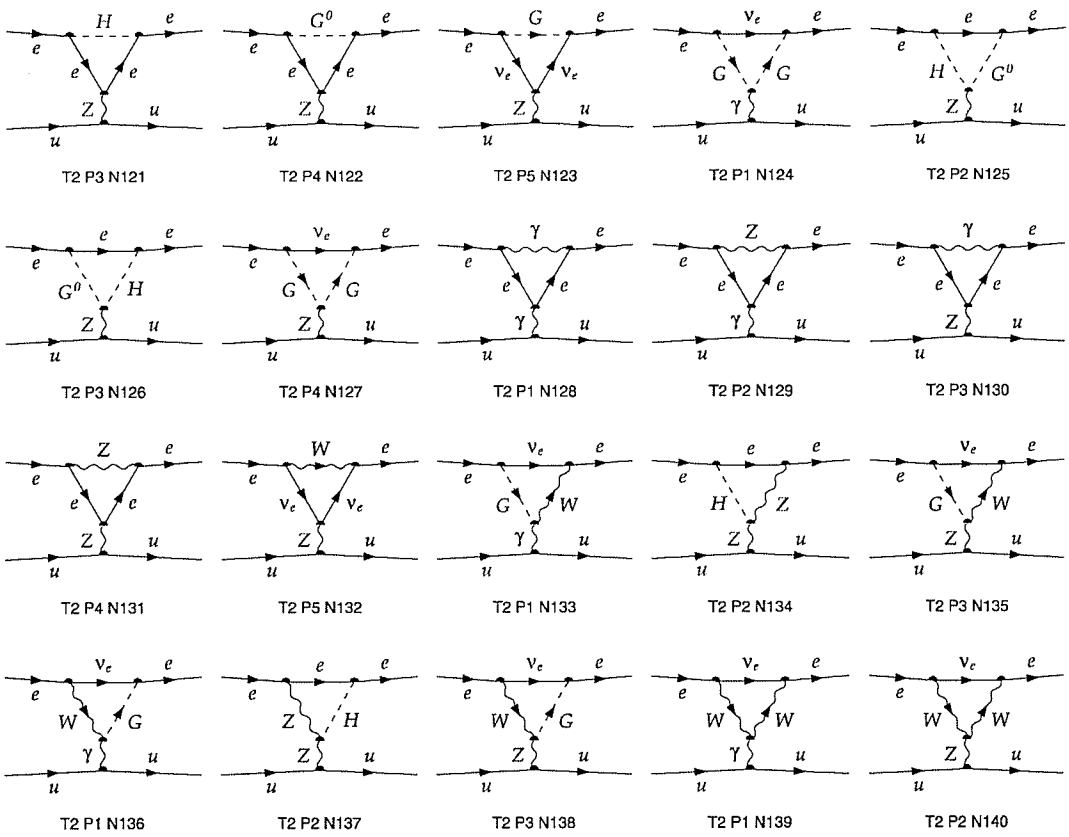

Figure 43: Triangles N121-N140

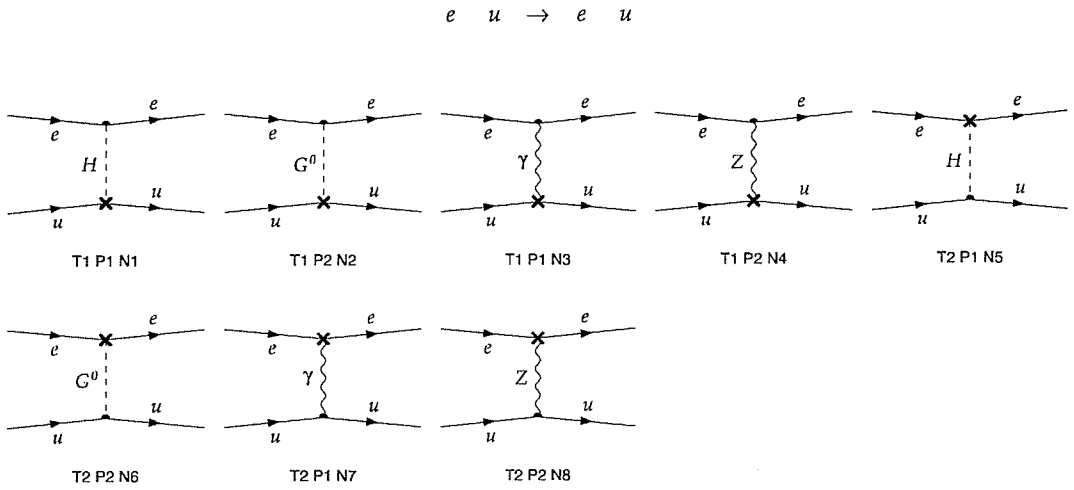

Figure 44: Triangles counterterms N1-N8

References

[1] A4 at Mainz proposal at http://www.kph.uni-mainz.de/A4/Welcome.html.

[2] F. del Aguila *et al.*, Nucl. Phys. B **537**, 561 (1999).

[3] A.I. Akhiezer and M.P. Rekalo, Sov. J. Part. Nucl. **3**, 277 (1974).

[4] K.A. Aniol *et al.*, Phys. Lett. B **509**, 211 (2001).

[5] J. Ashman *et al.* [European Muon Collaboration], Phys. Lett. B **206**, 364 (1988).

[6] B. Bauss *et al.*, "The ATLAS Experiment at CERN", at http://www.physik.uni-mainz.de/Forschungsbericht/ETAP/sec_atlas.html.

[7] D.H. Beck and B.R. Holstein, Int. J. Mod. Phys. E **10**, 1 (2001).

[8] D.H. Beck and R.D. McKeown, Ann. Rev. Nucl. Part. Sci. **51**, 189 (2001).

[9] D.H. Beck, Phys. Rev. D **39**, 3248 (1989).

[10] E.J. Beise *et al.*, Proc. SPIN96 Symp., Amsterdam, Sept. 1996, nucl-ex/9610011 (1996).

[11] F. Bloch and A. Nordsieck, Phys. Rev. **37,** 54 (1937).

[12] M. Bohm, W. Hollik, H. Speisberger, Fort. Phys. **34**, 688 (1986)

[13] E.J. Brash *et al.*, Phys. Rev. C **65,** 051001 (2002).

[14] E. E. Bruins *et al.*, Phys. Rev. Lett. **75**, 21 (1995).

[15] S. J. Dong, K. F. Liu, and A. G. Williams, Phys. Rev. D **58**, 074504 (1998).

[16] J. F. Donoghue, E. Golowich, and B. R. Holstein, "Dynamics of the Standard Model", Series: Cambridge Monographs on Particle Physics, Nuclear Physics and Cosmology (1996).

[17] B.W. Filippone and X. Ji, Adv. Nucl. Phys. **26**, 1 (2001).

[18] G0 web page, http://www.npl.uiuc.edu/exp/G0/G0Main.html.

[19] J. Gasser, H. Leutwyler, and M.E. Sainio, Phys. Lett. B **253**, 163 (1991).

[20] S. L. Glashow, Nucl. Phys. B **22**, 579 (1961);

S. Weinberg, Phys. Rev. Lett. **19**, 19 (1967);

A. Salam, in "Elementary Particle Theory", p. 367 (1968).

[21] T. Hahn and M. Perez-Victoria, Comp. Phys. Comm. **118**, 153 (1999).

[22] T. Hahn, Nucl. Phys. Proc. Suppl. **89**, 231-236 (2000).

[23] T. Hahn, Ph.D. thesis, University of Karlsruhe (1997).

[24] R. Harlander and M. Steinhauser, Prog. Part. Nucl. Phys. **43**, 167 (1999).

[25] T.R. Hemmert, U.-G. Meissner, and S. Steinberg, Phys. Lett. B **437,** 184 (1998).

[26] W.F. Hollik, Fortsch. Phys. **38**, 165 (1990).

[27] W. F. L. Hollik, DESY 88-188, ISSN 0418-9833 (1988).

[28] G 't Hooft, Nucl. Phys. B **33**, 173 (1971).

[29] G. 't Hooft and M. Veltman, Nucl. Phys. B **153**, 365 (1979).

[30] T. M. Ito *et al.* [SAMPLE collaboration], Phys. Rev. Lett. **92**, 102003 (2004).

[31] R. L. Jaffe, Phys. Lett. B **229**, 275 (1989).

[32] Jefferson Lab Experiment E02020 "The Q(Weak) Experiment: A Search for Physics at the TeV Scale Via a Measurement of the Proton's Weak Charge" Spokespersons: J. Bowman, R. Carlini, J. Finn, V. A. Kowalski, S. Page. Proposal to PAC 21 at http://www.jlab.org/qweak/.

[33] Jefferson Lab Experiment 99-115, "Constraining the Nucleon Strangeness Radius in Parity Violating Electron Scattering" Spokespersons: K. Kumar, D. Lhuillier. Proposal at http://hallaweb.jlab.org/experiment/HAPPEX/.

[34] N. Mathur and S.-J. Dong, Nucl. Phys. Proc. Suppl. **94**, 311-314 (2001).

[35] Michio Kaku, "Quantum Field Theory", Oxford University Press (1993).

[36] D. Kaplan and A. Manohar, Nucl. Phys. B **310**, 527 (1988).

[37] D. B. Leinweber and A. W. Thomas, Phys. Rev. D **62**, 074595 (2000).

[38] F. E. Maas *et al.* [A4 Collaboration], Phys. Rev. Lett. **93,** 022002 (2004).

[39] W. J. Marciano, A. Sirlin, Phys. Rev. D **29**, 75 (1984).

[40] L.C. Maximon and J.A. Tjon, Phys. Rev. C **62**, 054320 (2000).

[41] B.A. Mueller *et al.*, Phys. Rev. Lett. **78**, 3824 (1997); D.T. Spayde *et al.*, Phys. Rev. Lett. **84**,1106 (2000); R. Hasty *et al.*, Science **290**, 2117 (2000).

[42] M.J. Musolf, Ph.D. thesis, Princeton University (1989).

[43] M.J. Musolf and B.R. Holstein, Phys. Lett. B **242**, 461 (1990).

[44] M.J. Musolf and B.R. Holstein, Phys. Rev. D **43**, 2956 (1991).

[45] M.J. Musolf *et al.*, Phys. Rep. **239**, 1 (1994).

[46] Particle Data Group, D.E. Groom *et al.*, Eur. Phys. J. C **15**, 1 (2000).

[47] G. Passarino and M. Veltman, Nucl. Phys. B **160**, 151 (1979).

[48] M. E. Peskin and D. V. Schroeder, "An Introduction to Quantum Field Theory", Westview Press (1995).

[49] Q_{weak} Experiment Websites, http://www.jlab.org/qweak/, http://p23.lanl.gov/len/qweak/index.html.

[50] William B. Rolnick, "The Fundamental Particles and Their Interactions", Addison-Wesley Publishing Company (1994).

[51] SAMPLE Collaboration Home Page at Illinois, http://www.npl.uiuc.edu/exp/sample/sampleMain.html.

[52] W. Siegel, Phys. Lett. B **84**, 193 (1979).

[53] A. Silva, H.-C. Kim, and K.Goeke, Phys. Rev. D **65**, 014016 (2002); Erratum-ibid. D **66**, 039902 (2002).

[54] D.T. Spayde, Ph.D. thesis, University of Maryland (2001).

[55] J. C. Ward, Phys. Rev. **78**, 182 (1950);

Y. Takahashi, Nuovo Cim. **6**, 371 (1957).

[56] Y.B. Zeldovich, Zh. Eksp. Teor. Fiz. **36**, 964 (1959).

[57] S.-L. Zhu *et al.*, Phys. Rev. D **62**, 033008 (2000).